

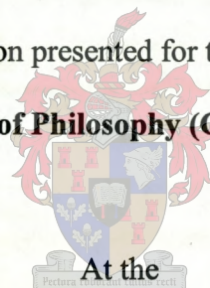
**SOL-GEL PREPARATION, CHARACTERISATION AND
ELECTROCHEMISTRY OF MIXED METAL TIN OXIDE ELECTRODES**

By

Priscilla GL Baker

Dissertation presented for the degree of

Doctor of Philosophy (Chemistry)



At the

University of Stellenbosch

Promoter

Prof. AM Crouch

Co-Promoter

Prof. RD Sanderson

Stellenbosch

December 2004

I, the undersigned, hereby declare that the work contained in this dissertation is my own original work and that I have not previously in its entirety, or in part, submitted it at any university for a degree.

Abstract

Mixed metal oxide stannates were prepared by sol-gel methods and coated onto solid titanium substrates as thin films using spin and dip coating methods. Metal oxides such as Sb_2O_5 , ZrO_2 , CuO , MnO_x and PdO_2 were introduced into a SnO_2 host matrix using sol-gel techniques. TGA analysis showed that $\text{PdO}_2/\text{SnO}_2$ forms the most stable phase. UV/vis spectroscopy confirmed that the band gap energies of all mixed metal oxides were in the range 2.37-3.37 eV. The thin film surfaces were characterised using Scanning Electron Microscopy and Atomic Force Microscopy confirmed the porous nature of the coatings and the absence of extensive cracks and surface defects. Chemical composition analysis was performed with PIXE/RBS combination, confirming the stoichiometry of the films. Cyclic voltammetry (CV) was used (a) for preliminary electrochemical characterisation in a 0.001M H_2SO_4 background (b) for investigation of oxidative ability of the novel thin films (c) and for evaluation of the suitability of these thin films electrodes as anodes for organic combustion.

Cyclic voltammetry of the mixed metal oxide electrodes in a 0.001 M H_2SO_4 solution showed that only the Sb_2O_5 and ZrO_2 doped tin oxide electrodes were suitable for electrocatalytic evaluation. The $\text{ZrO}_2\text{-SnO}_2$ electrode showed 19% efficiency for oxidation of phenol in bulk electrolysis experiments and the major products were quinones. Electrochemical impedance spectroscopy (EIS) at the Sb_2O_5 and ZrO_2 doped tin oxide electrode interface, was performed in a coating flat cell. EIS confirmed that both electrodes were able to oxidise $\text{K}_3\text{Fe}(\text{CN})_6$ and hydroquinone, but phenol oxidation was not confirmed.

Opsomming

Die gemengde metaaloksied gel materiaal, is met behulp van TGA en UV/vis gekarakteriseer. Scanning Electron Microscopy en Atomic Force Microscopy is gebruik om die morfologie van die gemengde metaaloksiedoppervlakke te karakteriseer. Chemiese komposisie analise is deur middel van PIXE/RBS kombinasie uitgevoer. Dit is gebruik om te bevestig dat die ZrO_2 , CuO , MnO_2 , Sb_2O_5 en PdO_2 wel by die SnO_2 gasheer in gesluit was, in die formasie van die homogene dun films. Die voorlopige electrochemiese evaluasie van die gemengde metaaloksied elektrodes, in 0.001 M H_2SO_4 , was deur middel van sikliese voltammetrie gedoen. Sikliese voltammetrie is ook aangewend in die evaluering van die oksidasie vermoë van die nuwe elektrokataliste. Die elektriese parameters van die elektrode materiaal en die oplossings tussen fase is deur middel van impedansiespektroskopie bepaal. EIS het bewys dat die Sb_2O_5 en ZrO_2 gemengde tinoksiedelektrodes, wel die $K_3Fe(CN)_6$ en hydrokwinoon oplossings geoksideer hê, maar die oksidasie van die fenol oplossing was nie bevestig nie.

Acknowledgements

- ❖ I wish to express sincere appreciation to my promoters Prof. AM Crouch and Prof. RD Sanderson for their assistance, encouragement and financial support throughout the project.

- ❖ I would like to acknowledge the financial assistance of the Water Research Commission (WRC) and the National Research Foundation (NRF) of South Africa.

- ❖ The assistance of Dr. W Pzybolowitz and Dr. C Theron of Ithemba Labs (South Africa) with surface analysis by microprobe, is acknowledged.

- ❖ I would also like to thank my colleagues and co-workers in the analytical and separations group (University of Stellenbosch), for their friendship and encouragement particularly on days when nothing seemed to work.

- ❖ To my husband, son, friends and family for their constant support, encouragement and love, thank you very much.

Wisdom is better than strength

¹ For all this I considered in my heart, even to declare all this,
That the righteous and the wise and their works, are in the hand of God:

¹¹ The race is not to the swift, nor the battle to the strong;
neither yet bread to the wise, nor yet riches to men of understanding;
nor yet favour to men of skill;
but time and chance happeneth to them all

Ecclesiastes 9:1,11. The Holy Bible

List of abbreviations

ac	Alternating current
AFM	Atomic force microscopy
BE	Bulk electrolysis
CE	Counter electrode
CFC	Coating flat cell
CPE	Constant phase element
CV	Cyclic voltammetry
dc	direct current
eec	Electrical equivalent circuit
EHI	Electrochemical hydrodynamic impedance
EIS	Electrochemical impedance spectroscopy
FTF	Fracture transfer function impedance analysis
IR drop	voltage drop across electrodes
oer	oxygen evolution reaction
PIXE	Particle induced x-ray emission
RBS	Rutherford backscattering
R_{ct}	Charge transfer resistance
RF sputtering	Radio frequency sputtering
R_s	Solution resistance
RUMP	Rutherford universal manipulation programme
SEM	Scanning electron microscopy
TGA	Thermogravimetric analysis
UHQ	Ultra high quality
UV/vis	UV visible spectroscopy
WE	Working electrode
Z_w	Warburg impedance

List of Contents

Author's declaration

Abstract

Opsomming

Acknowledgements

List of abbreviations

List of tables

List of figures

Chapter one: Introduction and objectives

1.1	Transition metals as catalysts	1
1.2	Tin oxide as electro-catalyst host material	3
1.3	Some applications of doped tin oxide electrodes	4
1.4	Motivation for the dissertation	7
1.5	Overall aim of the thesis	8
1.6	Objectives	8
1.7	Significant contributions of the dissertation	10
1.8	Layout of the dissertation	10

Chapter two: Theoretical background

2.1	Introduction	12
2.2	Requirements for efficient electrocatalysts	12
2.3	Disadvantages of metal oxide electrodes	13
2.4	Transition metal oxide electrocatalysts	14

2.5	Selected transition metal doped SnO ₂ materials, for electrocatalytic investigations	15
2.6	Sol-gel techniques	16
2.7	Characterisation tools and methods	17
2.7.1	Thermogravimetric analysis	17
2.7.2	UV/vis spectroscopy	18
2.7.3	X-Ray methods	18
2.7.4	Microscopy	
2.7.4.1	Scanning electron microscopy (SEM)	19
2.7.4.2	Atomic force microscopy (AFM)	19
2.7.5	Nuclear probe methods	
2.7.5.1	Rutherford backscattering (RBS)	21
2.7.5.2	Particle induced X-ray emissions (PIXE)	21
2.8	Cyclic voltammetry	22
2.8.1	Cyclic voltammetry as a diagnostic tool for determining the reversibility of redox reactions	24
2.9	Electrochemical impedance spectroscopy	25
2.9.1	Electrochemical impedance spectroscopy data presentation	28

Chapter three: Preparation of mixed metal tin oxides

3.1	Introduction	31
3.2	Experimental conditions	
3.2.1	Sol-gel preparation of mixed metal oxide electrodes	31
3.2.2	Preparation of thin film electrodes	33

3.3	Properties of electrodes with increased surface area	36
3.4	Experimental	
3.4.1	Method 1: using surfactants	37
3.4.2	Methods 2: using porous substrate	38
3.5	Results and discussion	
3.5.1	Method 1: using surfactants	38
3.5.2	Method 2: using porous substrate	39
3.6	Conclusion	40

Chapter four: Characterisation of mixed metal tin oxides

4.1	Introduction	42
4.2	Experimental	
4.2.1	Thermogravimetric analysis	42
4.2.2	UV/vis spectroscopy	43
4.2.3	X-ray diffraction	43
4.2.4	Scanning electron microscopy	44
4.2.5	Atomic force microscopy	44
4.2.6	Particle induced X-ray emissions /Rutherford backscattering	44
4.3	Characterisation results and discussion	
4.3.1	Thermogravimetric analysis	45
4.3.2	UV/vis spectroscopy	47
4.3.3	X-ray methods.....	49
4.3.4	Scanning electron microscopy	51
4.3.5	Atomic force microscopy	53
4.3.6	Rutherford backscattering	55

4.3.7	Particle induced X-ray emissions	57
4.4	Conclusion	59

Chapter five: Electrochemical characterisation by cyclic voltammetry

5.1	Introduction	61
5.2	Experimental conditions.....	61
5.3	Results and discussion	63
5.3.1	Mixed metal tin oxides in 0.001 M H ₂ SO ₄	65
5.3.2	K ₃ Fe(CN) ₆ oxidation at Sb ₂ O ₅ /SnO ₂ and ZrO ₂ /SnO ₂ thin film electrodes	67
5.3.3	K ₃ Fe(CN) ₆ oxidation at CuO/SnO ₂ , MnO _x /SnO ₂ and PdO ₂ /SnO ₂ thin film electrodes	72
5.3.4	Tafel plots	75
5.4	Conclusions	77

Chapter six: Electrochemical impedance spectroscopy (EIS) of mixed metal oxides

6.1	Introduction	76
6.2	Common electrical circuits and circuit parameters	79
6.3	Experimental	82
6.4	Results and discussion	84
6.4.1	Uncoated titanium substrate in 0.001 M H ₂ SO ₄	84
6.4.2	Titanium substrate coated with SnO ₂ in 0.001 M H ₂ SO ₄	90
6.4.3	Titanium substrate coated with SnO ₂ /CuO, in 0.001 M H ₂ SO ₄	96
6.4.4	Titanium substrate coated with SnO ₂ /MnO _x in 0.001 M H ₂ SO ₄	99

6.4.5	Titanium substrate coated with SnO ₂ /PdO ₂ in 0.001M H ₂ SO ₄	102
6.4.6	Titanium substrate coated with SnO ₂ /ZrO ₂ in 0.001 M H ₂ SO ₄	104
6.4.7	Titanium coated with SnO ₂ /Sb ₂ O ₅ in 0.001 M H ₂ SO ₄	107
6.5	Prediction of double layer capacitance using cyclic voltammetry	109
6.6	Discussion and conclusion	113

Chapter seven: Electrochemical impedance spectroscopy of charge transfer reactions at ZrO₂ and Sb₂O₅ doped tin oxide thin films.

7.1	Introduction	117
7.2	Experimental	
	7.2.1 Preparation of test solutions	118
7.3	Results and Discussion	
	7.3.1 Oxidation of K ₃ Fe(CN) ₆ at Ti/SnO ₂ /Sb ₂ O ₅ electrodes.....	118
	7.3.2 Oxidation of K ₃ Fe(CN) ₆ at Ti/SnO ₂ /ZrO ₂ electrodes	121
	7.3.3 Oxidation of hydroquinone (C ₆ H ₆ O ₂) at Ti/SnO ₂ /Sb ₂ O ₅ and Ti/SnO ₂ /ZrO ₂ electrodes	123
	7.3.4 Oxidation of phenol (C ₆ H ₆ O) at Ti/SnO ₂ /Sb ₂ O ₅ and Ti/SnO ₂ /ZrO ₂ electrodes	126
7.4	Conclusions	130

Chapter eight: Electrochemical treatment of wastewater

8.1	Introduction	132
8.2	Electrochemical treatment of wastewater	132
	8.2.1 Mechanisms for combustion of organics at metal oxide anodes	133

8.3	Organic pollutants in wastewater	134
8.4	Controlled potential bulk electrolysis	136
8.5	Bulk electrolysis experiments	138
8.6	Analysis of samples by high performance liquid chromatography	140
8.6.1	High performance liquid chromatography (HPLC) results	141
8.7	Reactor design and testing of catalyst	144
8.8	Conclusions	145

Chapter nine: Conclusions and recommendations for future research

9.1	Conclusions	146
9.2	Main scientific contributions of the dissertation	150
9.3	Recommendations for future work	151
9.4	Output from this dissertation	
9.4.1	Contributions at conferences	153
9.4.2	Papers prepared for publication	153
	References	154

List of tables

Table 1.1:	Some examples of important industrial processes that make use of transition metal catalysts	2
Table 3.1:	Doping ratios for mixed metal tin oxides	33
Table 4.1:	Band gap energy values of the various mixed metal tin oxide gels prepared	47
Table 4.2:	Typical compositional analysis of mixed metal tin oxide thin films (%composition based on ppm analysis) as determined by PIXE/RBS	58
Table 5.1:	Instrumental parameters for cyclic voltammetry experiments	62
Table 6.1:	Common electrical elements used in circuit fitting	81
Table 6.2:	Results of automatic circle fit for uncoated Ti at high frequencies	87
Table 6.3:	Results of circuit fitting for uncoated titanium	89
Table 6.4:	Equivalent circuit fitting results for Ti/SnO ₂	95
Table 6.5:	Equivalent circuit fitting results for Ti/CuO/SnO ₂ electrode in H ₂ SO ₄	97
Table 6.6:	Equivalent circuit fitting results for Ti/MnO ₂ /SnO ₂ electrode in H ₂ SO ₄	101
Table 6.7:	Equivalent circuit fitting results for Ti/PdO ₂ /SnO ₂ electrode in H ₂ SO ₄	104
Table 6.8:	Equivalent circuit fitting results for Ti/SnO ₂ /ZrO ₂ electrode in H ₂ SO ₄	106
Table 6.9:	Equivalent circuit fitting results for Ti/ SnO ₂ /Sb ₂ O ₅ electrode in 0.001 M H ₂ SO ₄	108

Table 6.10:	Values for q_{in}^* , q_{out}^* , and q_{tot}^* obtained for various mixed metal stannates, using cyclic voltammetry	112
Table 6.11:	Average capacitance and resistance values of mixed metal oxide systems at high frequency, as determined by electrochemical impedance spectroscopy	113
Table 7.1:	Parameters for oxidation of $K_3Fe(CN)_6$ at $Ti/SnO_2/Sb_2O_5$ thin film electrodes	121
Table 7.2:	Fitting results for oxidation of $K_3Fe(CN)_6$ at the $Ti/SnO_2/ZrO_2$ electrode	123
Table 7.3:	Fitting results for oxidation of hydroquinone at $Ti/SnO_2/Sb_2O_5$ and $Ti/SnO_2/ZrO_2$ electrodes	126

List of figures

Figure 1.1:	Experimental lay out of the research carried out in this dissertation	11
Figure 2.1:	Potential–time profiles for sweep voltammetry	23
Figure 2.2:	Current-voltage plot for an oxidation reduction with $O = R$ and $O + e^- \leftrightarrow R$	27
Figure 2.3:	Complex plot of EIS data for $O + e^- \leftrightarrow R$, both soluble species	29
Figure 2.4:	Bode plots: magnitude (top) and phase angle (bottom) change vs frequency	30
Figure 3.1:	Schematic representation of sol-gel process (M represents the dopant metal as described in the text)	32
Figure 3.2:	An example of the domestic grinder used as rotating disk in spin coating of thin films	34
Figure 3.3:	Design of mixed metal tin oxide coated electrode	35
Figure 3.4:	SEM of ZrO_2 - SnO_2 modified with DTAB	39
Figure 3.5:	SEM of ZrO_2 - SnO_2 coated onto porous titanium substrate	40
Figure 4.1:	TGA of metal oxide doped tin oxide gels (pink - ZrO_2/SnO_2 ;blue - Sb_2O_5 ; green - CuO ; brown - $MnOx/SnO_2$; red - PdO_2/SnO_2)	46
Figure 4.2:	An example of how band gap energy was measured for ZrO_2 - SnO_2	48
Figure 4.3:	The effect of ageing on SnO_2/ZrO_2 (-▲-2002 and --■--2003 samples)	49
Figure 4.4:	XRD pattern for Zr - SnO_2 powder showing only the characteristic peaks for SnO_2	50

Figure 4.5:	SEM of (a) ZrO ₂ -SnO ₂ spin coated thin film	52
	(b) PdO ₂ -SnO ₂ spin coated thin film.....	52
Figure 4.6:	AFM of (a) dip and (b) spin coated MnO _x /SnO ₂ films	54
Figure 4.7:	RBS of Zr/SnO ₂ (a) dip and (b) spin coated surfaces and the fit spectrum produced by RUMP (red)	56
Figure 5.1:	Electrochemical cell arrangement used for CV experiments	62
Figure 5.2:	Cyclic voltammetry of ZrO ₂ /SnO ₂ electrodes in H ₂ SO ₄ at different concentrations (0.001 M, 0.1 M and 0.5 M).....	64
Figure 5.3:	Current response as a function of scan rate for mixed metal tin oxide electrodes in 0.001 M H ₂ SO ₄ (-■- Sb ₂ O ₅ /SnO ₂ , -▲- ZrO ₂ /SnO ₂ , -◆-CuO/SnO ₂ , -✱-PdO ₂ /SnO ₂ , --■-- MnO _x /SnO ₂)	65
Figure 5.4:	Cyclic voltammetry of CuO/SnO ₂ in H ₂ SO ₄	66
Figure 5.5:	Cyclic voltammetry of MnO ₂ /SnO ₂ in H ₂ SO ₄	67
Figure 5.6:	ZrO ₂ /SnO ₂ current response as a function of scan rate in 0.002 M K ₃ Fe(CN) ₆ (-■— Zr1 in H ₂ SO ₄ , -▲— Zr2 in H ₂ SO ₄ , --■-- Zr1 with K ₃ Fe(CN) ₆ , --▲-- Zr2 with K ₃ Fe(CN) ₆)	68
Figure 5.7:	Cyclic voltammetry of K ₃ Fe(CN) ₆ oxidation at a ZrO ₂ /SnO ₂ thin film at scan rate 50 mV/s	69
Figure 5.8:	Sb ₂ O ₅ /SnO ₂ current response as a function of scan rate in 0.002 M K ₃ Fe ₃ (CN) ₆ (-■— Sb1 in H ₂ SO ₄ , -▲— Sb2 in H ₂ SO ₄ , --■-- Sb1 with K ₃ Fe(CN) ₆ , --▲-- Sb2 with K ₃ Fe(CN) ₆)	70
Figure 5.9:	Cyclic voltammetry of K ₃ Fe(CN) ₆ at the Sb ₂ O ₅ /SnO ₂ thin film electrode at scan rate 25 mV/s	71

Figure 5.10	Cyclic voltammetry of 0.002 M $K_3Fe(CN)_6$ oxidation at (a) CuO/SnO_2 and (b) MnO_2/SnO_2 thin film electrodes, at 50 mV/s	73
Figure 5.11:	Oxidation of $K_3Fe(CN)_6$ at glassy carbon electrode in 0.001 M H_2SO_4 at 400 mV/s	74
Figure 5.12:	Tafel plot for Sb_2O_5/SnO_2 with $K_3Fe(CN)_6$ at 25 mV/s (— = I_c , - - = I_a)	75
Figure 5.13:	Tafel plot for ZrO_2/SnO_2 with $K_3Fe(CN)_6$ at 25 mV/s (— = I_c , - - = I_a)	76
Figure 6.1:	Randles equivalent circuit	80
Figure 6.2:	Diagram of coating flat cell used for impedance measurements	82
Figure 6.3:	Mixed metal oxide electrode interface in solution of interest	84
Figure 6.4:	(a) Complex plot: uncoated titanium over full frequency spectrum (b) Bode plot: uncoated titanium over full frequency spectrum...	85
Figure 6.5:	Complex plane of uncoated Ti, high frequency region expanded	86
Figure 6.6:	Equivalent electrical circuit for uncoated titanium	88
Figure 6.7:	Capacitance vs voltage plot for uncoated Ti interface	90
Figure 6.8:	Three different equivalent circuits for systems with two rate limiting electrode processes (a) Voigt model (b) Ladder model and (c) Mixed model	91
Figure 6.9	(a) Complex plot of Ti/SnO_2	92
	(b) Bode plot of Ti/SnO_2	93
Figure 6.10:	Unique plot for Warburg impedance (Z' —, Z'' - -) based on Ti/SnO_2 electrode/solution interface data	94
Figure 6.11:	Complex plot of $Ti/SnO_2/CuO$	96

Figure 6.12:	Electrical equivalent circuit for CuO/SnO ₂	97
Figure 6.13:	Complex plot of Ti/SnO ₂ /CuO showing the first experiment (black) and the repeat experiment (gray)	98
Figure 6.14:	Capacitance vs voltage curves for the Ti/SnO ₂ /CuO thin film (♦ High frequency semicircle; ■ middle frequency semicircle; ▲ low frequency semicircle)	99
Figure 6.15:	Complex plot of Ti/SnO ₂ /MnO _x electrode/solution interface	100
Figure 6.16:	Capacitance–voltage plot for Ti/SnO ₂ /MnO ₂ electrode in H ₂ SO ₄ ...	102
Figure 6.17:	Complex plot of Ti/SnO ₂ /PdO ₂ electrode in H ₂ SO ₄	103
Figure 6.18:	Capacitance–voltage plot for Ti/SnO ₂ /PdO ₂ electrodes in H ₂ SO ₄ ...	103
Figure 6.19:	Complex plot of Ti/SnO ₂ /ZrO ₂ electrode in 0.001 M H ₂ SO ₄	105
Figure 6.20:	Complex plot of Ti/SnO ₂ /Sb ₂ O ₅ electrode in 0.001 M H ₂ SO ₄	107
Figure 6.21:	Capacitance voltage plots for the (---▲---) Ti/ SnO ₂ /Sb ₂ O ₅ and the (---■---) Ti/SnO ₂ /ZrO ₂ electrodes in 0.001 M H ₂ SO ₄	109
Figure 6.22:	(a) Determination of q _{tot} from charge vs scan rate plots	111
	(b) Determination of q _{out} from charge vs scan rate plots	111
Figure 7.1:	Electrical equivalent circuits representing oxidation of K ₃ Fe(CN) ₆ at Ti/SnO ₂ /Sb ₂ O ₅	119
Figure 7.2:	Complex plot of oxidation of K ₃ Fe ₃ (SCN) ₆ at Ti/SnO ₂ /Sb ₂ O ₅ electrode at 200 mV to 300 mV.....	120
Figure 7.3:	Complex plot of oxidation of K ₃ Fe(CN) ₆ at Ti/SnO ₂ /ZrO ₂ at 200 mV to 300 mV	122
Figure 7.4:	Oxidation of hydroquinone at Ti/SnO ₂ /Sb ₂ O ₅ electrode at 600 mV to 700 mV	124

Figure 7.5:	Complex plot of oxidation of hydroquinone at Ti/SnO ₂ /ZrO ₂ electrode at 1200 mV to 1300 mV.....	125
Figure 7.6:	Oxidation of phenol at Ti/SnO ₂ /Sb ₂ O ₅ electrode at 1200 mV to 1500 mV	127
Figure 7.7:	Complex plot of oxidation of phenol at Ti/SnO ₂ /Sb ₂ O ₅ electrode, with the high frequency region expanded	128
Figure 7.8:	Complex plot of oxidation of phenol at Ti/SnO ₂ /ZrO ₂ electrode at 1400 mV to 1500 mV.....	129
Figure 7.9:	Complex plot of oxidation of phenol at Ti/SnO ₂ /ZrO ₂ electrode, with the high frequency region expanded	130
Figure 8.1:	Reaction scheme for anodic oxidation of phenol	139
Figure 8.2:	Bulk electrolysis of a 0.019 M phenol solution at ZrO ₂ -SnO ₂ electrode, for 1 hour	140
Figure 8.3:	Calibration curves for phenol and its breakdown products (◆ phenol, ■ catechol, ▲ hydroquinone, ● quinone)	141
Figure 8.4:	An example of a chromatogram obtained for the products of phenol bulk electrolysis (6 hours)	142
Figure 8.5:	Phenol degradation at ZrO ₂ /SnO ₂ electrode (—◆— phenol, -■-- hydroquinone,--▲--- quinone)	143

Chapter one

Introduction and objectives

1.1 Transition metals as catalysts

One of the most characteristic chemical properties of transition metals, is the occurrence of multiple oxidation states. Many transition metal compounds can be used as homogeneous catalysts, since they readily inter-convert between oxidation states. In this way they can act as intermediates for the exchange of electrons between the reactants. Enzymes act as homogeneous catalysts in living systems and their active sites are often transition metals [1].

Many important examples of heterogeneous catalysis also employ transition metals as catalysts. In heterogeneous catalysis the catalyst is usually a solid and the reactants are in the gas phase. The activation energy is lowered because the catalyst adsorbs the reactants onto its surface and holds them close together in an orientation that favours reaction. Some examples are given in Table 1.1 [2].

Table1.1: Some examples of important industrial processes that make use of transition metal catalysts.

Process	Catalyst
Ziegler-Natta polymerization	Ti(IV)chloride
Contact process for making sulphuric acid	V(V)oxide
Decomposition of hydrogen peroxide	Mn(IV)oxide
Hydrogenation of vegetable oils to produce margarine	Ni, Pd, Pt
Ostwald process for making nitric acid	Pt, Rh
Vehicle exhaust system catalytic converters	Pt-Rh alloy

We would like to show that the catalytic ability of transition metals in heterogeneous catalysis can also be extended to electrocatalysis. Electrocatalysis requires the incorporation of the transition metal catalyst into a suitable host material, for production of thin film electrodes. The resultant thin film should be homogeneous in its chemical composition and stable under anodic conditions, with respect to chemical and mechanical weathering. Therefore, in the production of thin film electrodes the chemical and electrical nature of the host material is as important as the catalytic ability of the electrode, induced by the dopant element.

1.2 Tin oxide as electro-catalyst host material

SnO₂ films have many unique properties, which make them suitable for electroanalytical, electrochemical and photo-electrochemical applications. SnO₂ films show very little absorbance in the visible *ir*-range, are very resistant against chemical attack, have high mechanical strength, good electrical conductivity when doped, relatively high hydrogen and oxygen over voltages and can easily be prepared as thin film electrodes. Therefore, SnO₂ films meet the general requirements for dimensionally stable electrode host material [3].

These properties make it an attractive choice for electrode material in spectroscopic studies. SnO₂ has a band gap of ~ 3.7 eV and when used as a thin film electrode material usually contains oxygen vacancies in the lattice. Additionally it can also be prepared to contain donor atoms such as Cl or Sb, which raises its n-type carrier capacity to values in excess of 10²⁰ cm⁻³ and consequently the potential conductivity to well above 10 ohm⁻¹.cm⁻¹. The electrodes retain their semiconducting properties and the exchange currents are low [4].

Tin oxide can be used solely for its electrical properties as a gas sensor or as bulk electrodes to oxidise organics in wastewater. Pure tin oxide is polycrystalline in nature and its conductivity is believed to be due to a defect structure with oxygen deficiencies and/or interstitial tin as well as the incorporation of chlorine impurities in the crystalline lattice of the cassiterite structure [5,6]. The microstructure of tin oxide, which can be controlled by deposition parameters, also greatly affects its electrical properties. Factors such as film thickness and deposition temperature impact on electrical conductivity [7]. Perfect control over deposition parameters in the development of industrial gas sensors, have many

advantages ie. miniaturisation which implies power reduction, microelectronic compatibility for use in multi sensors, mass production of sensors and good reproducibility.

The bulk grain electrical properties depend on the structural defect generated by introduction of dopant atoms. Foreign atoms are introduced in the search for increased sensitivity and selectivity of the sensing layer at milder operating conditions. Dopants are introduced in an effort to obtain a large dispersion of small particles through the whole base material. Additives can also modify the microstructure of the host material, control the grain growth mechanism and introduce donor or acceptor levels.

1.3 Some applications of doped tin oxide electrodes

The electrochemical behaviour of a fluorine doped tin oxide electrode in a solution of LiClO_4 in propylene carbonate was investigated. Mass changes were detected using a quartz crystal microbalance and the formation of a LiOH coating was observed on the electrode surface, which was assumed to be due to the reduction of water. It was also established that the coating was porous allowing ions to move inside it [8].

Tin doped iron oxides were synthesized and characterised to investigate the influence of tin on the sensing properties, of doped iron oxides, for gases such as methane and carbon monoxide. The structural characterisation was done using X-ray powder diffraction and

Mössbauer spectroscopy. Structural detail was obtained for the inclusion of tin in the inverse spinel related and corundum related iron oxide structures [9].

SnO₂ doped with WO_x was prepared and characterised as thick films and nanosized powders to test its sensitivity as a sensor for CO and NO₂ gases, since it is well known that WO₃ is very sensitive to NO_x. In order to improve sensitivity and selectivity of semiconducting oxides it is necessary to reduce the particle size of the material and nanosized particles can effectively be obtained using sol-gel technology. The addition of W to SnO₂ was found to lower the conductance of the film in air. It lowers the response of tin oxide to CO but enhances its ability to sense NO₂ [10].

The addition of small amounts of vanadium oxide to tin oxide provides a higher sensitivity to alkyl-aromatics and alcohols [11].

Colloidal solutions of antimony doped tin oxide nanoparticles (4-9 nm, diameter) have been prepared successfully in an autoclave at high temperatures. These were characterised by the same strong absorption band in the red to IR region, giving them a characteristic blue colour, which is related to the level of doping. Films of tin oxide at low levels of Sb doping are transparent throughout the visible region, and are widely used in photovoltaic and optoelectronic devices. They have been prepared by various methods and annealing at high temperatures, producing films with good electrical conductivity. Nanoparticulate antimony doped tin oxide has been used as the electrochromic material for the production of printed, electrochromic displays [12,13].

Zr/Ni amorphous alloys have been prepared as electrocatalytic materials for hydrogen evolution. The electrocatalytic activity of these alloys was further enhanced by chemical etching, which removes any oxide layers that may form on the surface [14].

High density capacitors require high dielectric constant thin films. The films should have large charge storage capacity, high breakdown field and low leakage current density. ZrO_2 is one of the main dielectric thin film materials reported in literature, along with others such as TiO_2 , Ta_2O_5 and mixed oxides of Ba, Sr and Ti. Good quality zirconium tin titanate thin films have been prepared by the sol-gel-technique, which is a good technique for stoichiometric control and introduction of dopants. These thin films were designed for application in ultra large scale resonators, filters and microwave substrates [15]. Mesoporous zirconium oxide was prepared in the presence of surfactants, also using sol-gel technology. The expanded surface area, pore size distribution and phase structure of ZrO_2 was directly affected by synthesis conditions, i.e. preparation composition of Zr/ H_2O and Zr/surfactant, the presence of stabilizers, as well as the type of catalysis used (acid or base) [16].

Thin conductive films on a variety of substrates have been increasingly employed as electrode surfaces. The films are composed of noble metals (vapour deposited or evaporated) or prepared from thermally decomposed and deposited metal oxides. These films were primarily used to study charge transfer processes but when coated onto transparent substrates these films also find use in areas where optical transparency in

combination with good electrochemical behaviour is required, as in optoelectronic devices eg. solar cells and liquid crystal displays [17]. Wide band gap semiconductors such as tin oxide and indium oxide exhibit good optical transparency in the visible light spectrum as well as high electrical conductivity. Control over the optical transparency and electrical conduction is dependent on the method of preparation of the thin film. Optical transparency requires good crystallinity whereas the electrical properties can be modified by creating well defined structural defects such as oxygen vacancies and substitutional or interstitial doping of foreign atoms.

1.4 Motivation for the dissertation

We have seen from literature that there are many examples of mixed metal oxide electrode materials for various applications. Good candidates as starting materials for alloys seem to be early to late transition metals alloys, since alloying of such metals can generate electronic structures with high catalytic activity. Amorphous alloys (of which the composition can be gradually changed) tend to be very homogeneous and have coordination sites, which are unsaturated in many cases and can generate strong catalytic activity. An iron modified cobalt oxide anode system and a nickel oxide anode have both demonstrated the successful degradation of phenol to carboxylic acids and CO_2 [18,19]. A mixed metal oxide system prepared from SnO_2 as host material, was also successful in the complete degradation of phenol. SnO_2 doped with Sb_2O_5 showed improved catalytic ability for phenol oxidation, compared to Ebonex/ PbO_2 electrodes [20].

1.5 Overall Aim of the thesis

The demand for new materials exhibiting good electrocatalytic properties, as alternatives to traditional electrodes, leads the research into ever new compositions and structures. We would like to investigate the possibility of using SnO_2 as host material and doping it with selected transition metal oxides (PdO_2 , MnO_x , CuO , and ZrO_2), thereby producing a new class of electrodes, with improved catalytic activity. The transition metal oxides which have been selected for the purpose of this dissertation, are recognized as reducing gas sensors. Harnessing the characteristic ability of transition metals to switch oxidation states, we would like to explore the forced application of these transition metal oxides, as oxidative electrocatalysts. Throughout this dissertation the work of Grimm et al (SnO_2 doped with Sb_2O_5 for successful phenol oxidation) was used as a reference point.

1.6 Objectives

Mixed metal tin oxides have great potential in electro-catalysis and electro-analytical chemistry. We have seen from literature how structural and electrical properties influence catalytic ability of the thin film electrodes, hence it is important to be able to control and characterise the morphology and electrical properties of mixed metal oxides. Consequently, we have prepared tin oxide electrodes by the sol-gel technique, with very low dopant levels, with the following objectives in mind:

- ❖ Sol-gel preparation of a novel class of transition metal doped tin oxide electrodes at very low transition metal dopant ratios
- ❖ Characterisation of all prepared thin films using:
 - Thermogravimetric Analysis [TGA]
 - UV/vis Spectroscopy [UV/vis]
 - X-ray diffraction [XRD]
 - Atomic Force Microscopy [AFM]
 - Scanning Electron Microscopy [SEM]
 - Particle Induced X-ray Emission [PIXE]
 - Rutherford Backscattering [RBS];
- ❖ Investigation of interfacial electrochemistry of the thin films as electrodes in acidic medium, using cyclic voltammetry [CV]
- ❖ Determination of the oxidative ability of the doped tin oxide electrodes prepared, using single electron and multiple electron exchange couples
- ❖ Testing of selected mixed metal oxide electrodes, as effective catalysts for phenol combustion
- ❖ Monitoring of the extent of phenol conversion by bulk electrolysis experiments.
- ❖ Analysis of phenol oxidation intermediates by refined High Performance Liquid Chromatography [HPLC] methods
- ❖ Evaluation of the electrical properties of the mixed metal oxide interfaces in acidic medium by electrochemical impedance spectroscopy [EIS]
- ❖ Evaluation of charge transfer at the mixed metal oxide/solution interface, in the presence of electron exchange couples by electrochemical impedance spectroscopy [EIS]

1.7 Significant contributions of the dissertation

- ❖ Refining sol-gel technology for the preparation of mixed metal oxides;
- ❖ Full characterisation (*surface morphology* and *electrochemical*) of all prepared mixed metal oxide electrodes;
- ❖ Mechanistic evaluation of oxidation reactions at complex metal oxide systems;
- ❖ Electrochemical impedance evaluation of charge transfer at complex metal oxide interfaces,
- ❖ Evaluation of the bulk electrical properties of complex metal oxide materials, using electrochemical impedance spectroscopy [EIS]

1.8 Layout of the dissertation

A theoretical background to the subject of mixed metal oxide synthesis and characterization is given, followed by the electrochemical evaluation of the prepared electrocatalysts. An example of an application of the new technology is given i.e. the use of a zirconium modified catalyst for phenol combustion. The dissertation is concluded with a brief summary of how the objectives were met and the main scientific contributions will be highlighted. The main conclusions and some suggestions for future research are also given.

A schematic lay out of the experimental approach used in the dissertation is given (Figure 1.1).

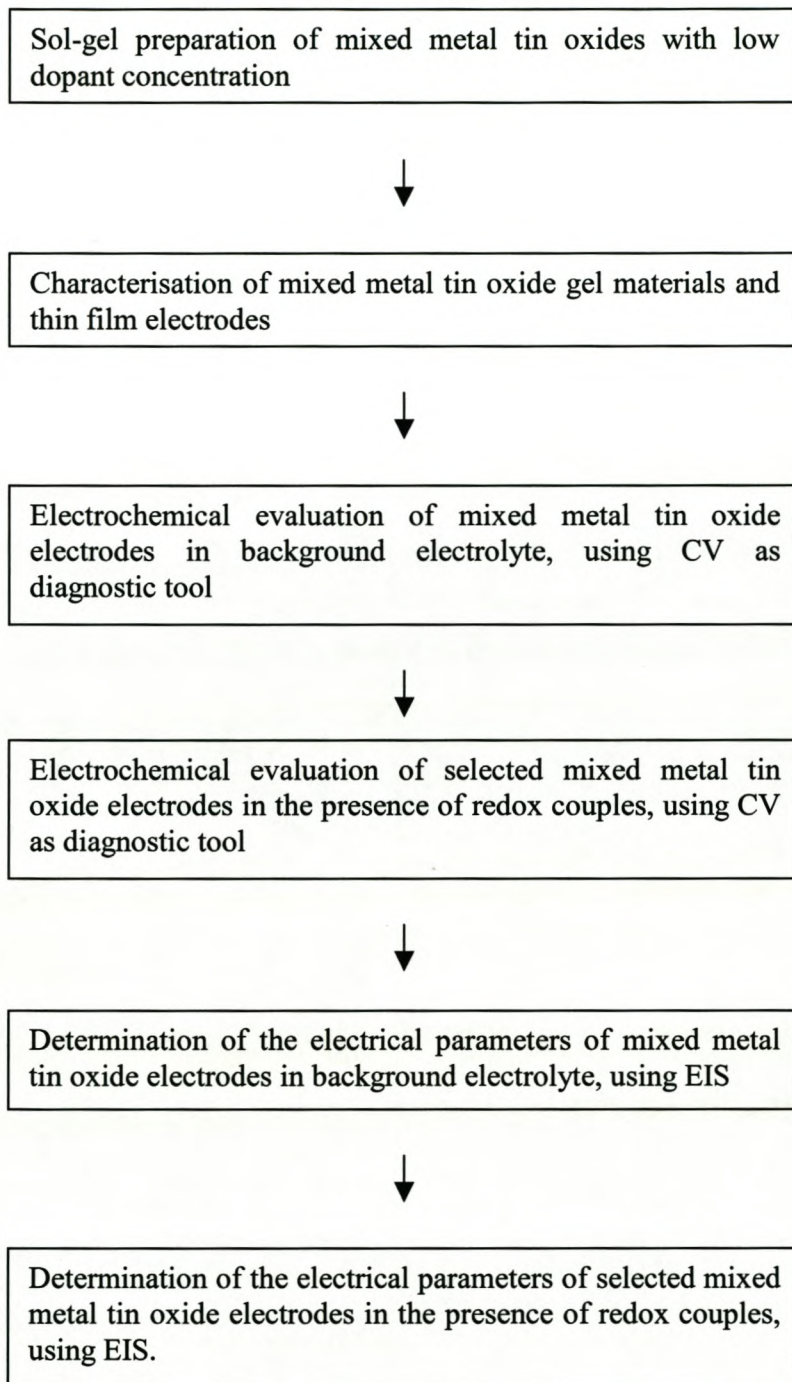


Figure 1.1: Experimental lay out of the research carried out in this dissertation.

Chapter two

Theoretical background

2.1 Introduction

A brief overview of the requirements for good catalysts will be given, followed by some perspective on the catalytic ability of the transition metal elements selected for introduction into the SnO₂ host material. The theoretical background of the main techniques used in the course of the research will be discussed. This includes a brief overview of sol-gel technology, analytical techniques used in characterisation of electrode surfaces, cyclic voltammetry and impedance spectroscopy.

2.2 Requirements for efficient electrocatalysts

Oxygen evolution from water is an unwanted side reaction in organic oxidation reactions. An efficient electrocatalyst will suppress the oxygen evolution reaction, while still being electrocatalytically active towards the oxidation of organics. This impacts on the energy efficiency per unit volume of water treated. An electrocatalyst with a high oxygen overpotential, allows the electrode potential to be increased for improved rates of oxidation, without excessive oxygen formation. Metals with highly conductive stable oxide layers eg. transition metal based alloys, have displayed

high catalytic activity, whilst providing good separation between organic oxidation potentials and the potential for oxygen evolution [21].

Anodes can be classified into two classes based on their potential toward the evolution of oxygen during combustion of organics. Examples of class one anodes (high potential towards the oxygen evolution reaction (*oer*)) are Sb doped SnO₂ and F doped PbO₂. Class two anodes (anodes with low potential toward *oer*) include Ir-based oxides and mixed Ir/Ti oxides [22]. Industrial anodes presently, are generally class two anodes customarily based on a RuO₂ active agent and a TiO₂ stabilising agent. In the design of dimensionally stable anodes it is common practice to substitute IrO₂ as an active agent, especially for gas evolving anodic reactions in acidic media. Additional components can be added to enhance selectivity or to increase anodic stability [23]. The chemical nature and morphology of the anode have a great influence on the extent of anodic oxidation of organics in wastewater and the oxidation pathway [24].

2.3 Disadvantages of metal oxide electrodes

Some of the problems associated with metal oxide anodes are (i) passivation of the electrode surface as a result of oxidised organic material and (ii) the limited lifetime of the anode material due to electrochemical corrosion.

Phenol, a common target molecule in wastewater treatment experiments, produces oligomers (high molecular weight polymers) as products in the oxidation process. These remain on the electrode surface causing passivation of the electrode, limiting

the lifetime of the electrode. Passivation interferes with the supply of fresh reactant to the electrode surface and also the removal of products from the reaction zone (also called active sites). Passivation also decreases the available over potential to drive the oxidation reaction [25]. During the anodic oxidation of phenol at the surface of a platinum electrode, a yellow brown polymeric product was formed. The formation of the polymeric film was related to the experimental conditions. Alkaline media (pH > 9), low current density and high phenol concentrations favoured polymeric film formation [26].

Extreme anodic conditions (i.e. prolonged application of anodic potentials or very high positive potentials) during electrolysis affect the lifetime of electrodes, since the electrode material itself undergoes oxidation. Prolonged electrolysis of Ti/SnO₂-Sb₂O₅ anodes, showed that the anode was deactivated after 12 hours of electrolysis and that 80% of anode coating material was corroded [27].

2.4 Transition metal oxide electrocatalysts

The sensing function of a semiconducting metal oxide, like SnO₂, is based on the chemical interaction between the surrounding gas and the oxide surface. To improve the selectivity and sensitivity of such metal oxides, catalysts (eg. Pt, Pd, Ag and Au) can be added to SnO₂ [28].

Manganese oxides are well known as chemical oxidation catalysts. Manganese oxides in combination with other transition metal elements have been used as

catalysts for oxidation of various organic compounds [29,30,31]. A nanoporous amorphous manganese oxide was prepared via sol-gel, as an electrocatalyst for the successful reduction of oxygen in alkaline solution. The amorphous material owns more active sites than crystalline manganese oxide and its nonporous morphology is an advantage in the design of effective gas diffusion electrodes [32].

Copper and copper oxides have been reported to be effective catalysts for several environmental processes eg. reduction of NO, oxidation of CO and the decomposition of N₂O [33,34,35]. Fibreglass coated with copper oxides showed catalytic activity for the oxidation of ethanol in a stream of air at different temperatures [36].

2.5 Selected transition metal doped SnO₂ materials for electrocatalytic investigations

The transition metal oxide dopants selected for the purpose of the current research, have been prepared for specific applications by other authors [37,38,39,40]. CuO-SnO₂ powders were prepared by two different sol-gel methods in order to obtain nanocrystalline particles which would assist greatly in its marketability as an industrial electrocatalytic surface. ZrO₂-SnO₂ was synthesized via the sol-gel route and prepared as thin films to test the sensitivity of the doped system in H₂S monitoring and in an attempt to lower the high working temperature needed for SnO₂ based gas sensors. Mn-SnO₂ powders were prepared through a chemical route in order to obtain a dense SnO₂ ceramic under conventional sintering conditions. Pd-SnO₂ thin films were prepared by the sol-gel route followed by spin coating in order to improve the selectivity and sensitivity of the SnO₂ sensor to H₂ and CO.

By introducing transition metals, which have known catalytic ability, into the SnO₂ host material in this dissertation, we will strive to produce a class of anodes with high potential towards the oxygen evolution reaction. This type of electrode material should be ideally suited for organic waste combustion. It is envisaged that the control over surface morphology and chemical composition of thin films that can be obtained by using sol-gel technology and dip coating methods, will produce effective electrocatalysts, in this class of anodes.

2.6 Sol-gel techniques

Sol-gel chemistry is widely used to prepare inorganic and organic-inorganic composite materials. It is simple technology involving hydrolysis of precursors to produce a sol (colloidal suspension of small particles) and condensation to produce the gel (a rigid porous structure), under relatively mild conditions. Gelation takes place during the ageing process, which can range from a few seconds to months, depending on the processing conditions [41]. Sol-gel synthesis of mixed metal oxides is not new technology. It has emerged as an effective preparative route providing control over surface area, surface composition and particle size, which are among the important factors affecting electrocatalytic behaviour of oxide electrodes [42,43,44]. By increasing the ageing time, for instance, the densification of the gel material prepared by sol-gel, is improved. The reactivity of the sol-gel product is favoured by densification of the gel product.

2.7 Characterisation tools and methods

The transition metal doped tin oxide electrodes were characterised in terms of surface morphology and electrode interface electrochemistry, using AFM, SEM, RBS/PIXE, CV and EIS. UV/vis and TGA provided some useful information about the physical and chemical properties of the mixed metal oxide gels prepared by sol-gel. In particular the electrochemical characterisation of this novel class of electrodes, represents a major contribution to the field of mixed metal oxide electrocatalyst development.

2.7.1 *Thermogravimetric analysis*

Thermal analysis measurements employ a continuous heating rate of a sample (usually linear with time) and the observation of changes to the sample as a result of the applied heating ramp. The result of such measurement is a thermal analysis curve showing distinct features (peaks, changes of slope, discontinuities), which can be related to thermal events. In thermogravimetric analysis (TGA), the sample property measured is mass and the changes to mass that occur during the heating cycle. However thermal analysis techniques can also be used to measure properties such as temperature (differential thermal analysis, DTA), evolution of radioactive gas (emanation thermal analysis, ETA) and enthalpy changes (differential scanning calorimetry, DSC) to name but a few [45]. Only TGA was used for the characterization of the mixed metal oxides prepared in this work.

2.7.2 *UV/vis spectroscopy*

UV/vis spectroscopy is based on the absorption of light by a sample as the wavelength is varied over a selected range determined by the light source used. UV/vis spectroscopy was used to determine the band gap energy for Sb_2O_5 , ZrO_2 , CuO , MnO_x and PdO_2 doped tin oxide gels prepared by sol-gel. In order to measure band gap energy (eV) a line was drawn tangent to the onset of the first peak and another line, extending the baseline absorbance measurement, was drawn. From the intersection of these two lines, a wavelength reading was obtained and related to a band gap energy using the following equation (Equation 2.1)

$$E = hc/\lambda \quad (2.1)$$

With c , the speed of light ($3 \times 10^8 \text{ m}\cdot\text{s}^{-1}$); h , Planck's constant ($6.626 \times 10^{-34} \text{ Js}$) and λ , wavelength in nano meters.

2.7.3 *X-Ray methods*

The discovery of X-rays (1895) provided radiation with the appropriate wavelength (10^{-10} m) that would allow the structure of matter to be probed at the atomic level. X-rays for diffraction are produced by bombarding a metal target, often Cu or Mo, with a beam of electrons emitted from a heated filament. The incident beam will ionize electrons from the K shell of the target atoms and X-rays are emitted as the resultant vacancies are filled by electrons from the L or M shells. As the atomic number of the target element increases the energy of the characteristic emissions increases and the wavelength decreases. Monochromatic beams of specific wavelengths can be selected by reflecting an X-ray from a crystal monochromator (according to the Bragg equation, $\lambda = 2d\sin\theta$) or using a filter. The Bragg equation represents the

condition for diffraction to take place. X-ray diffraction can be applied to powders and single crystal materials. The X-ray pattern of a compound provides a characteristic fingerprint which can be used in quantitative analysis. Precise values of d -spacings (property of the material) and estimated line intensities can be compared to extensive powder diffraction database files [46].

2.7.4 *Microscopy*

2.7.4.1 *Scanning electron microscopy (SEM)*

Scanning electron microscopy employs a beam of electrons directed at the sample by means of a set of condenser lenses and deflector coils. Points on the surface of the specimen generate low energy secondary electrons, which are converted into a very low current by a detector. The current is then amplified and used to control the brightness of the cathode ray tube in order to produce a magnified image of the specimen. In SEM the formation of a magnified image is achieved without the use of lenses, therefore the image cannot suffer the aberrations which are unavoidable when using lenses and the image information is carried as a current in a wire and can in turn be amplified and manipulated in a variety of ways. The resolution of SEM is however the limiting factor since it is dependent on the diameter of the electron beam. The SEM operates only in vacuum, it can resolve nanometer features but depth information is not readily quantifiable [47].

2.7.4.2 *Atomic force microscopy (AFM)*

In scanning probe microscopy (SPM) a mechanical probe is responsible for the generation of the image. The probe is moved across the surface in a raster pattern and moves up or down to maintain a constant distance from the sample surface.

These raster movements and up and down movements are monitored by laser reflection changes and are converted to a three dimensional image of the sample surface by a computer. A SPM can operate in ambient, liquid or vacuum to resolve features in three dimensions. The various types of SPM differ only in the method that is used to sense the sample and in the relationship between the probe and the sample. Other types of SPM include “Force” sensing of the sample and “Near-Optics” sensing. AFM measures very small forces at very small distances in order to obtain images at the molecular level. The forces are measured by placing the probe on a very small spring cantilever, which deflects according to attractive and repulsive forces between the probe and the surface. It is also possible to study attractive forces between semiconductors and a metal coated tip, with varying applied voltage, using AFM. The relationship between attractive forces and applied voltage is recorded as force spectra. The force spectra can provide information about electronic structure i.e. energy gap, electron affinity, ionization energy and density of state. A charge transfer model has been developed for selected organic crystals, using AFM, which can successfully relate their force spectra to their electronic structures. [48].

For materials of mixed composition, the phase contrast regime of AFM can be used to identify location and size of particles as a different phase to that of the host material. Nanostructured metal (Sn, Pd, Cu) polymers and metal oxide polymer composites have been prepared. Phase contrast AFM images could clearly distinguish between the dark polymer spherulite regions and the lighter regions indicating the presence of the metal. Surface imperfections were recognizable deviating their shape from spheroid [49].

2.7.5 *Nuclear probe methods*

2.7.5.1 *Rutherford backscattering (RBS)*

RBS is based on the elastic backscattering of incoming ions by nuclei in the sample. A purely elastic collision is defined as one where the incoming particle does not have enough energy to penetrate the Coulomb barrier surrounding the nucleus and the scattering process obeys classical laws. The criterion for elastic scattering is met when an α -particle is used at energies of up to 2 MeV and for this reason, helium ions are extensively used [50]. Backscattered electrons are those that suffer collisions resulting in their re-emergence from the surface. RBS relies on the measurement of the energy of the backscattered ion at a well defined angle in order to determine the mass of the scattering nuclei. The fraction of incident electrons backscattered is strongly dependent on the atomic number of the element and the surface topography, which affects the surface angle. Two principal types of detectors are used for electron detection i.e. scintillation detectors and solid state detectors. Even though the RBS spectrum is generally more difficult to interpret than PIXE spectra, it is simplified by the use of the well tested simulation computer program RUMP, which is used universally for all but the most complex spectra [51].

2.7.5.2 *Particle induced X-ray emissions (PIXE)*

An incoming ion will eject an inner core electron from its orbit, resulting in a vacancy which is rapidly filled by an electron from one of the outer shells. The release of energy as a result of this transition, is equal to the energy gap between the adjacent shells and is characteristic of the parent atom. Measuring this characteristic X-ray with a X-ray detector with sufficient resolution, provides an indication of the atomic composition of the sample. Particle induced X-ray emission (PIXE) is sensitive to

the parts per million and most of the elements can be measured in the same analysis run.

Becoming more popular is the combination of Rutherford backscattering (RBS) with PIXE using protons to bombard the sample. RBS is used for matrix determination and depth profiling and PIXE is used for elemental analysis. The RBS/PIXE combination, using protons is particularly useful for thin samples, where the peaks due to scattering from the light elements (e.g. C, N₂, O₂) are easily resolved in the RBS spectrum. The incoming ion in other applications could also be a helium ion (α -particle) or even a deuterium ion, although deuterium beams have been little used since they emit neutrons in various nuclear reactions, which interfere with detection limits [52]. Thus the PIXE/RBS combination has been established as an excellent tool for the study of biological materials ranging from applications in medicine, agriculture and botany as well as the identification of unknown coatings on optical elements e.g. laser crystals and lenses [53].

2.8 Cyclic voltammetry

Cyclic voltammetry is a potential sweep technique that is particularly useful in the area of preliminary mechanistic investigations. During a potential sweep the potential at which redox reactions occur can be readily determined. From the sweep rate dependence coupled homogeneous reactions and complications, such as adsorption, can be identified. Cyclic voltammetry is nearly always the method of choice when studying an electrochemical system for the first time, although undoubtedly other methods exist for investigating specific kinetic detail.

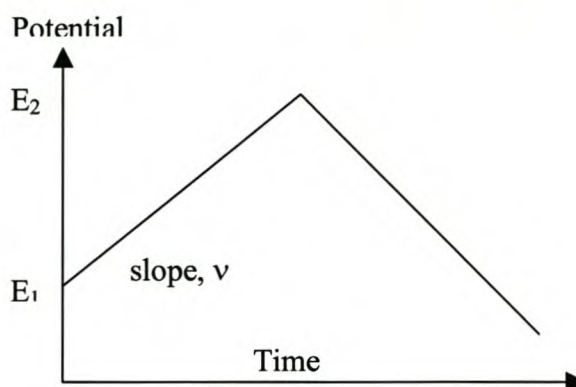


Figure 2.1: Potential–time profiles for sweep voltammetry.

In linear sweep voltammetry a sweep is performed on the electrode potential between E_1 and E_2 at a known sweep rate and stopped after reaching E_2 (Figure 2.1). In cyclic voltammetry the initial sweep is the same as in linear sweep voltammetry, but instead of stopping when E_2 is reached the potential is reversed and the sweep can continue until E_1 is reached or can be taken beyond E_2 to a potential E_3 . The cell current is recorded as a function of the applied potential. The sweep rate can vary from a few $\text{mV}\cdot\text{s}^{-1}$ up to a few hundred $\text{V}\cdot\text{s}^{-1}$, but at these high values, the application of the technique is restricted by experimental complications such as double layer charging and large iR_u drop (uncompensated resistance) effects. A good approach to obtaining high quality data at fast scan rates is the use of microelectrodes which minimize both the charging effects and the uncompensated resistance effects. The method for recording the voltammogram depends on the sweep rate used. Generally for very fast sweep rates (in the order of $\text{mV}\cdot\text{s}^{-1}$) a microcomputer interfaced with a potentiostat-galvanostat is required to capture all the information during the sweep and avoid distortion of the voltammogram [54].

2.8.1 Cyclic voltammetry as a diagnostic tool for determining the reversibility of redox reactions

Under steady state conditions, concentrations above a certain distance away from the electrode are kept constant by natural convection. Within the region next to the electrode, the concentration gradients are essentially linear and the ratio of oxidized to reduced species for a reversible reaction is given by the Nernst equation (Equation 2.2).

$$E_e = E_e^\circ + \frac{RT}{nF} \ln \frac{C_O}{C_R} \quad (2.2)$$

Where E_e is the equilibrium potential (V), E_e° is the standard electrode potential (V), R , T , n and F are the usual constants and C_O and C_R the surface concentrations of oxidized and reduced species.

The concentration gradient at the surface, changes as a result of applied potential. A current, proportional to this gradient, flows in the external circuit. As you increase the sweep rate of a CV oxidation experiment, you shorten the time scale of the experiment and the concentration gradient has less time to relax. Therefore, at fast sweep rates, you will develop high concentration gradients with resulting large currents. The relationship between peak current density and sweep rate is mathematically illustrated by the Randles-Sevcik equation (Equation 2.3).

$$I_p = -0.4463 nF (nF/RT)^{1/2} C_o^\infty D^{1/2} v^{1/2} \quad (2.3)$$

Where I_p is the peak current density ($A.cm^{-2}$), D is the diffusion coefficient ($cm^2.s^{-1}$), v is the sweep rate ($V.s^{-1}$) and C_o^∞ is the concentration of electroactive species ($mol.cm^{-3}$).

The proportional relationship between peak current density and square root of the sweep, should give a straight line passing through the origin for a completely reversible reaction. Deviations from this relationship can be related to quasi reversibility or complete irreversibility. Another related test is the separation between oxidation peak potential (E_a) and reduction peak potential (E_c) given by Equation 2.4:

$$\Delta E = E_a - E_c = 59/n \text{ (mV)} \quad (2.4)$$

where n is the number of electrons involved in the reaction.

Nernstian diffusion in the region adjacent to the electrode surface and the related equations, form the basis of the evaluation of the interfacial region of the novel electrode surfaces in the background electrolyte [54,55].

2.9 Electrochemical impedance spectroscopy

Electrical resistance is understood as the ability of a circuit element to resist the flow of electrical current. Ohm's law defines resistance as the ratio between voltage (E) and current (I) (Equation 2.5):

$$R = \frac{E}{I} \quad (2.5)$$

Ohm's law is however restricted to the ideal resistor, which has several simplifying properties amongst which is the assumption that the resistance of the ideal resistor is independent of frequency (56). The real world however is made of circuit elements, which do not behave ideally and therefore this simple concept of resistance, does not always apply.

Impedance is used to replace the simple concept of resistance in instances where systems do not behave ideally and deviate from Ohm's law.. Impedance is also a measure of the ability of a circuit element to resist the flow of electrical current, but the limiting assumptions of Ohm's law do not apply. Electrochemical impedance is usually measured by applying an *ac* potential to an electrochemical cell and measuring the current through the cell. If the input signal (potential) is sinusoidal, the response would be an *ac* current signal containing the excitation frequency and its harmonics (70).

Electrochemical impedance is normally measured using a small amplitude perturbing signal to ensure that the cell's response is pseudo linear. For a species being oxidized or reduced in solution an equilibrium is established at some time such that concentration of oxidized species is equal to concentration of reduced species for a reversible one electron transfer (Equation 2.6).

$$[O] = [R] \quad (2.6)$$

the potential at equilibrium is given by Equation 2.7:

$$E_e = E^\circ + RT/nF \ln[O]/[R] = E^\circ \quad (2.7)$$

Since $\ln[O]/[R] = 0$; $E_e = E^\circ$

Therefore, in electrochemical impedance spectroscopy a small amplitude perturbation signal is used in the region of E_e . In the equilibrium region we find a pseudo linear current voltage relationship. This can be seen in the typical S-shaped curve obtained for one electron oxidation reactions (Figure 2.2).

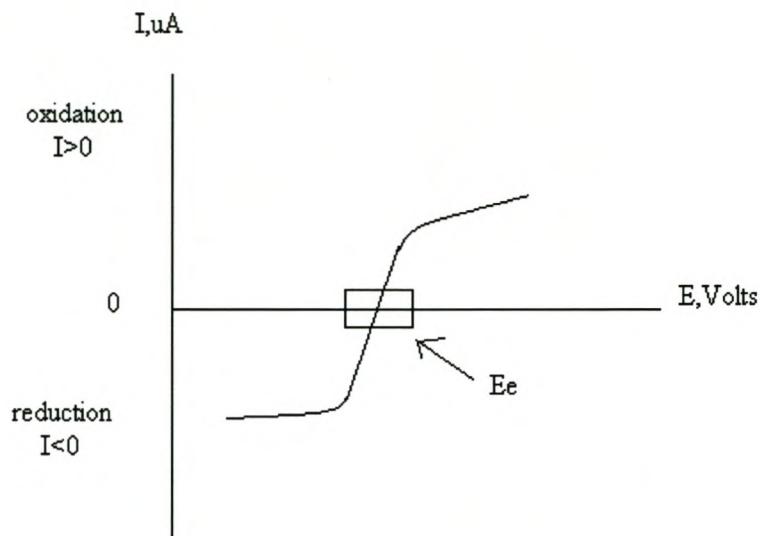


Figure 2.2: Current-voltage plot for an oxidation reduction reaction with $O=R$ and $O + e^- \leftrightarrow R$.

The amplitude of the excitation signal should have an amplitude small enough to validate the assumption of linearity represented by this equilibrium region. In a pseudo linear system, the current response to a sinusoidal potential will be a sinusoid at the same frequency but shifted in phase (70).

The excitation signal expressed as a function of time, has the form (Equation 2.8)

$$E(t) = E_0 \cos(\omega t) \quad (2.8)$$

With $E(t)$ the potential at time t , E_0 is the amplitude of the signal and ω is the radial frequency, in radians per second (Equation 2.9).

$$\omega = 2\pi f \quad (2.9)$$

f , is frequency in Hz.

The current response signal ($I(t)$), is shifted in phase (φ) and has a different amplitude, I_0 given by Equation 2.10:

$$I(t) = I_0 \cos(\omega t - \varphi) \quad (2.10)$$

An expression analogous to Ohm's law allows us to calculate the impedance of the system (Z) according to Equation 2.11:

$$Z = \frac{E(t)}{I(t)} = \frac{E_0 \cos(\omega t)}{I_0 \cos(\omega t - \varphi)} = Z_0 \frac{\cos(\omega t)}{\cos(\omega t - \varphi)} \quad (2.11)$$

The impedance is therefore expressed in terms of a magnitude, Z_0 , and a phase shift.

2.9.1 Electrochemical Impedance Spectroscopy data presentation

It is possible to express the impedance as a complex function using Euler's relationship (Equation 2.12).

$$\exp(j\varphi) = \cos\varphi + j\sin\varphi \quad (2.12)$$

The potential ($E(t)$) is described by Equation 2.13.

$$E(t) = E_0 \exp(j\omega t) \quad (2.13)$$

The current $I(t)$ is given by Equation 2.14.

$$I(t) = I_0 \exp(j\omega t - j\varphi) \quad (2.14)$$

The impedance is then represented as a complex number with a real and imaginary part as represented by Equation 2.15.

$$Z = E/I = Z_0 \exp(j\varphi) = Z_0(\cos\varphi + j\sin\varphi) \quad (2.15)$$

Plotting the real part (represented in the diagram by Z') on the X-axis and the imaginary part (represented in the diagram by Z'') on the Y-axis gives rise to the Nyquist plot, also known as Complex plane diagrams (Figure 2.3).

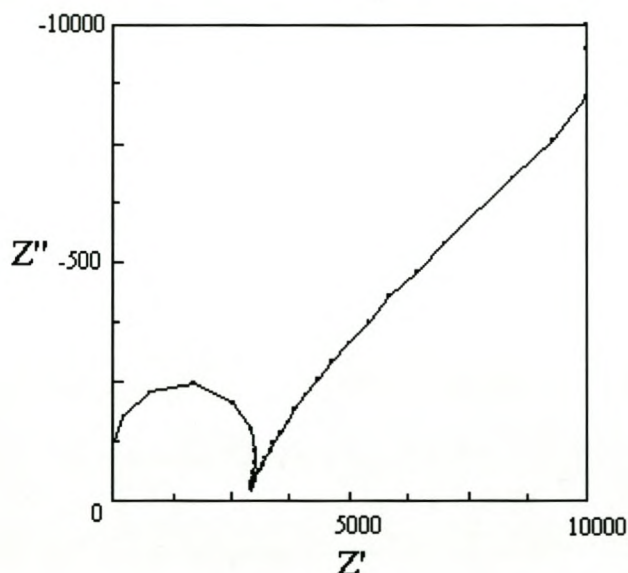


Figure 2.3: Complex plot of EIS data for $O + e^- \rightleftharpoons R$, both soluble species.

In the complex plot the semicircle at low values of Z' , corresponds to the high frequency region. In electrochemical impedance spectroscopy the high frequency region is usually interpreted as the electrical properties of the bulk electrode material under investigation. The low frequency region (high Z' values) provides information about the interfacial region in an electrochemical cell.

The magnitude and phase angle of the impedance vector can be plotted individually to obtain the Bode plots.

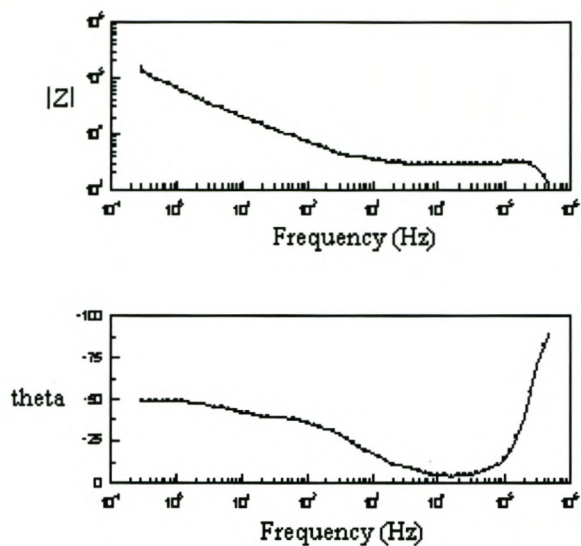


Figure 2.4: Bode plots: magnitude (top) and phase angle (bottom) change vs frequency.

If we know the phase as a function of frequency, we can deduce the way in which the amplitude of the impedance is changing. These plots show the real component change in impedance (the $|Z|$ plot) and the imaginary component (theta plot), separately. A 45° phase angle in the low frequency region is typically associated with diffusion controlled impedance at the interface (70, 71).

Chapter three:

Preparation of mixed metal tin oxides

3.1 Introduction

Thin film mixed metal tin oxides of transition metal doped SnO₂ were prepared using sol-gel technology. The opportunity for increasing the surface area of the mixed metal tin oxides, by adding surfactants during sol-gel synthesis, was explored. This was compared to the use of porous substrate to effect increased surface area of the electrode. Increased surface area of electrodes will result in improved catalytic efficiency.

3.2 Experimental conditions

3.2.1 Sol-gel preparation of mixed metal oxide electrodes

Sol-gel involves solvolysis of organic or inorganic precursors, followed by condensation and ageing. A schematic representation of the sol-gel process is given in Figure 3.1. The cationic precursors in sol-gel preparation were either chloride salts (Sb, Pd) or organic derivatives (Cu, Zr). In the case of manganese doping, citrate derivatives of manganese and tin were preferred. The manganese citrate derivative was freshly prepared before sol-gel synthesis, from MnCO₃ by precipitation and filtration. The organic solvent in all cases was absolute ethanol, except for zirconium doping, where the solvent was methanol.

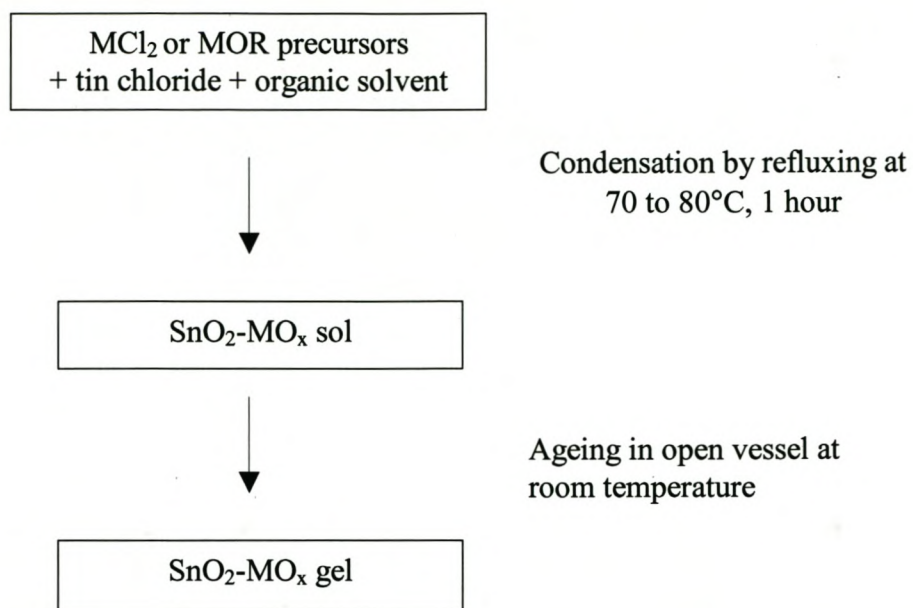


Figure 3.1: Schematic representation of sol-gel process (M represents the dopant metal as described in the text).

The doping ratios were kept as low as possible, using literature references as a guideline (Table 3.1). The doping ratio was determined according to the following formula :

$$\text{Doping ratio} = n_i / \Sigma n$$

Where n_i is the number of moles of dopant atom and n is the total number of moles (moles of SnO_2 + moles of dopant)

Table 3.1: Doping ratios for mixed metal tin oxides

Starting materials	Dopant	Ratio
$\text{SnCl}_2 \cdot 2\text{H}_2\text{O}$, SbCl_3 ⁽²⁰⁾	Sb_2O_5	10mol%
$\text{SnCl}_4 \cdot 5\text{H}_2\text{O}$; $\text{Cu}(\text{CH}_3\text{COO})_2 \cdot \text{H}_2\text{O}$ ⁽³⁷⁾	CuO	2.5 wt%
$\text{SnCl}_2 \cdot 2\text{H}_2\text{O}$; $\text{Zr}(\text{OC}_3\text{H}_7)_4$ ⁽³⁸⁾	ZrO_2	1 mol%
citric acid, tin citrate, ethylene glycol, nitric acid, manganese citrate ⁽³⁹⁾	MnO_2	5 mol%
$\text{SnCl}_2 \cdot 2\text{H}_2\text{O}$; PdCl_2 ⁽⁴⁰⁾	PdO_2	1 mol%

In all cases the solutions were well stirred and refluxed before being left to age at room temperature for at least 24 h to ensure sufficient ageing of the gel. The gel obtained was evaporated to dryness to produce a powder. The powder was obtained by subjecting the gel solution to the same annealing cycle (maximum temperature of 600° C, ramp rate of 1° C/min) as that used for the preparation of the thin films. The resultant powder samples were submitted for XRD analysis. For the purpose of casting the thin films, the gels were retained in the liquid form. The gels were found to be stable at room temperature for up to 6 months when stored in the absence of direct light.

3.2.2 Preparation of thin film electrodes

Thin films were prepared by dip coating sol-gel techniques. The major advantages of this technique over other techniques such as spray pyrolysis, chemical vapour deposition and RF sputtering (radio frequency electromagnetic wave energy (e.g.,

13.65 MHz, etc.) is utilized to energize the sputtering operation) are: high purity starting material, easy coating of large and complex shaped substrates and low cost [44].

This technique produces high quality mixed metal SnO₂ thin films as far as structure and morphology are concerned. Experimental conditions can be readily controlled to ensure reproducibility. The dip coating mechanism is similar to that described by Grimm *et al* [20].

The spin coated samples were prepared by spinning samples at a fixed speed for a fixed period of time on a rotating disk. The substrate was mounted onto the rotating disk of a domestic angle grinder with Prestik® (Figure 3.2). Two to three drops of the gel were placed on the substrate using a pasteur pipette. The grinder was operated at full speed for 10 seconds to ensure reproducibility of spin coatings. The thin film was formed as a result of the centrifugal force during spinning.

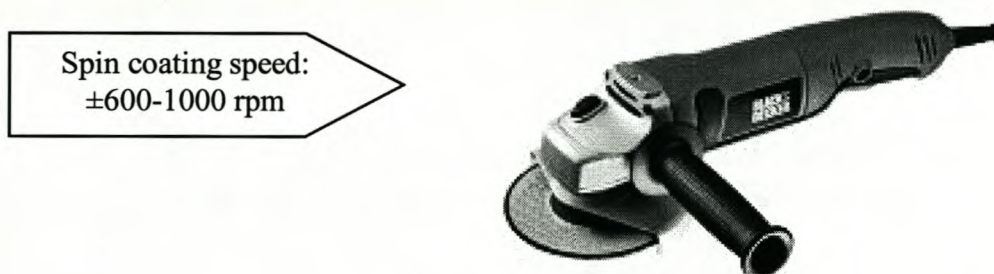


Figure 3.2: An example of the domestic grinder used as rotating disk in spin coating of thin films.

The spin and dip coated films were coated once, allowed to dry at 100°C for 30 minutes in a standard laboratory oven, before the second coating was applied. All the films prepared by dip coating and spin coating were then annealed in a tube furnace (LABOFURN, quartz tube) fitted with a model 7 temperature controller, in an open atmosphere. The samples were heated at a ramp rate of 60°C per hour and kept at 600°C for one hour, before being allowed to cool again to room temperature. The effect of spin coating the mixed metal oxides onto the titanium substrates, as opposed to dip coating, was investigated in terms of film thickness and surface features such as cracks.

Thin film electrodes were constructed by connecting copper wire to the back of the titanium substrate using a conductive adhesive (Farnell InOne 6500 CHEMENCE). The back of the coated film and the electrical contact was then isolated from contact with the solution in the electrochemical cell using non-conductive nail enamel. The only part of the electrode exposed to the analytical solution was the thin film electrocatalyst coating (Figure 3.3).

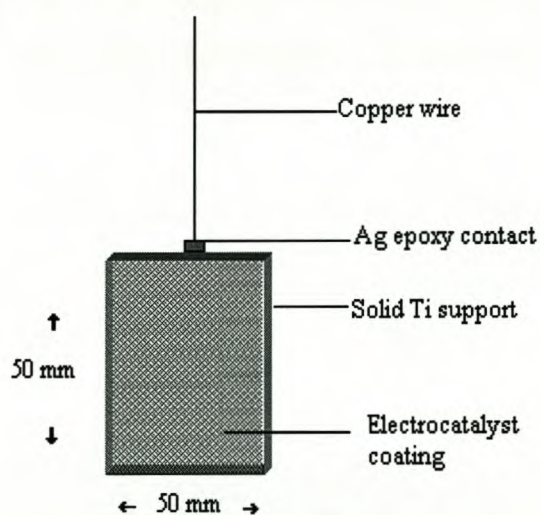


Figure 3.3: Design of mixed metal tin oxide coated electrode.

3.3 Properties of electrodes with increased surface area

The surface area of an electrode may not necessarily be the most important factor for the design of practical electrocatalysts. Factors such as durability, optimum catalytic activity and selectivity of the electrodes are often as important factors especially in industrial oxide electrodes. However, oxide electrodes with a large surface area usually give high catalytic activities, although the surface area does not always correlate with its electrocatalytic performance. A large electrochemically active surface area implies that the voltammetric charge is almost the same as the pseudocapacitance. The pseudocapacitance reflects the charge of the electrical double layer and large double layer capacitances are of interest in a wide range of applications where charge needs to be stored [57].

Various parameters affect the surface area of dip coated oxide electrodes e.g. the types of metal complexes and alcoholic solvents, the concentration of the metal complexes, drying time and temperature, annealing temperature, number of dip coating cycles, amongst others. Over and above these considerations there are also different methods of preparing large surface area metal oxide electrodes i.e. (a) adding a salt (sodium carbonate) to the dip coating solution (b) doping of the host metal oxide with additional metal ions (c) doping with rare earth elements with subsequent dissolution by acid to form meso-pores (d) addition of a salt catalyst in a sol-gel process to produce ultrafine metal oxide particle and (e) the preparation of layered metal oxide structures [58].

The use of surfactants such as cetyltrimethylammonium bromide (CTAB) co-entrapped with dopant molecules within sol-gel matrices has been shown to effectively modify the cage properties and therefore dopant properties and functionalities of the sol-gel

matrices. The performance of an extensive series of pH indicators were modified in this way by the co-entrapment of CTAB in the tetramethoxysilane (TMOS) sol-gel matrix [59].

The use of templates such as porous alumina membranes with fixed pore arrays and pore densities can also provide metal oxide electrodes with increased surface area. The template membrane is dipped into the metal oxide solution, dried and annealed. The template membrane can then be dissolved by immersion in a suitable solution in order to expose the unsupported metal oxide electrode. In this way micro- and nano-structures of metal oxides can be prepared for use as electrodes [60].

In this study, the gels were mixed with surfactants hexadecyltrimethylammonium bromide (CTAB, $C_{19}H_{42}NBr$) and decyltrimethylammonium bromide (DTAB, $C_{13}H_{30}NBr$) in an attempt to introduce porosity via the gel into the final thin film.

3.4 Experimental

3.4.1 Method 1: using surfactants

The surfactants were added as solids to the gel mixture until the formation of the micellar structure was observed under the microscope (100 to 1000 x magnification). The critical micelle concentrations (*cmc*) for the surfactants in aqueous solutions at 25°C, 1 atm, were used as a guide for predicting the formation of micelles in the gel. The values of *cmc* were 0.9 mM (CTAB) and 65 mM (DTAB) [61]. The modified gel was coated onto a solid titanium substrate and then annealed in the tube furnace.

3.4.2 Method 2: using porous substrate

Commercial porous titanium was used as substrate in the preparation of electrodes with increased surface area. The titanium was cut to produce porous electrode surfaces of 1 x 1 cm. Here the porosity was controlled by the design of the substrate, rather than modification of the coating material.

3.5 Results and discussion

3.5.1 Method 1: using surfactant

The purpose of using a surfactant was so that it would act as a template for introducing regular porosity into the thin film. As the modified film undergoes heating it was anticipated that the surfactant would decompose and volatilize, leaving behind controlled porosity. The use of DTAB (a linear carbon chain, C₁₀) produced better defined micelles in the gel than CTAB (a linear carbon chain, C₁₆) did. Using CTAB, the formation of micelles was observed after just exceeding the *cmc* i.e. at approximately 1.1 mM CTAB solutions. Using DTAB as surfactant, micelle formation was observed at concentrations of about 50-60 mM DTAB.

The micelles introduced into the mixed metal oxide gel by using surfactants were not of a regularly repeating shape and not necessarily circular. During the relatively mild annealing conditions (1°C/minute) the micelles did not retain their shape long enough to produce well defined pores, but in fact decomposed as a result of increased surface strain. The surfactant modified mixed metal oxide thin films consequently, displayed surface cracks and irregular depressions, as can be seen with SEM at 2000X

magnification (Figure 3.4). This further contributed to the uncontrolled nature of the increased surface area.

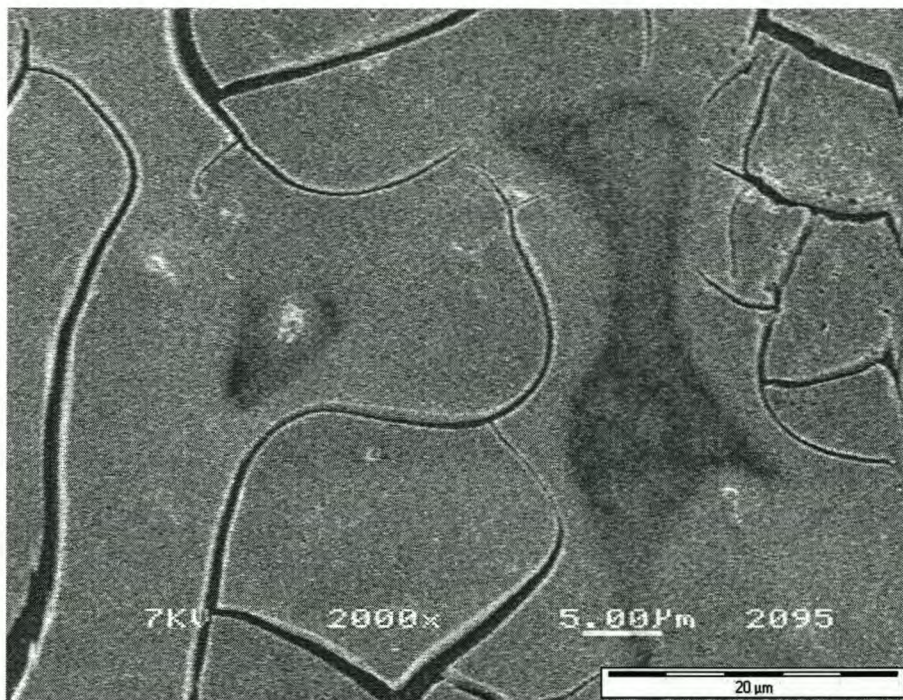


Figure 3.4: SEM of ZrO₂-SnO₂ modified with DTAB

3.5.2 Method 2: using porous substrate

The increased surface area of the electrode surface produced using a porous substrate, is directly related to the shape of the substrate. Therefore the thin film coating on the porous electrodes, have predictable enlarged surfaces. The dip coating method was used to produce well coated surfaces on porous titanium substrates (Figure 3.5). For the purpose of comparing data obtained by the various analytical tools used to characterise the transition metal doped tin oxide electrodes, it is important to have good reproducibility between electrodes.

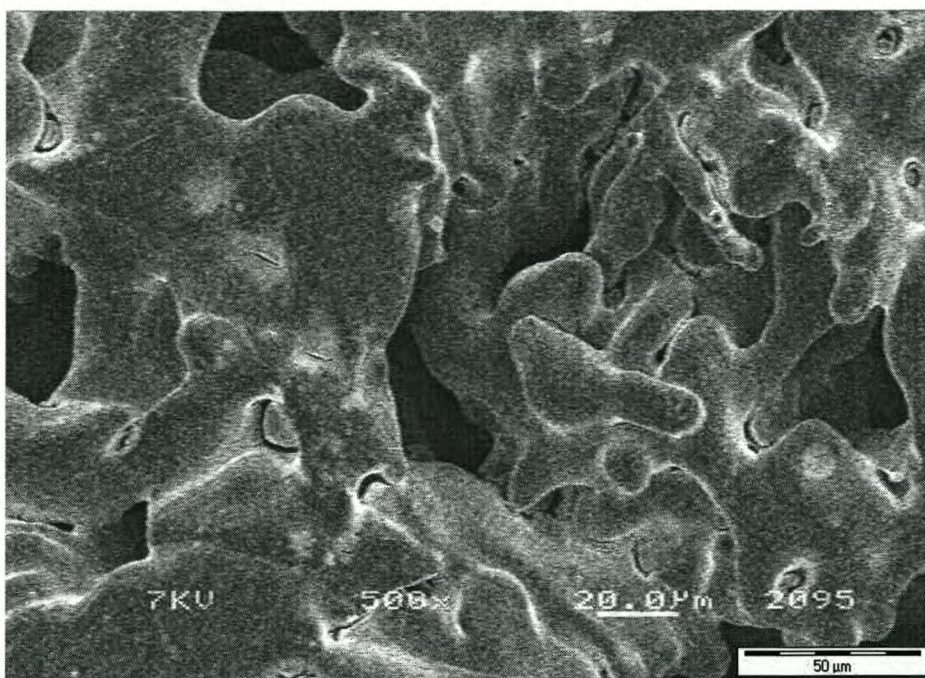


Figure 3.5: SEM of ZrO₂-SnO₂ coated onto porous titanium substrate.

3.6 Conclusion

Improving porosity by means of adding surfactants to the mixed metal oxide gels and thereby creating electrodes with increased surface area, was not effective in the sense of introducing regularly repeating, micelle shaped pores. Very little reproducibility could be established in the electrochemical response of surfactant modified thin films electrodes. This can be understood in terms of the irregular nature of the surface morphology of surfactant modified thin films.

To explore the benefit of increased surface area on reactivity of the electrode surface, electrochemical characterisation experiments (cyclic voltammetry) and electrocatalytic reactivity testing (bulk electrolysis) were performed on the electrodes prepared on porous titanium.

For evaluation of electrochemical interface kinetics (electrochemical impedance spectroscopy) and surface morphology characterisation, however, solid titanium was used as coating surface. The use of porous electrodes in the coating flat cell used for impedance measurements, would lead to leakage of the test solution during experiments. The advantage of increased surface area of the electrodes, are thus not applicable to the results obtained by EIS.

The solid titanium substrate was used during surface characterisation to avoid contours of a porous substrate interfering with the evaluation of the thin film morphology.

Chapter four

Characterisation of mixed metal tin oxides

4.1 Introduction

The mixed metal tin oxide materials prepared via the sol-gel route were extensively characterised. TGA analysis was performed to confirm that at 600°C (the calcination temperature) no further structural changes due to mass loss occur. UV spectroscopy of the gels allowed the determination of the band gap energy. The surfaces of the thin film electrodes were characterised by X-ray diffraction (XRD), atomic force microscopy (AFM), scanning electron microscopy (SEM), Rutherford backscattering (RBS) and particle induced X-ray emission (PIXE) analysis provided some insight into the chemical composition of the mixed metal tin oxides.

4.2 Experimental

4.2.1 Thermogravimetric analysis

Small sample masses are used in TGA to ensure uniform heating of sample and to reduce exchange of gas with the surrounding atmosphere. A concentrated gel material was prepared for TGA by evaporating the solvent of a small volume of the original gel. The

sample was analysed on a Perkin Elmer TGA (7 series). The heating rate was 1°C/min up to a maximum of 600°C and nitrogen was used as purging gas.

4.2.2 *UV/vis spectroscopy*

A Unicam, Helios Gamma, UV spectrophotometer and Aurora 1.1 scanning software version was used for the collection of the data. The instrument was used in single beam mode. Absolute ethanol (solvent used in preparation of mixed metal oxide gels) was used as a reference. The gel samples were diluted 1:1 with absolute ethanol to obtain absorbance readings on an appropriate scale. The band gap energy (eV) was measured by extrapolation of the first absorbance peak, usually observed between 300 to 400nm.

4.2.3 *X-ray diffraction*

Samples of the mixed metal tin oxide gels were evaporated to dryness and the resulting powders were analysed by X-Ray diffraction (XRD). Measurements were made on a Siemens advanced D8 diffractometer (Bruker AXS) with primary (Cu tube, variable divergent slit) and secondary (NaI(Th)) scintillation, variable anti-scatter slit) detectors. The incident angle was set as 2θ for all measurements. Energy dispersive X-ray fluorescence (EDXRF) was useful in the quantitative analysis of the Cu doped thin film composition, in particular.

4.2.4 *Scanning electron microscopy*

SEM pictures of the surfaces were obtained at 500 x and 5000 x magnification using a Topcon scanning electron microscope, model ABT60. The microscope was operated in secondary electron detection (SED) mode at an accelerating voltage of 20 kV. The working distance was 10 mm, the samples were tilted 20° and they were not coated for viewing.

4.2.5 *Atomic force microscopy*

AFM micrographs were taken at two different positions on each film that was prepared using a Topometrix Explorer TMX 2000. Two measurements on the same sample was done to improve representation of the entire surface morphology, since the sample surface is not homogeneous. The samples were scanned in non-contact mode (i.e. the probe is oscillated in the attractive regime). A low resonance frequency cantilever was used and the force spring constant was 35-65 N/m.

4.2.6 *Particle induced X-ray emission/ Rutherford backscattering*

Compositional analyses of the mixed metal oxides cast as thin films were obtained by the combination PIXE/RBS technique. The sample was bombarded with protons and the energy of the beam was kept at 3 eV. A selected section of the surface (5 µm x 5 µm) was bombarded with protons and taken to be representative of the total surface composition (5 mm x 5 mm). The backscattered energy was recorded using an X-ray detector. Semi-quantitative on-line imaging was made possible by the use of the GEO-PIXE suite of programmes. Compositional analysis (ppm of element) is based on matrix determination

and depth profiling (film thickness) provided by RBS. PIXE/RBS and XRD analyses were done at the nuclear microprobe facility at Ithemba Labs, Faure, South Africa.

4.3 Characterisation results and discussion

4.3.1 Thermogravimetric analysis

The TGA profiles obtained for the synthesized gels are in good agreement with published TGA profiles for Zr, Pd and CuO doped SnO₂ [38,62,63]. In all cases, an initial 10 to 20% weight loss was assigned to the evaporation of the organic solvent. Subsequent major weight loss between 100 to 200 °C is ascribed to evaporation of water, salts and organic compounds. The only possibilities for further weight loss after the oxides are formed, is loss of oxygen. ZrO₂ maintains its 4+ oxidation state throughout the heating cycle. ZrO₂ only decomposes above 2677°C [73]. Sb₂O₅ however decomposes by losing oxygen at 380°C to form Sb₂O₃, which is stable up to 655°C [74]. The similarities in the decomposition profiles of antimony doped and zirconium doped tin oxide, can be related to the high oxidation state of the final oxide product during the heating cycle. CuO and MnO₂ doped tin oxide follow a similar decomposition pattern and the similarities can be attributed to the fact that in both of these mixed oxides the dopant metal center has an oxidation number of II. CuO is stable up to 1336°C but MnO₂ decomposes above 535°C to form MnO [75,76]. It is possible that the decomposition temperature of MnO₂ could be lowered when incorporated in to the SnO₂ matrix. PdO₂ decomposes to form PdO at comparatively low temperature i.e. 200°C. PdO is then stable up to 750°C [77]. Any further loss of oxygen by this oxide will give rise to elemental Pd, therefore the most stable

phase possible for palladium oxides, is reached. The decomposition profiles obtained by TGA are not influenced by the decomposition of the host material, which is stable as SnO_2 up to temperatures of 1630°C [78]. TGA has confirmed that all mixed metal tin oxides form stable phases before the maximum temperature used in the annealing of prepared mixed metal oxide thin films, i.e. 600°C (Figure 4.1).

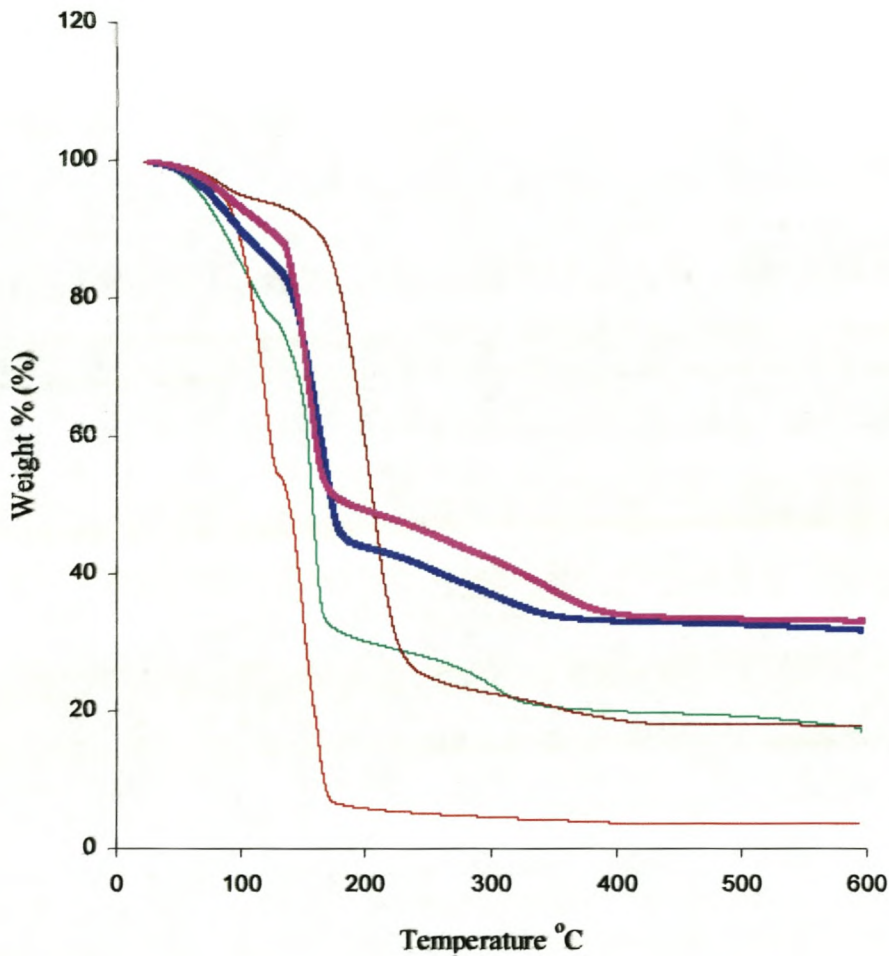


Figure 4.1: TGA of metal oxide doped tin oxide gels (pink - $\text{ZrO}_2/\text{SnO}_2$; blue - Sb_2O_5 ; green - CuO ; brown - MnOx/SnO_2 ; red - $\text{PdO}_2/\text{SnO}_2$).

4.3.2 UV/vis spectroscopy

The band gap energies for all mixed metal tin oxides were determined to be between 2.37 to 3.37 eV (Table 4.1).

Table 4.1: Band gap energy values of the mixed metal tin oxide gels prepared

Gel composition	E _{bg} , Ev
SnO ₂	3.30
SnO ₂ /CuO	3.03
SnO ₂ /PdO ₂	2.37-2.47
SnO ₂ /Sb ₂ O ₅	3.34
SnO ₂ /ZrO ₂ (2002)	3.30
SnO ₂ /ZrO ₂ (2003)	3.37
SnO ₂ /MnO _x	-

The band gap energy (eV) for each mixed metal oxide was determined from the onset of the absorption in the UV region, as illustrated in Figure 4.2. A typical calculation of band gap energy is shown below.

$$E = hc/\lambda$$

Planck's constant, $h = 6.626 \times 10^{-34}$ J.s and the speed of light, $c = 3 \times 10^8$ m.s⁻¹. The appropriate conversion of units gives; 1 eV = 1.602×10^{-19} J and 1 nm = 1×10^{-9} m. The wavelength, λ in nm, is obtained from the UV absorption graph.

$$E \text{ (eV)} = [(4.14 \times 10^{-15} \text{ eV.s}) \times (3 \times 10^{17} \text{ nm.s}^{-1})] / \lambda \text{ nm}$$

Solving the equation gives E, the band gap energy in units of eV.

$\text{PdO}_2/\text{SnO}_2$ was the only mixed metal tin oxide which gave a band gap energy lower than that of undoped tin oxide. Such a lowering of the band gap energy means that the conductivity of the doped material is improved as a result of the addition of the dopant. The $\text{MnO}_2/\text{SnO}_2$ sample gel was obtained in the form of a dispersion rather than a clear solution and this complicated the absorbance measurements, even after dilution. It was therefore not possible to determine the band gap energy for this particular mixed metal oxide composition.

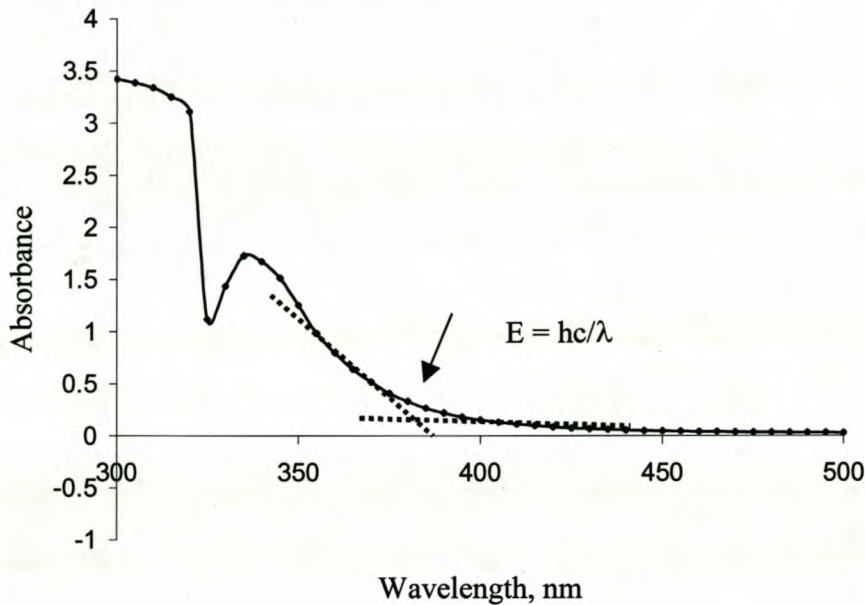


Figure 4.2: An example of how band gap energy was measured for $\text{ZrO}_2\text{-SnO}_2$.

Three samples of $\text{ZrO}_2/\text{SnO}_2$ gels were collected over time to observe the effect of long term ageing on the absorbance response of the gels. Two samples of the zirconium doped tin oxide which were prepared a year apart (March, 2002 and September, 2003) showed distinctly different absorptions at 340 nm (Figure 4.3). The absorption peak for the 2002

sample was at least 1 absorbance unit bigger than that of the 2003 sample. As the sample ages with time the extent of cross-linking increases and the gel becomes more dense or crystalline. This increase in cross-linking of the sample due to the ageing process is reflected in the larger absorbance for the aged samples.

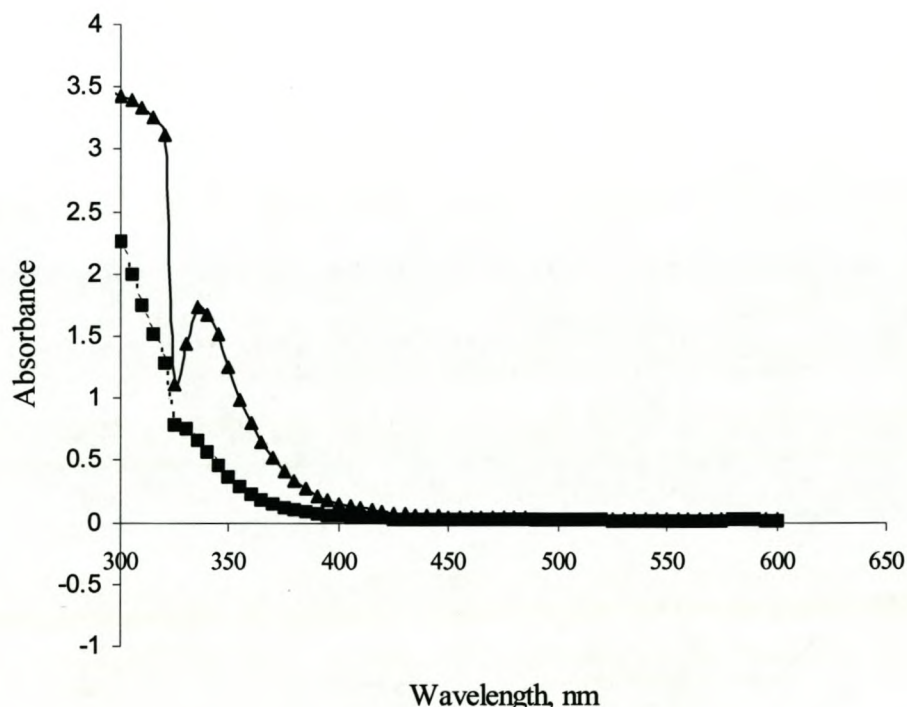


Figure 4.3: The effect of ageing on $\text{SnO}_2/\text{ZrO}_2$ (-▲-2002 and --■--2003 samples)

4.3.3 X-ray methods

XRD was able to confirm the characteristic peaks for SnO_2 when compared to the JCPDS file number 21-1250 (Cassiterite syn SnO_2) for the mixed metal oxide powders (Figure 4.4). Peaks for the identification of the dopant atom were however not always observed since the very low dopant ratio of 1 mol% is beyond the capability of the instrument used. In a study of $\text{SnO}_2/\text{ZrO}_2$ prepared as 95:5 wt% composition, XRD could

only confirm the crystalline cassiterite structure. Thus at 5 wt% ZrO_2 doping the refinement of the lattice parameters were in good agreement with that of bulk SnO_2 [63]. XRD of ZrO_2 thin films grown by photo-induced chemical vapour deposition, showed weak intensity bands at 30.4° and 35° , which could be assigned to the tetragonal and monoclinic phases respectively. This confirmed that ZrO_2 layers grown in this manner start to crystallize at a deposition temperature of $250^\circ C$ [65]. Energy dispersive X-ray fluorescence (EDXRF) was able to positively identify the copper in CuO/SnO_2 . XRD could not confirm the presence of the dopant atoms.

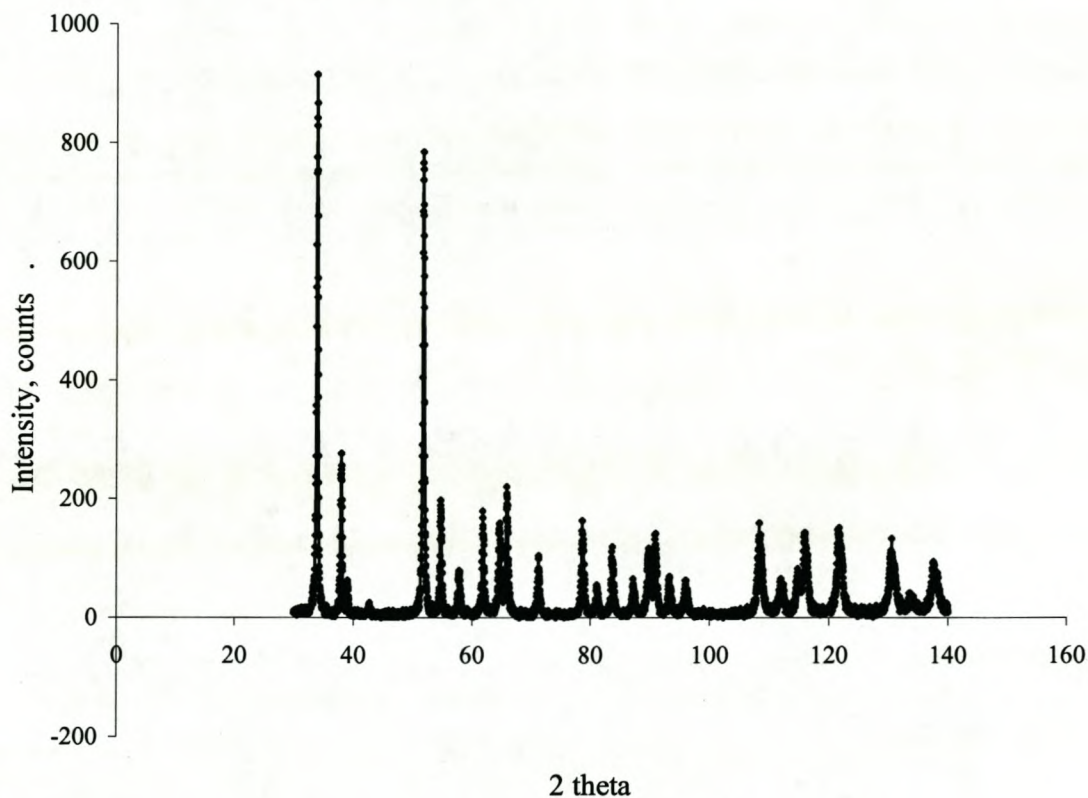


Figure 4.4: XRD pattern for $Zr-SnO_2$ powder showing only the characteristic peaks for SnO_2 .

4.3.4 Scanning electron microscopy

Scanning electron micrographs reflected well coated surfaces in most cases for spin coating as well as dip coating. The Cu-doped surfaces (spin coated) showed a lighter and a darker area at 500 x magnification which could be due to an uneven concentration distribution.

The Zr-doped spin coated surface showed dramatic fragmentation at 500 x magnification. Increase in the doping level of Zr in the tin oxide host material gave rise to clusters or island formation as a result of exclusion (Figure 4.5a). Pd-doped spin coated surface produced a cauliflower like surface as a result of agglomeration of metal oxide particles (Figure 4.5b). Noble metals like palladium, readily oxidize in air forming a layer of touching oxide particles. These oxide particles can be reduced back to metallic palladium by further heating (up to 500°C) in a reducing atmosphere, giving rise to the agglomeration of metal oxide and metallic particles observed [28].

The agglomeration observed for zirconium and palladium doped tin oxide, were confirmed by repeat coatings and are therefore characteristic of the coating composition. The spin coated thin films showed greatly enhanced surface roughness compared to dip coated films of the same composition.



Figure 4.5: SEM of (a) ZrO₂-SnO₂ spin coated thin film.

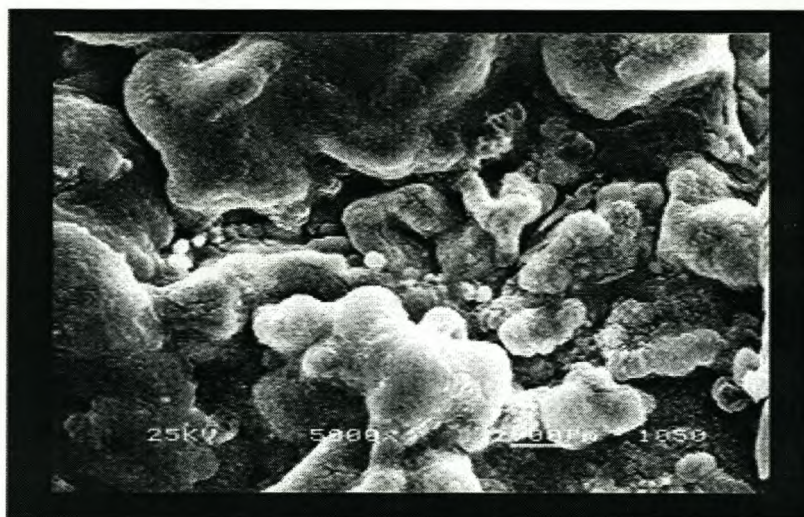


Figure 4.5: SEM of (b) PdO₂-SnO₂ spin coated thin film.

4.3.5 Atomic force microscopy

Atomic force micrographs of Sb_2O_5 doped thin films showed greater surface roughness for the dip coated than the spin coated surfaces. The dipping process leads to the formation of regularly repeating triangular patterns on the thin film electrode surfaces. For the Pd doped surfaces the spin coated surfaces were observed to be more textured than the dip coated surfaces. Mn doped thin films presented a scale-like effect on the dip coated surfaces due to the drag during the dipping process (Figure 4.6a). The spin coated thin films have the same features, but with reduced surface roughness (Figure 4.6b).

The spin coated surfaces showed less surface roughness and appear smoother. The Zr and CuO doped thin films appear much smoother than the Mn films but the surface characteristics were otherwise similar. The atomic force microscope that was used, was not able to detect much more than surface morphology. It was not possible to get pictures at atomic level and investigate molecular or atomic bond structure. We were limited by the capabilities of the instrument available for use. Information of this nature would enable structural analysis of thin film surface composition.

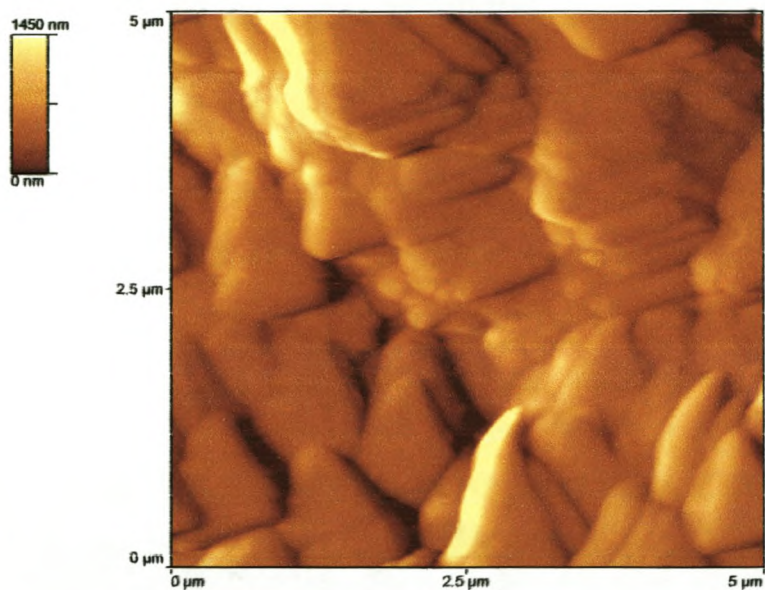


Figure 4.6: AFM of (a) dip coated $\text{MnO}_x/\text{SnO}_2$ films.

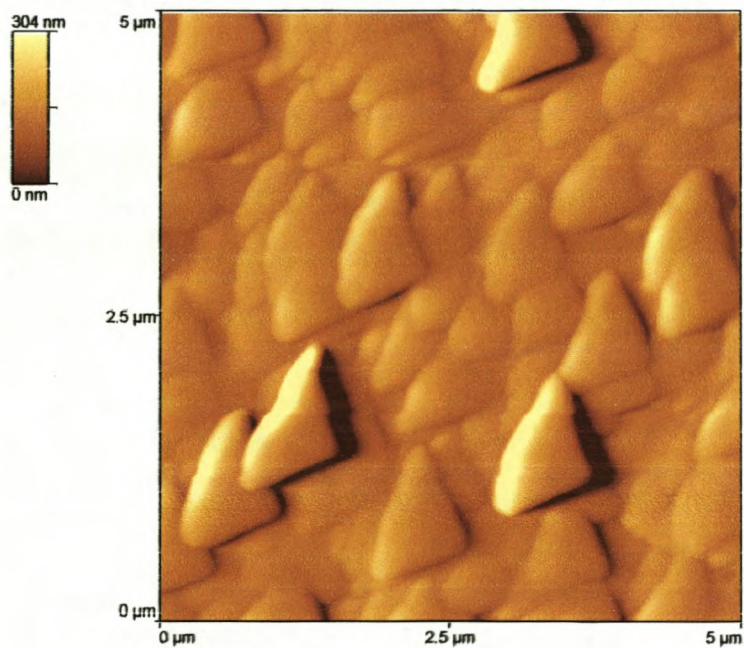


Figure 4.6: AFM of (b) spin coated $\text{MnO}_x/\text{SnO}_2$ films.

4.3.6 *Rutherford backscattering*

The RBS spectra show that the substrate that was used (solid titanium) and the coated metal oxide thin films give well separated peaks for simulation and fitting purposes. This confirms the suitability of RBS as an analytical tool for compositional analysis. Simulation was done using the Rutherford Universal Manipulation Programme (RUMP).

Comparing the spin and dip coated surfaces, it appears that in most cases the elements were more abundant in the spin coated surfaces than in the dip coated surfaces. This is reflected in the larger peak areas obtained by RBS for spin coated versus dip coated samples (Figure 4.7a&b).

It should be noted however that the surfaces were not homogeneous in composition and hence compositional analysis of the thin films as presented in the data is subject to the composition of the specific surface area that was bombarded with α -particles (RBS) and protons (PIXE). Usually an area $5\ \mu\text{m} \times 5\ \mu\text{m}$ near the center of the samples was selected for characterization and taken as representative of the entire sample.

The thickness of films determined by RBS was in the order of 20 to 40 nm for spin coated films and less for dip coated films. The only exception was the Zr spin coated film which had a film thickness of 140 nm.

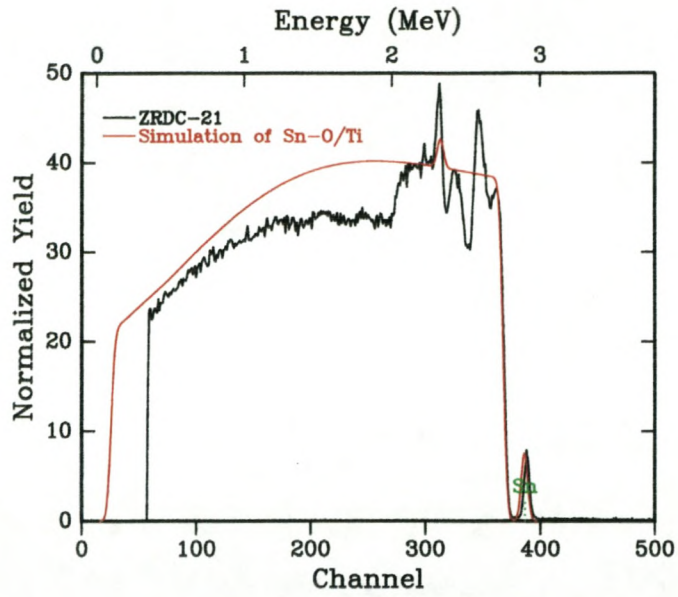


Figure 4.7: (a) RBS of Zr/SnO₂ dip coated surfaces and the fit spectrum by RUMP (red).

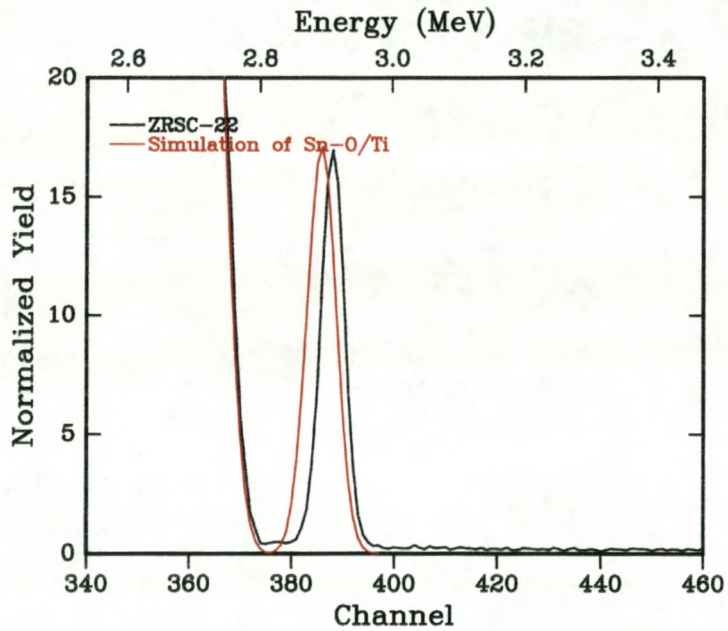


Figure 4.7: (b) RBS of Zr/SnO₂ spin coated surfaces and the fit spectrum by RUMP (red).

4.3.7 *Particle induced X-ray emission*

Three sets of prepared thin films were analysed. In all cases the dopant element was positively identified. The spin coated samples generally gave thicker films than the dip coated samples did. The detection of the dopant element was consequently also more successful for spin coated samples than for dip coated samples. For the third set of samples, detection of the dopant element in the dip coated samples was generally so low that no quantitative evaluation of the dopant element was performed.

Tungsten (W) was identified as a contaminant in all samples, as determined by performing a blank run on an uncoated titanium sample. Further tests with blank samples and standards eliminated the detection chamber as the source of contamination. The W is thought to be present as a contaminant in the titanium. Fe and Ag contaminants were introduced as part of the composition of the starting materials and were therefore unavoidable. None of the contaminants however showed any interference with the catalytic behaviour of the thin film electrodes.

By using intrinsic doping during sol-gel synthesis, a fusion of the dopant atom with the SnO₂ host material is obtained after annealing the thin films. The surface composition of mixed metal oxide thin films (expressed as a %) based on ppm quantification, will therefore not necessarily reflect the calculated composition (Table 4.2). Consistency in the estimations for Pd, Zr, Sb and Cu is observed, at their respective levels of doping.

For detailed structural analysis, tools such as X-ray crystallography could assist in identifying the exact location of the dopant molecules within the SnO₂ host structure. This would involve the growth of good quality crystals which is time consuming and a specialized skill in its own right.

Table 4.2: Typical compositional analysis of mixed metal tin oxide thin films
(% composition based on ppm analysis) as determined by PIXE/RBS

Dopant	Coat	Fe	Cu	Ag	Sn	Sb	W	Mn	Co	Zr	Pd	Zn
Sb	dip	2.79	0.47		60.12	26.94	9.68					
Sb	spin	3.38	1.14		55.12	12.19	28.17					
Mn	dip	2.57	0.94	2.71	72.14	0.00	19.48	0.92	1.24			
Mn	spin	0.33	0.20	0.09	94.02	1.30	3.41	0.38	0.27			
Zr	dip	0.47	0.11	0.10	95.38	0.54	2.49	0.13	0.12	0.65		
Zr	spin	0.13	0.05		97.98	0.07	1.01	0.03	0.04	0.68		
Pd	dip	0.33	0.24	0.04	54.14		4.13	0.08	0.12		0.27	40.65
Pd	spin	0.35	0.21	0.33	94.77		3.12	0.28	0.28		0.67	
Cu	dip	4.72	5.16		41.00	0.43	48.69					
Cu	spin	0.47	9.34	0.66	86.37		3.16					

4.4 Conclusion

From thermogravimetric analysis it emerges that PdO₂/SnO₂ forms the most stable phase ($\pm 90\%$ weight loss and 180°C) whilst all the other mixed metal oxides stabilize at much higher temperatures (around 400°C). ZrO₂/SnO₂ and Sb₂O₅/SnO₂ follow a similar temperature degradation profile with a maximum %weight loss of 60%. CuO/SnO₂ and MnO_x/SnO₂ show 80% weight loss. The mixed metal tin oxides form stable phases in the order PdO₂ > CuO > Sb₂O₅ > ZrO₂ > MnO_x.

From UV/vis measurements it was possible to determine the band gap energies for all mixed metal oxides to be in the range 2.37 to 3.37 eV. The addition of these metal oxide dopants do not decrease the band gap energies of undoped SnO₂. ZrO₂/SnO₂ gels show a lower band gap energy i.e. improved electron conduction, with prolonged ageing since the sample becomes more crystalline. PdO₂/SnO₂ was the only mixed metal oxide that had a lower band gap than undoped SnO₂.

XRD analysis of the transition metal doped samples could only confirm the cassiterite structure of SnO₂; it was not useful in identifying any of the dopant atoms. PIXE/RBS combination was used for determination of chemical composition. An accurate assessment of whether the calculated doping ratio was obtained, needs to be based on raster or grid-like compositional analysis of the entire surface and taking into account the effect of depth profiling. This is possible with the PIXE/RBS combination technique but was not done due to limitations in availability of the nuclear probe facility.

Consistency in the compositional analysis of Pd, Zr, Sb and Cu thin films (% composition based on ppm concentrations) was observed, at their respective level of doping. At best the inclusion of the active centers within the host material was demonstrated.

Chapter five

Electrochemical characterisation by cyclic voltammetry

5.1 Introduction

The synthesised mixed metal oxide gels were prepared as thin film electrodes. An electrochemical cell (three electrodes) was employed for the electrochemical characterisation of the novel surfaces. Cyclic voltammetry (CV) was used for the investigation of redox behaviour and bulk electrolysis was used to determine the overall number of electrons involved in the electrode reaction.

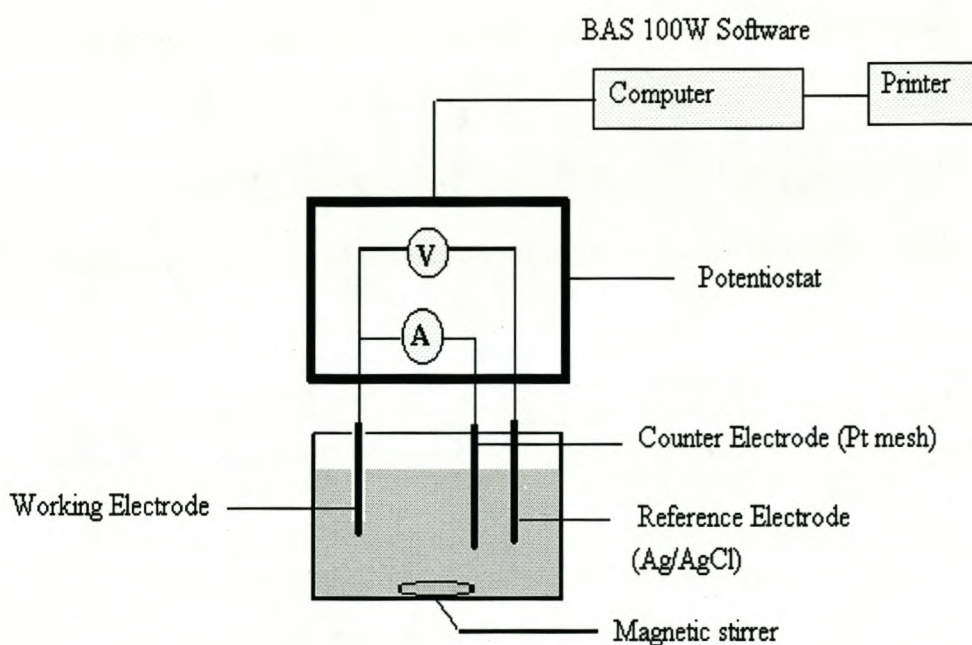
5.2 Experimental conditions

A BAS CV100 cell stand interfaced with a microcomputer (SMM Instruments) was used for all electrochemical experiments. The cell volume was kept at 10 mL for all CV investigations. The values of experimental parameters are given below (Table 5.1).

Table 5.1: Instrumental parameters for cyclic voltammetry experiments

Parameter	Value
Start Potential	0 mV
Initial Potential	2500 mV
End Potential	-500 mV
Scan rate	9 - 400 mV.s ⁻¹
Current range	100 uA
Number of sweeps	3

Data analysis was done using BAS 100W software. The mixed metal tin oxide surfaces were connected as the working electrodes, a standard calomel reference electrode was used and a platinum mesh (Alpha Aesar, 100 mesh, 2 x 2 cm) as counter electrode (Figure 5.1).

**Figure 5.1:** Electrochemical cell arrangement used for CV experiments.

The electrocatalytic properties of these metal oxides were investigated in acid medium. Potential scans were carried out in the positive direction from 0 mV to about +2500 mV first and then in the negative direction to -500 mV. The electrolyte of choice, 0.001 M H₂SO₄, was prepared using Millipore, ultra high quality (UHQ) water. The effect of concentration on the efficiency of the H₂SO₄ as an effective background electrolyte was investigated. For the purpose of preliminary mechanistic investigations, a one electron exchange system (K₃Fe(CN)₆) at concentrations of about 2 mM in 0.001 M H₂SO₄, was used.

5.3 Results and discussion

The electrochemistry of the mixed metal oxide electrodes were evaluated in three different electrolytes (KOH, Na₂HPO₄ and H₂SO₄). The basic (KOH) and neutral (Na₂HPO₄) electrolytes produced very good background voltammograms, i.e. low currents and no interfering peaks, but also very poor current responses for the active species in solution viz. K₃Fe(CN)₆. The sulphuric acid medium proved to be the best electrolyte for investigation of redox behaviour of K₃Fe(CN)₆. However, in the background evaluation, a reduction peak around -200 mV to -400 mV was observed at some of the mixed metal oxide electrodes. A literature reference for cyclic voltammetry at Pt and Pt_xNi_y electrodes in H₂SO₄ electrolyte showed a similar reduction peak at around -200 mv. This peak was attributed to the reduction of adsorbed hydrogen species [65, 66]. The reduction peak observed at around -200 mV at the SnO₂/ZrO₂ electrode, grew in size as the sulphuric acid concentration was increased from 0.001 to 0.5 M (Figure 5.2 a,b,c). This behaviour was also observed at the Sb₂O₅/SnO₂ electrode. To obtain minimum interference from the

adsorbed hydrogen reduction, the concentration of background electrolyte was kept at 0.001 M H_2SO_4 , for further electrochemical investigations.

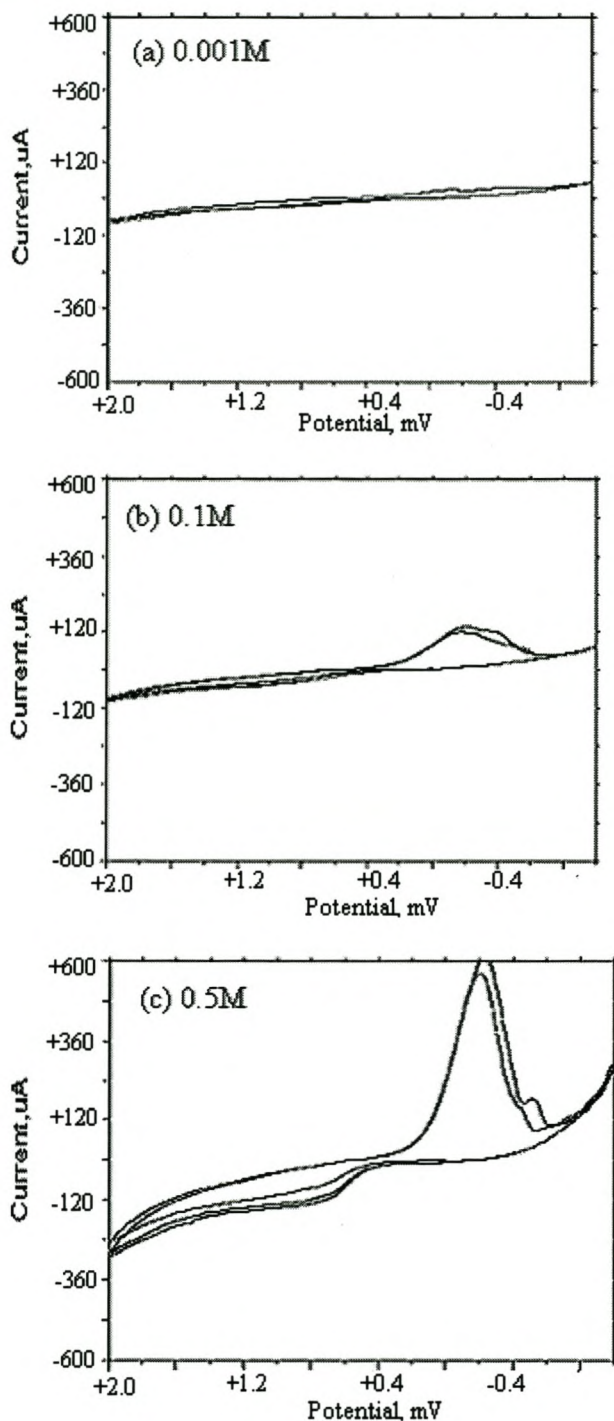


Figure 5.2: Cyclic voltammetry of $\text{ZrO}_2/\text{SnO}_2$ electrodes in H_2SO_4 (0.001 M, 0.1 M and 0.5 M) at 200 mV/s.

5.3.1 Mixed metal tin oxides in 0.001M H₂SO₄

All the mixed metal oxide thin film electrodes were observed to carry very low currents (uA) in the 0.001 M H₂SO₄ electrolyte (Figure 5.3). All the mixed metal tin oxides show an approximately linear residual current in terms of current density as the scan speed is increased.

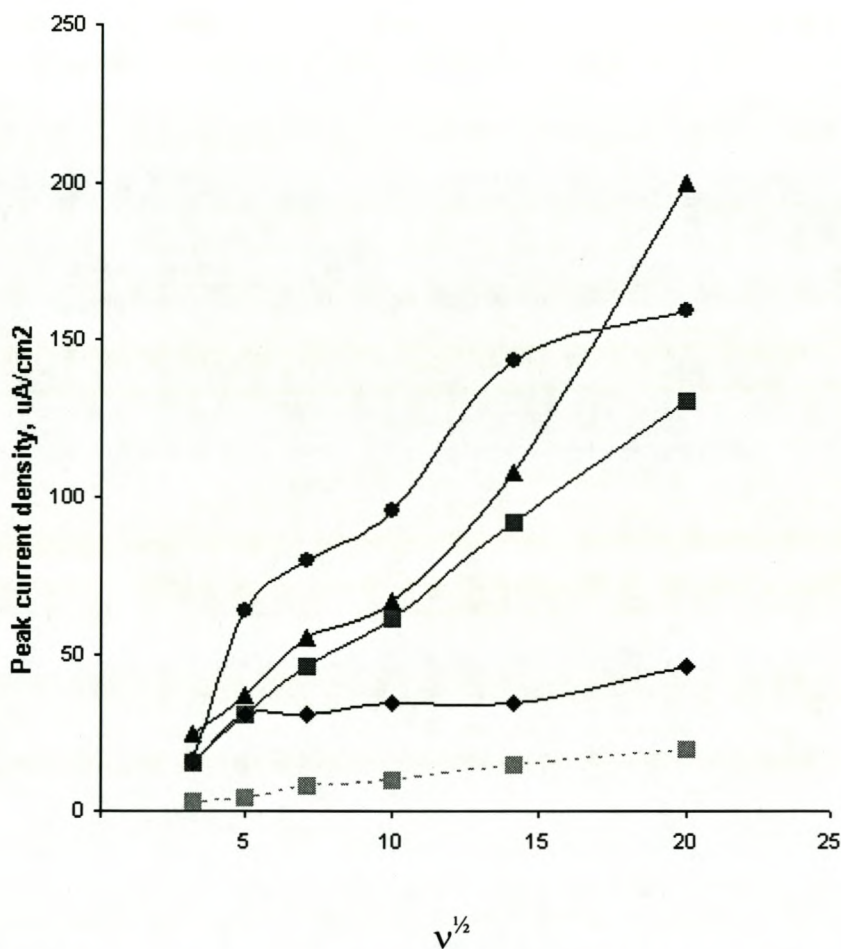


Figure 5.3: Current response as a function of scan rate for mixed metal tin oxide electrodes in 0.001 M H₂SO₄ (—■—Sb₂O₅/SnO₂, —▲— ZrO₂/SnO₂, —◆— CuO/SnO₂, —●—PdO₂/SnO₂, --■-- MnO_x/SnO₂).

Sb_2O_5 , ZrO_2 and PdO_2 doped SnO_2 gave the highest current densities. Sb_2O_5 and ZrO_2 doped tin oxide were observed to give the best qualitative linear response.

Cyclic voltammetry of CuO/SnO_2 and $\text{MnO}_2/\text{SnO}_2$ in the H_2SO_4 background shows that the electrode material undergoes oxidation and reduction (Figures 5.4 and 5.5). This could give rise to dissolution of the metal oxide from the catalyst surface due to acidic reaction conditions [67]. In other words these mixed metal oxides are not stable anodes for the evaluation of redox reactions. The scan rate dependence of Sb_2O_5 and ZrO_2 doped tin oxide in the presence of the classic one electron exchange couple, $\text{K}_3\text{Fe}(\text{CN})_6$, was further evaluated.

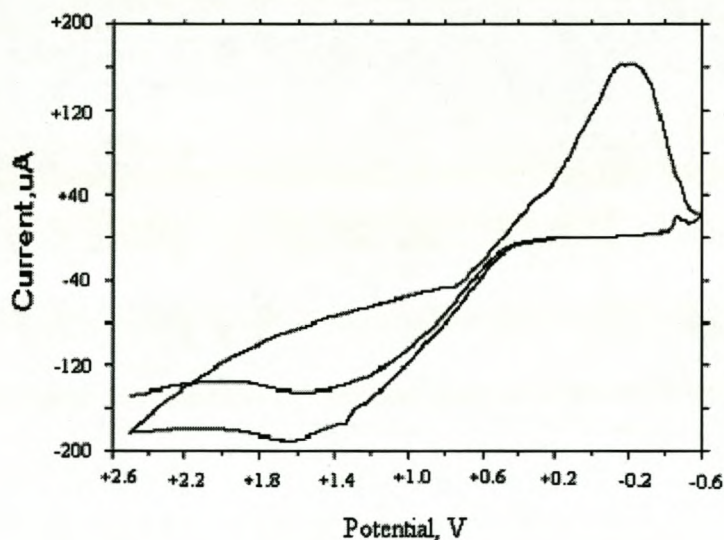


Figure 5.4: Cyclic voltammetry of CuO/SnO_2 electrode in H_2SO_4 .

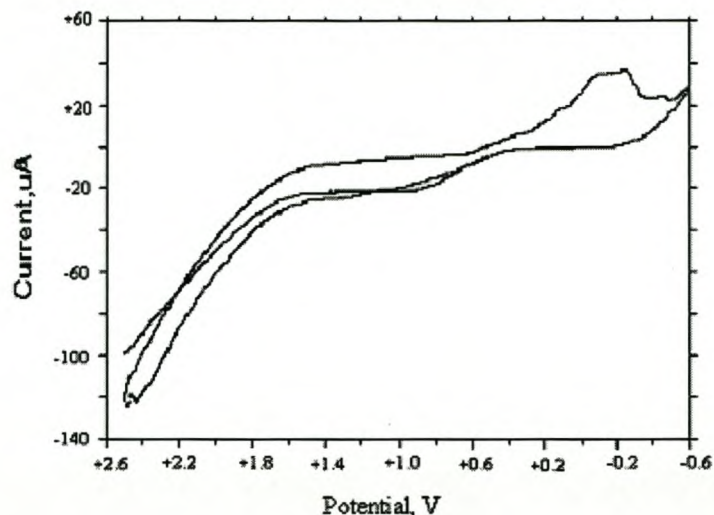


Figure 5.5: Cyclic voltammetry of $\text{MnO}_2/\text{SnO}_2$ electrode in H_2SO_4 at 50 mV/s.

5.3.2 $\text{K}_3\text{Fe}(\text{CN})_6$ oxidation at $\text{Sb}_2\text{O}_5/\text{SnO}_2$ and $\text{ZrO}_2/\text{SnO}_2$ thin film electrodes

The mixed metal tin oxides were examined for their ability to act as electron carriers. A 0.002 M $\text{K}_3\text{Fe}(\text{CN})_6$ solution was prepared in the 0.001 M H_2SO_4 electrolyte. Other than adding this test solution, the electrochemical cell parameters were unchanged. Due to problems of electrode fouling it was difficult to use phenol in investigating charge transfer at the mixed metal tin oxide electrodes in cyclic voltammetry experiments

The anodic peak density (Figure 5.6) was recorded as a function of the scan rate. The dotted lines represent the oxidation peak current densities for the oxidation of $\text{K}_3\text{Fe}(\text{CN})_6$ as a function of scan rate and the solid lines represent the backgrounds for the respective systems. Use of the 0.001 M H_2SO_4 electrolyte provides good separation between analyte signal and baseline. The presence of an electron carrier highlights the change in charge transport rates as a function of scan rate.

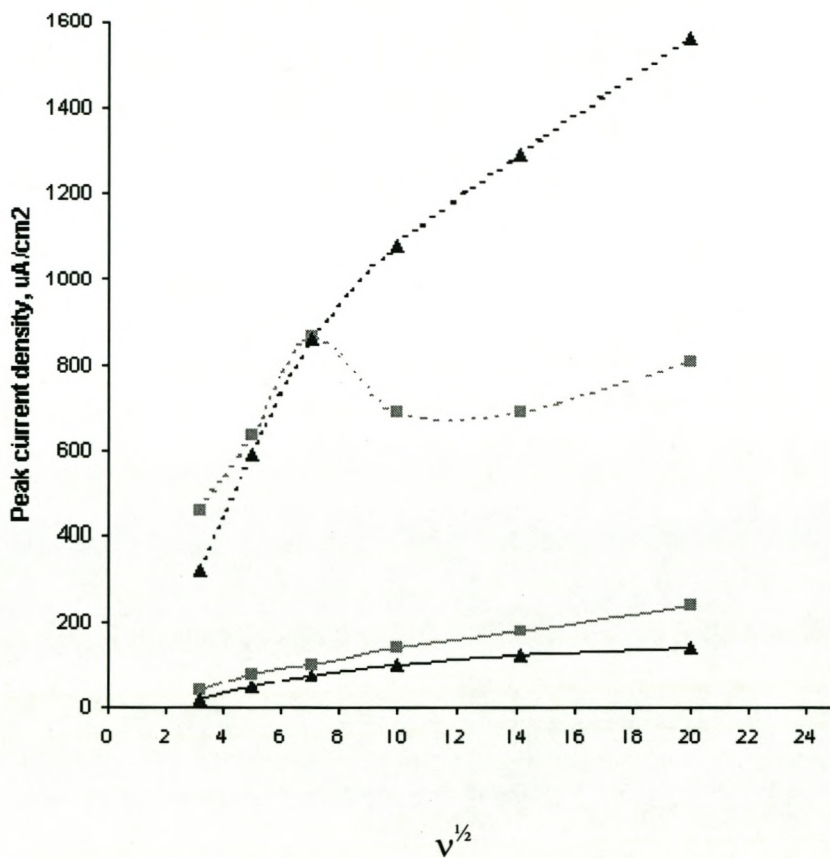


Figure 5.6: ZrO_2/SnO_2 current response as a function of scan rate in 0.002 M $K_3Fe(CN)_6$ (—■— Zr1 in H_2SO_4 , —▲— Zr2 in H_2SO_4 , --■-- Zr1 with $K_3Fe(CN)_6$, --▲-- Zr2 with $K_3Fe(CN)_6$).

At low scan rates (below 50 mV/s) the CV of the oxidation reduction at ZrO_2/SnO_2 appears quasi-reversible (Figure 5.7).

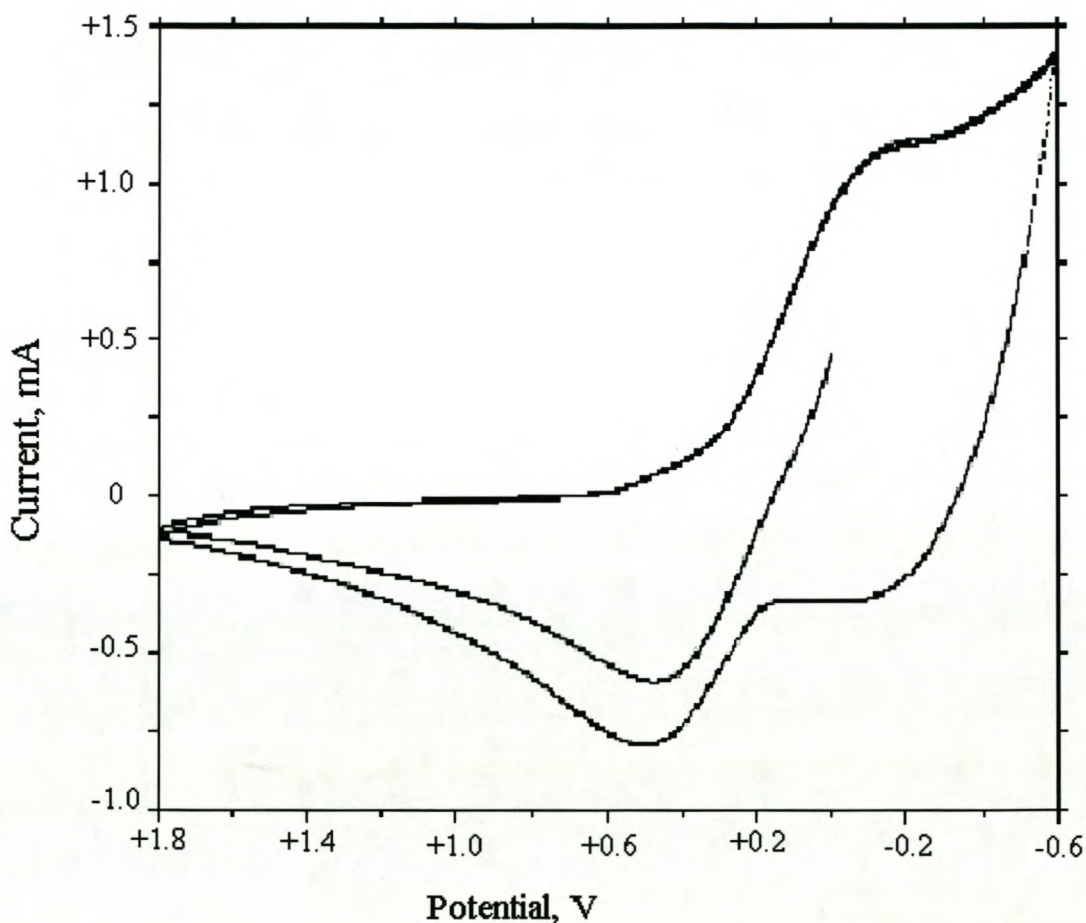


Figure 5.7: Cyclic voltammetry of $\text{K}_3\text{Fe}(\text{CN})_6$ oxidation at a $\text{ZrO}_2/\text{SnO}_2$ thin film at scan rate 50 mV/s.

The separation between the oxidation and reduction peaks ($\Delta E_p = 446$ mV) is much larger than peak separation expected for a reversible one electron transfer i.e. 59 mV. This suggests an irreversible electron transfer at the $\text{ZrO}_2/\text{SnO}_2$ thin film electrode. The half wave potential of the $\text{K}_3\text{Fe}(\text{CN})_6$ system is 177 mV. The same reaction at the $\text{ZrO}_2/\text{SnO}_2$ thin film electrode at 9 mV/s, improves the peak separation to about 200 mV. The increase in ΔE_p with increasing scan rate is characteristic of quasi-reversible reaction mechanisms.

The current density is notably lower (10x) for the antimony doped tin oxide films compared to the zirconium doped films for the same one electron transfer. The analyte current and background current densities are not well separated (Figure 5.8).

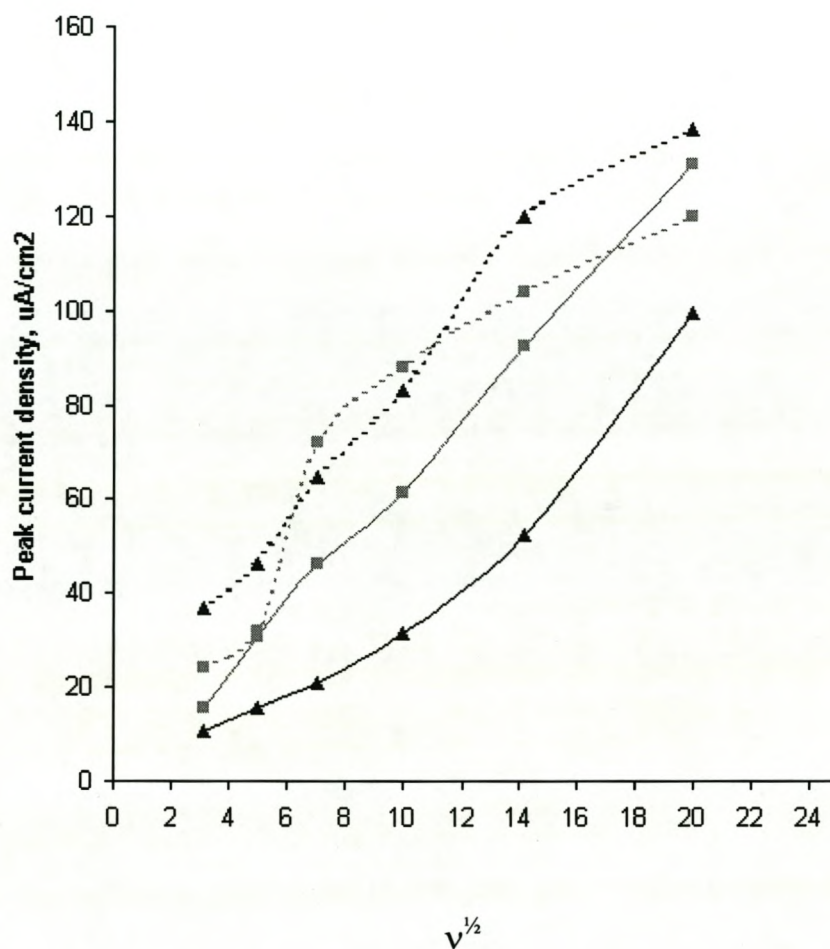


Figure 5.8: Sb_2O_5/SnO_2 current response as a function of scan rate in 0.002 M $K_3Fe(CN)_6$ (—■— Sb1 in H_2SO_4 , —▲— Sb2 in H_2SO_4 , --■-- Sb1 with $K_3Fe(CN)_6$, --▲-- Sb2 with $K_3Fe(CN)_6$).

Cyclic voltammetry of $\text{Sb}_2\text{O}_5/\text{SnO}_2$ shows that well defined oxidation and reduction peaks are only observed at scan rates lower than 25 mV/s (Figure 5.9). This observation together with the almost ten fold drop in current density for the same experimental conditions, suggests that the zirconium doped system has improved catalytic ability compared to that of antimony doped tin oxide.

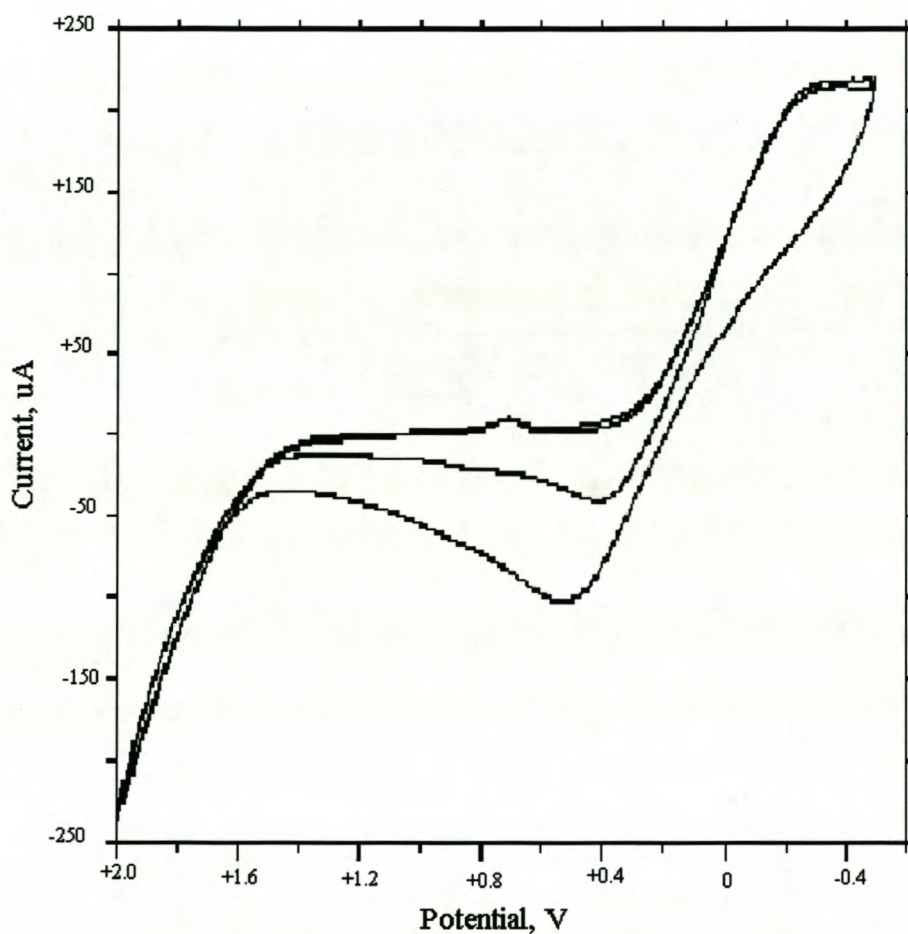


Figure 5.9: Cyclic voltammetry of $\text{K}_3\text{Fe}(\text{CN})_6$ at the $\text{Sb}_2\text{O}_5/\text{SnO}_2$ thin film electrode at scan rate 25 mV/s.

The separation between the oxidation and reduction peak for antimony doped tin oxide, ($\Delta E_p = 692 \text{ mV}$) is marginally larger than for the zirconium system and confirms the irreversible nature of the mixed metal tin oxides. Inspection of the half wave potential for $\text{K}_3\text{Fe}(\text{CN})_6$ of the antimony doped thin film, $E_{1/2} = 146 \text{ mV}$, confirms that the energy requirements for electron transfer between this system and the Zr doped tin oxide system, is comparable.

5.3.3 *$\text{K}_3\text{Fe}(\text{CN})_6$ oxidation at CuO/SnO_2 , MnOx/SnO_2 and $\text{PdO}_2/\text{SnO}_2$ thin film electrodes*

No additional peaks that could be associated with the oxidation of $\text{K}_3\text{Fe}(\text{CN})_6$ at the CuO/SnO_2 and $\text{MnO}_2/\text{SnO}_2$ thin film surfaces were identified by means of CV (Figure 5.10 a and b). The peaks associated with the activity of the electrode material in the background electrolyte (cf Figure 5.5) showed a decrease in current density, when examining the oxidation of $\text{K}_3\text{Fe}(\text{CN})_6$ at 50 mV/s (Figure 5.10). CV of the $\text{PdO}_2/\text{SnO}_2$ thin film electrode in background electrolyte, showed no oxidation or reduction peaks. The oxidation of 0.002 M $\text{K}_3\text{Fe}(\text{CN})_6$ at the $\text{PdO}_2/\text{SnO}_2$ thin film electrode in the same background electrolyte, produced no clearly defined peaks at scan rates between 25 to 400 mV/s .

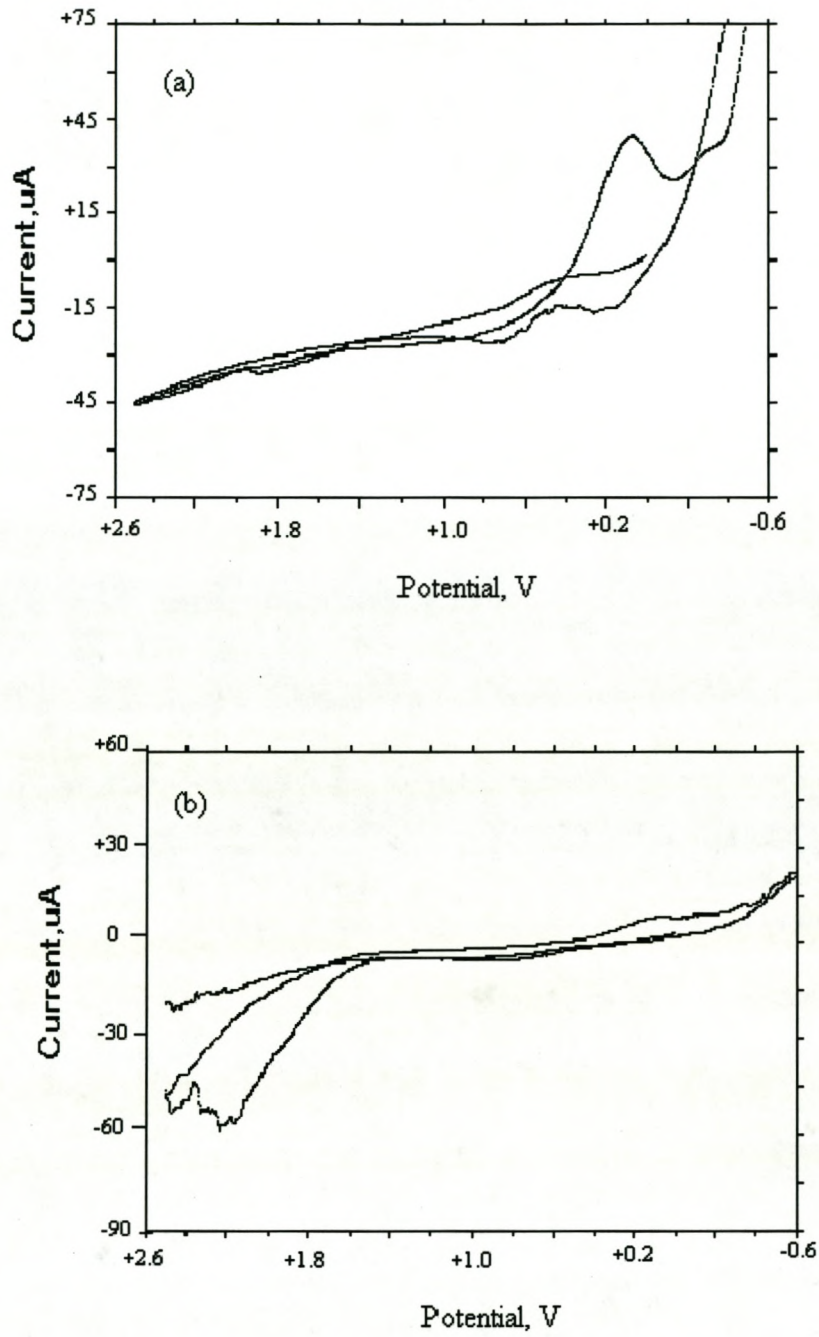


Figure 5.10: Cyclic voltammetry of 0.002 M $K_3Fe(CN)_6$ oxidation at (a) CuO/SnO_2 and (b) MnO_2/SnO_2 thin film electrodes, at 50 mV/s.

Comparing the half wave potentials for the oxidation and reduction of $\text{K}_3\text{Fe}(\text{CN})_6$ at antimony and zirconium doped tin oxides ($E_{1/2} = 146 \text{ mV}$ and 177 mV) to the same reaction at a glassy carbon electrode, indicates that the oxidation takes place at comparable potentials. The oxidation and reduction of $\text{K}_3\text{Fe}(\text{CN})_6$ on the glassy carbon electrode at scan rate 400 mV/s , is presented to show the kinetics of this redox couple at a reference surface, for comparison to the work presented here (Figure 5.11).

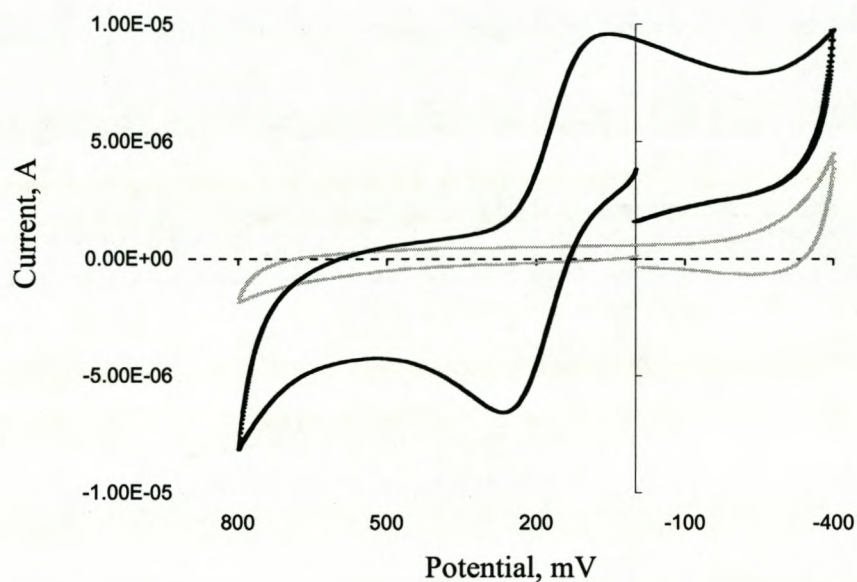


Figure 5.11: Oxidation of $\text{K}_3\text{Fe}(\text{CN})_6$ (black) at glassy carbon electrode in 0.001 M H_2SO_4 (gray) at 400 mV/s .

5.3.4 Tafel plots

For reactions where the current is controlled by the rate of electron transfer the exchange current for common redox couples can be obtained by the Butler-Volmer equation. At large negative overpotentials ($i_c \gg i_a$) the equation becomes (Equation 5.1):

$$i = i_0 \exp(-anF\eta/RT) \quad (5.1)$$

with $\eta = E - E_{eq}$, the overvoltage.

By plotting $\log I$ vs η one obtains the Tafel plots for the cathodic (I_c) and anodic (I_a) branches of the current voltage curve (Figures 5.12 and 5.13) [55].

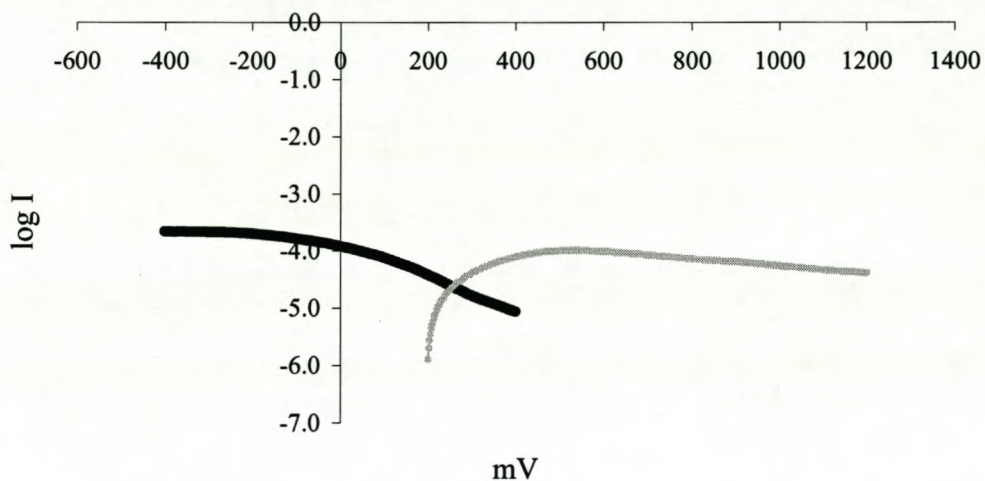


Figure 5.12: Tafel plot for Sb_2O_5/SnO_2 with $K_3Fe(CN)_6$ at 25 mV/s (— = I_c , — = I_a).

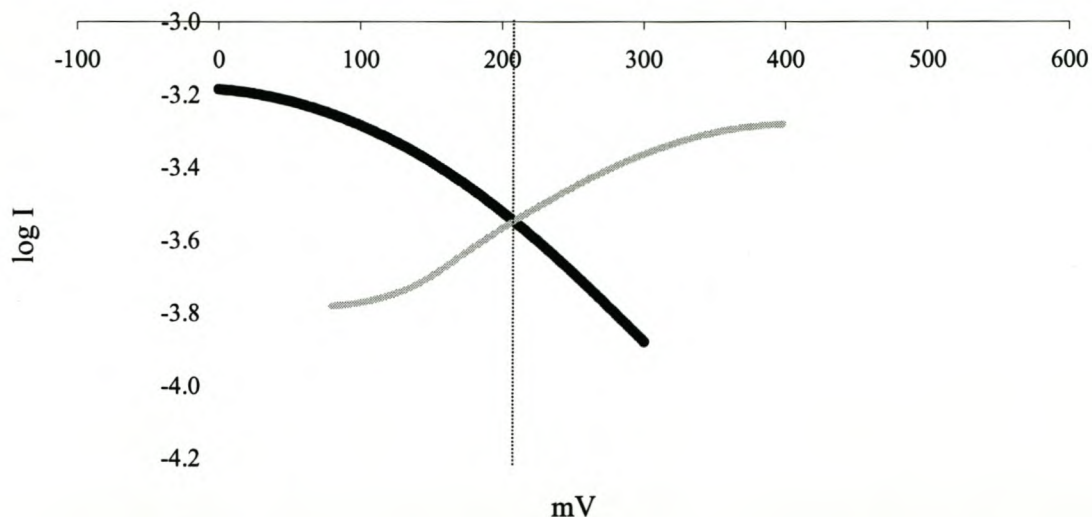


Figure 5.13: Tafel plot for $\text{ZrO}_2/\text{SnO}_2$ with $\text{K}_3\text{Fe}(\text{CN})_6$ at 25 mV/s, (— = I_c , — = I_a).

From the slope of the anodic and cathodic branches the alpha values were calculated as $\alpha_a = 0.26$ and $\alpha_c = 0.18$ for antimony doped tin oxide. α is known as the transfer coefficient for the anodic and cathodic reactions. It is an indication of the amount of energy required by a system to overcome the activation energy barrier of a given reaction. For simple electron transfer reactions it has values of about 0.5 respectively. The oxidation and reduction of $\text{K}_3\text{Fe}(\text{CN})_6$ does not appear to proceed via a simple electron transfer reaction. The same effect is observed for the $\text{ZrO}_2/\text{SnO}_2$ electrodes. The transfer coefficients were calculated to be $\alpha_a = 0.12$ and $\alpha_c = 0.15$ for zirconium doped tin oxide. These low values are acceptable in the light of the slow and irreversible nature of electron transfer as observed from the scan rate dependence of this reaction at zirconium and antimony doped tin oxide.

5.4 Conclusions

The reduction peak observed at \pm -200 mV for the SnO₂/ZrO₂ and Sb₂O₅/SnO₂ electrodes in sulphuric acid was identified to be as a result of the reduction of protons. The peak current increased consistently with increased H₂SO₄ concentration in the range 0.001 to 0.5 M. The electrochemical activity of CuO/SnO₂ and MnO_x/SnO₂ electrodes in H₂SO₄ showed that these mixed metal oxides were not stable anodes for the evaluation of redox reactions.

The nature of the electron transfer for K₃Fe(CN)₆ at ZrO₂/SnO₂ and Sb₂O₅/SnO₂ thin film electrodes, are irreversible, since the separation between the oxidation and reduction peaks ($\Delta E_p = 446$ mV) were much larger than 59 mV. The half wave potential for the oxidation of K₃Fe(CN)₆ at ZrO₂/SnO₂ ($E_{1/2} = 177$ mV) and Sb₂O₅/SnO₂ electrodes ($E_{1/2} = 146$ mV) are approximately the same as the half wave potential for the same reaction at the glassy carbon electrode. This shows that the oxidation at the metal oxide electrodes is more efficient in terms of its energy requirements. Even though ZrO₂/SnO₂ and Sb₂O₅/SnO₂ electrodes have comparable interfacial energy characteristics, the current densities recorded for the oxidation of K₃Fe(CN)₆, imply that ZrO₂/SnO₂ electrodes have some advantage over Sb₂O₅/SnO₂ electrodes, in terms of charge transfer efficiency.

The low values of the transfer coefficients determined for the oxidation of K₃Fe(CN)₆ at ZrO₂/SnO₂ and Sb₂O₅/SnO₂ electrodes confirm that electron transfer at these electrodes does not occur in a single reversible step. What is indicated as irreversible behaviour by

the CV diagnostic tests used, could in fact be coupled electron transfer mechanisms, i.e. chemical reaction followed by adsorption and electrochemical reactions.

A completely irreversible electron transfer is characterised most strongly by the absence of a reduction peak, which is not what is observed for the antimony and zirconium doped tin oxide electrodes. It is possible to evaluate coupled homogeneous reactions using CV by evaluating the decreasing peak current density of the reduction peak as a function of scan rate. Since the oxidation and reduction peaks at $\text{ZrO}_2/\text{SnO}_2$ and $\text{Sb}_2\text{O}_5/\text{SnO}_2$ electrodes were only observed at low scan rate, a scan rate dependence over a suitably large range of sweep rates, could not be evaluated.

Chapter six

Electrochemical impedance spectroscopy

(EIS) of mixed metal oxides

6.1 Introduction

EIS was used to determine the bulk electrical parameters of the mixed metal tin oxide electrodes as well as the electrical parameters associated with the interface of these electrodes in 0.001 M H₂SO₄. Analysis of data was done by fitting data to suitable, equivalent electrical circuits. The effective media theories (EMT) and the Bricklayer model (BLM) approach of data fitting work well for single crystal samples and were not explored for the complex mixed metal oxide systems, since a detailed understanding of the underlying microstructure of metal oxides would be required [68, 69].

6.2 Common electrical circuits and circuit parameters

The most commonly used model for a simple electron transfer reaction includes an uncompensated solution resistance (R_s) in series with a double layer capacitance (C_{dl}), a charge transfer resistance (R_{ct}) and a frequency dependent resistance called the Warburg impedance (Z_w). The relative size between R_{ct} and Z_w at any given frequency is a measure of the balance between kinetic and diffusion control.

This simplified equivalent electrical circuit is called the Randles equivalent circuit (Figure 6.1) and has two limiting cases i.e. at high and at low frequencies.

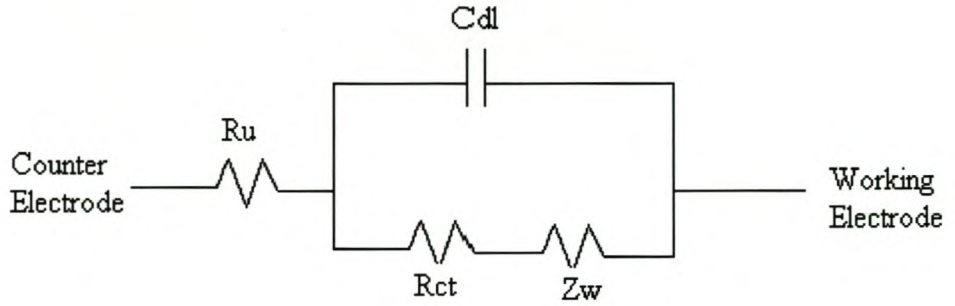


Figure 6.1: Randles equivalent circuit.

At high frequencies, measurements are fast on the time scale of the experiment and the Warburg impedance (diffusion effect, Z_w) is small compared to the charge transfer, hence the impedance expression is simplified to Equation 6.1:

$$(Z' - R_u - R_{ct}/2)^2 + (Z'')^2 = (R_{ct}/2)^2 \quad (6.1)$$

This is the equation of a circle, centred around $Z' = R_u + R_{ct}/2$ with a radius of $R_{ct}/2$.

Low frequency measurements take a long time and the diffusion effects dominate.

The angular frequency, $\omega \rightarrow 0$ and the impedance expression reduces:

$$Z'' = Z' - R_u - R_{ct} + 2\sigma^2 C_{dl} \quad (6.2)$$

Equation 6.2 is the expression of a straight line of unit slope and with an intercept on the real Z' axis given by Equation 6.3 [70].

$$R_u + R_{ct} - 2\sigma^2 C_{dl}. \quad (6.3)$$

σ , is the Warburg constant

Realistic systems can include only one of these extreme cases (high or low frequency) or both. For mixed metal oxide systems it is common to find a combination of semicircles without observing any linear diffusion component.

Electrochemical impedance spectroscopy is often analysed by fitting it to an equivalent electrical circuit using common electrical elements such as resistors, capacitors and inductances (Table 6.1).

Table 6.1: Common electrical elements used in circuit fitting

Component	Current vs Voltage	Impedance
Resistor	$E = IR$	$Z = R$
Inductor	$E = L di/dt$	$Z = j\omega L$
Capacitor	$I = C dE/dt$	$Z = 1/j\omega C$

The impedance of a resistor is independent of frequency and has only a real component. The impedance of an inductor increases as frequency increases. Inductors have only an imaginary impedance component and its current is phase shifted 90 degrees with respect to the voltage. The impedance of a capacitor decreases as the frequency is increased. Capacitors also have only an imaginary impedance component and the current through a capacitor is phase shifted 90 degrees with respect to the voltage [71,79].

6.3 Experimental

EIS measurements were performed in the wide frequency range from 500 kHz to 300 mHz, with an *ac* voltage amplitude of 5 mV. The response of a sample is measured over a wide frequency range and then analysed in the complex plane. A lock in amplifier (SOLARTRON 1260) was used as the signal generator and a potentiostat/galvanostat (SOLARTRON 1286) for electrochemical control. These were interfaced with a computer for data recording and manipulation, using ZPLOT software (version 2.b).

The coating flat cell used in the impedance measurements was designed with a false bottom into which a hole (diameter = 5 mm) was machined. The size of this hole determines the surface area of the working electrode that is exposed to the electrolyte solution during experiments. A snug fitting O-ring provides efficient insulation from the electrical contacts when the wing nuts are tightened during preparation of the electrochemical cell. The coating flat cell design was based on the SOLARTRON product (Figure 6.2).

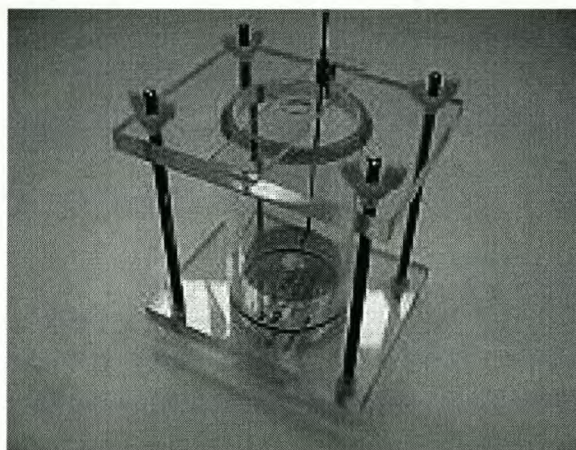


Figure 6.2: Diagram of coating flat cell used for impedance measurements.

The electrochemical cell was made up of three electrodes. The reference electrode was a Ag/AgCl electrode. A platinum mesh counter electrode of sufficiently large surface area was prepared from platinum mesh (Alpha Aesar, 100 mesh, 2 x 2 cm), for efficient current collection. The mixed metal oxide thin film electrodes were mounted as working electrodes. The electrolyte was 0.001 M H₂SO₄ and a volume of approximately 100 mL was sufficient to immerse all electrodes. The solution was de-aerated with online nitrogen gas for at least 600 s and was not stirred during the recording of data. The experimental temperature was controlled to 25±2°C by using a heating mantle, insulating material and a thermometer.

All solutions were prepared using Merck Suprapure acids and Millipore, ultra high quality (UHQ) water. The metal oxide thin film/H₂SO₄ electrolyte interface parameters were evaluated for all metal oxide combinations prepared. Frequency sweep experiments were performed over the entire frequency range and the applied *dc* potential was varied at 100 mV intervals starting from 0mV to 1500 mV. The potential range selected, provides a potential window for oxidation reactions, with the maximum set to include the oxidation potential of phenol at Ti/SnO₂/Sb₂O₅ as determined by Grimm et al., using cyclic voltammetry. At least two different sets of mixed metal oxide electrodes were prepared and analysed by EIS and good agreement was observed between sets. The experiment with each individual electrode was repeated twice to ensure the reproducibility of the data recorded under very rudimentary temperature control conditions.

6.4 Results and discussion

The interface between the electrode surface and 0.001 M H_2SO_4 was investigated over the potential range 0 to 1.5 V. The surface area of electrode exposed in all impedance experiments was determined by the size of the hole in the base of the coating flat cell, i.e. 5 mm diameter (surface area = 0.196 cm^2). The impedance experiments will characterise the electrode/solution interface (Figure 6.3) [80].

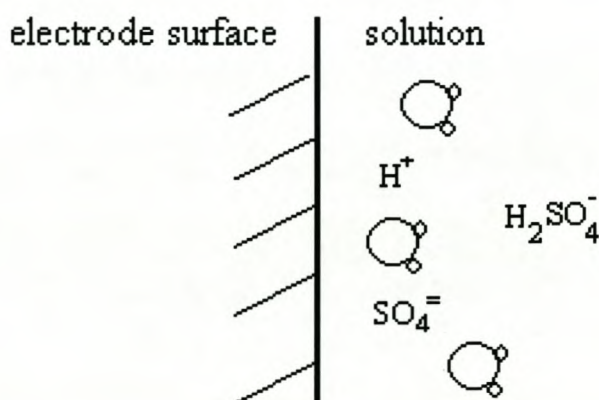


Figure 6.3: Mixed metal oxide electrode interface in solution of interest.

6.4.1 Uncoated titanium substrate in 0.001 M H_2SO_4

Uncoated Ti samples were prepared for measurement in the same way as the mixed metal stannate electrodes. Analyses were performed in a systematic way, starting with the uncoated Ti in 0.001 M H_2SO_4 , then the Ti/ SnO_2 in the same electrolyte, followed by the various mixed metal oxide thin films prepared, in the same electrolyte.

The complex plane plot appears to be the classic Randles circuit equivalent (Figure 6.4). There is a deviation from the Randles behaviour at very high frequencies (above 10^5 Hz). The characteristic 45° slope for Warburg diffusion is observed at frequencies between 10^3 to 10^5 Hz on the Bode plot.

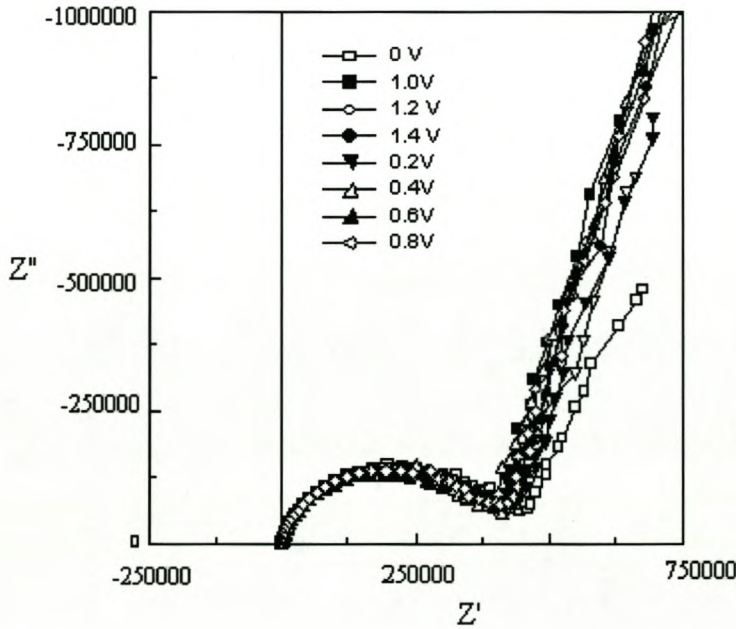


Figure 6.4: (a) Complex plot: uncoated titanium over full frequency spectrum.

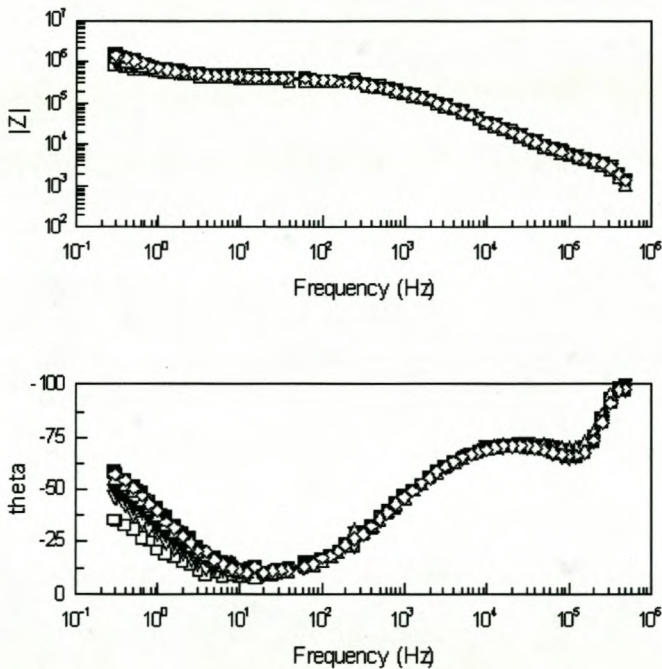


Figure 6.4: (b) Bode plot: uncoated titanium over full frequency spectrum.

The complex plot of the expanded high frequency region of the above plot shows some unusual behaviour. The plot shows no intersection at $Z'' = 0$, but is suspended at $Z'' = 1250$ (Figure 6.5).

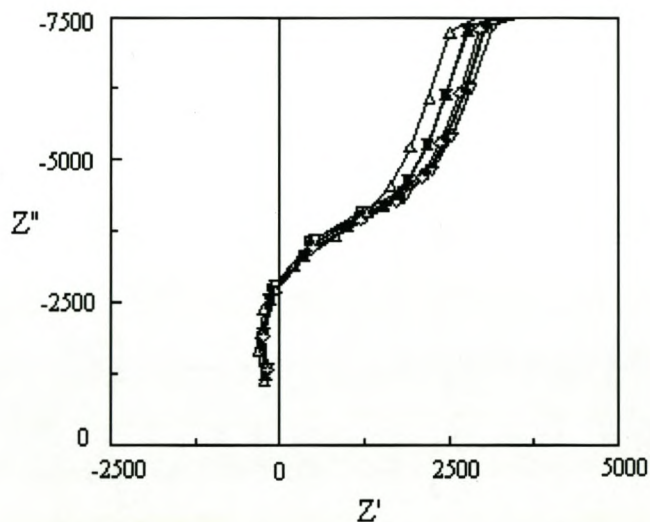


Figure 6.5: Complex plane of uncoated Ti, high frequency region expanded.

The best fit for the high frequency semicircle was obtained using an automatic circle fit and the results are presented in Table 6.2. The depression angle gives an idea of the deviation from a perfect semicircle in degrees, measured as an angle between the x-axis and a line drawn between the low intercept and the center of the semicircle.

Table 6.2: Results of automatic circle fit for uncoated Ti at high frequencies

DC potential, mV	R_1, Ω (low intercept)	R_2, Ω (high intercept)	Capacitance, Farads	Depression angle, $\theta, ^\circ$
0	443	4420	2.37e-10	-42
200	336	4400	2.76e-10	-39.4
400	251	4409	3.1e-10	-37.7
600	310	4453	2.76e-10	-38.24
800	352	4502	2.76e-10	-38.6
1000	383	4455	2.55e-10	-39.7
1200	404	4451	2.55e-10	-40.5
1400	406	4439	2.55e-10	-40
1500	401	4432	2.55e-10	-40

Reasons for the elevation of the high frequency loop from zero on the imaginary axis are not clear and the influence of instrumental parameters cannot be excluded. Depression of the arc indicates a distribution in relaxation time constants rather than a single value, due to inhomogeneities in the electrode material and therefore the rate and extent to which the electrolyte is in contact with the catalyst. The angle, θ , by which the semicircle is depressed below the real axis is related to the width of the relaxation time constant distribution [81]. In the ZPLOT software the depression angle is accounted for by the parameter CPE-P.

Excluding the extreme high frequency range of data, the remaining data obeys a Randles circuit, with constant phase elements (CPE) replacing the capacitance and Warburg components (Figure 6.6).

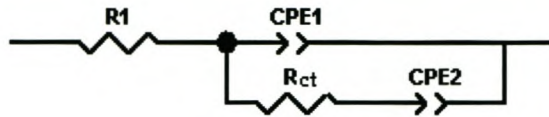


Figure 6.6: Equivalent electrical circuit for uncoated titanium.

The CPE, the constant phase element, is defined by two values (Equation 6.4) viz. CPE-T and CPE-P.

$$Z = 1 / [T(I*w)^P] \quad (6.4)$$

CPE-T is the capacitance associated with the constant phase element. CPE-P is related to the capacitive or resistive nature of the constant phase element. If CPE-P equals 1 then the equation is identical to that of a capacitor. A capacitor is actually a constant phase element, with a constant phase angle of 90 degrees. If CPE-P equals 0.5, a 45 degree line is produced on the Complex-Plane graph. Often a CPE is used in a model instead of a capacitor to compensate for non-homogeneity in the system. For example, a rough or porous surface can cause a double-layer capacitance to appear as a constant phase element with a CPE-P value between 0.9 and 1 [82]. Results of data fitted to the circuit in Figure 6.6 are given in Table 6.3.

Table 6.3: Results of circuit fitting for uncoated titanium

Potential, mV	R_s, Ω	CPE1-T, Farads	CPE1-P	R_{ct}, Ω	CPE2-T, Farads	CPE2-P
0	444.1	3.79e-9	0.8	438140	1.20e-6	0.678
200	203.9	3.76e-9	0.8	418540	7.3e-7	0.74
400	109.9	3.6e-9	0.8	388540	5.5e-7	0.79
600	221	4.06e-9	0.8	398540	5.2e-7	0.797
800	317	3.78e-9	0.8	398540	4.93e-7	0.801
1000	373	3.77e-9	0.8	398540	4.7e-7	0.802
1200	396.7	3.74e-9	0.8	398540	4.6e-7	0.798
1400	420.7	3.68e-9	0.8	398540	4.6e-7	0.785

The deviation of CPE-P from unity is an indication of a distribution of capacitances at the electrode surface. The CPE behaviour arises because microscopic material and adsorption properties are distributed, but impedance measures only the average of resistance or capacitance over the exposed area.

The capacitance of the interface shows a decreasing trend as the potential is increased between 0 to 1.4 V (Figure 6.7). This can be interpreted as a decrease in the thickness of the double layer as the potential is increased. The double layer exists as a result of the alignment of charged ions (positive and negative) in solution at the electrode surface. As the potential at the electrode surface is increased, the negative ions in solution are attracted more strongly and the charge separation between the electrode surface and negative ions in solution is decreased. This is measured as a decrease in capacitance, with increasing potential.

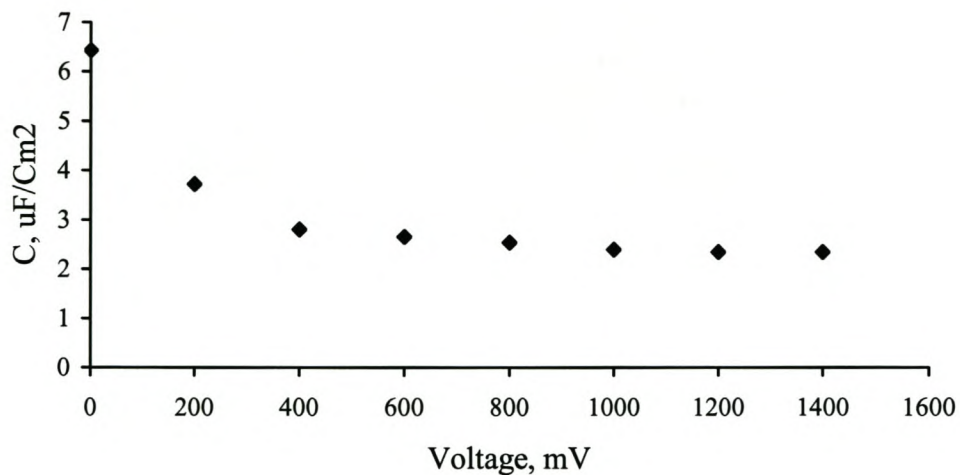
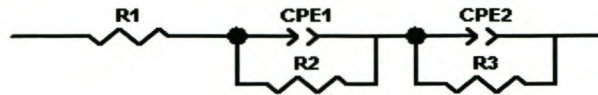


Figure 6.7: Capacitance vs voltage plot for uncoated Ti interface.

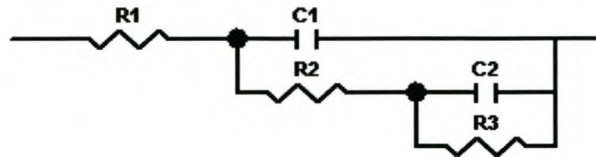
6.4.2 *Titanium substrate coated with SnO₂, in 0.001 M H₂SO₄*

The SnO₂ gel was prepared by the sol-gel route without the addition of any dopant elements and was coated onto the titanium substrate to provide an undoped tin oxide electrode. This was mounted in the coating flat cell as the working electrode for evaluation of its characteristics in the background electrolyte.

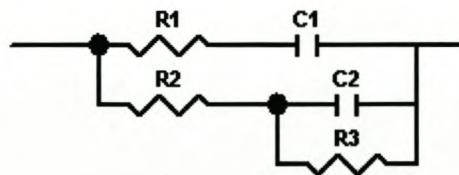
A system displaying two capacitive loops may be characterised by any of three possible circuits (Figure 6.8). These circuits are used to describe two inter related limiting electrode processes processes [79].



(a) Voigt model



(b) Ladder model



(c) Mixed model

Figure 6.8: Three different equivalent circuits for systems with two rate limiting electrode processes (a) Voigt model (b) Ladder model and (c) Mixed model.

The same impedance spectrum for all these circuits can be obtained for a particular data set, depending on a proper choice of parameters.

The complex plane plot of Ti/SnO₂ yielded a full semicircle at high frequency and an incomplete semicircle at lower frequency. The low frequency impedance behaviour changes from linear to an incomplete semicircle improves as the applied potential is increased. A combination of two series resistor- capacitance circuit was used for data fitting (Figure 6.8a). Evidence from literature supports this choice of equivalent circuit. EIS was used to study the effect of temperature and number of coatings on

densification and crystallization of sol-gel prepared SnO_2 films and the EIS data fitting was based on the circuit in Figure 6.8a [82, 83].

This equivalent electrical circuit (eec) was used throughout for the fitting of mixed metal oxide data. In all cases a good fit was obtained for the two series resistor-capacitance combination circuit. The use of distributed elements in place of pure capacitance emerged as a common practice in the evaluation of electrical parameters of mixed metal oxide bulk material and solution interfaces.

The complex plane plot of the Ti/SnO_2 electrode/solution interface shows one full semicircle (high frequency) and a half semicircle at low frequency (Figure 6.9). The high frequency semicircle gives the characteristics of the bulk material. The half semicircle at lower frequency on the complex plot depicts charge transfer at the electrode interface and changes from linear (no charge transfer) to an incomplete semicircle (conductivity at the interface).

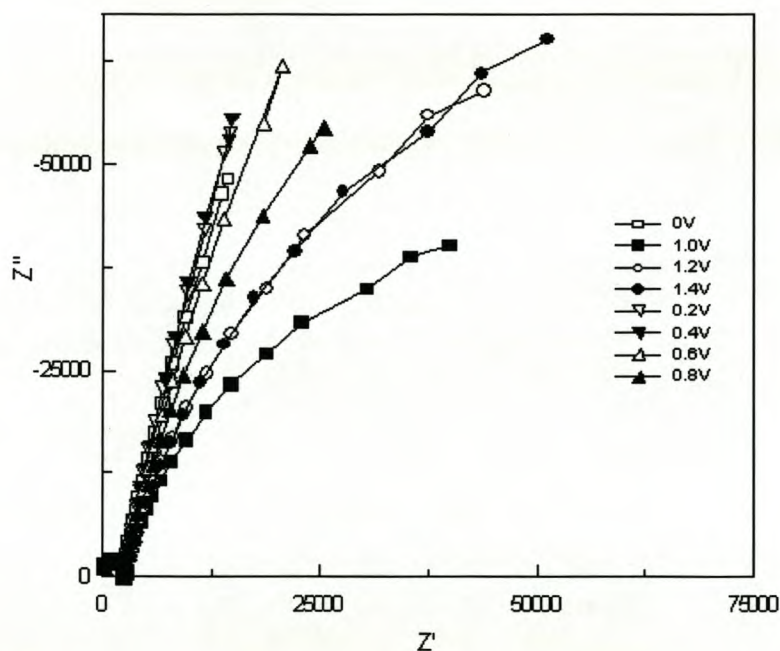


Figure 6.9: (a) Complex plot of Ti/SnO_2 .

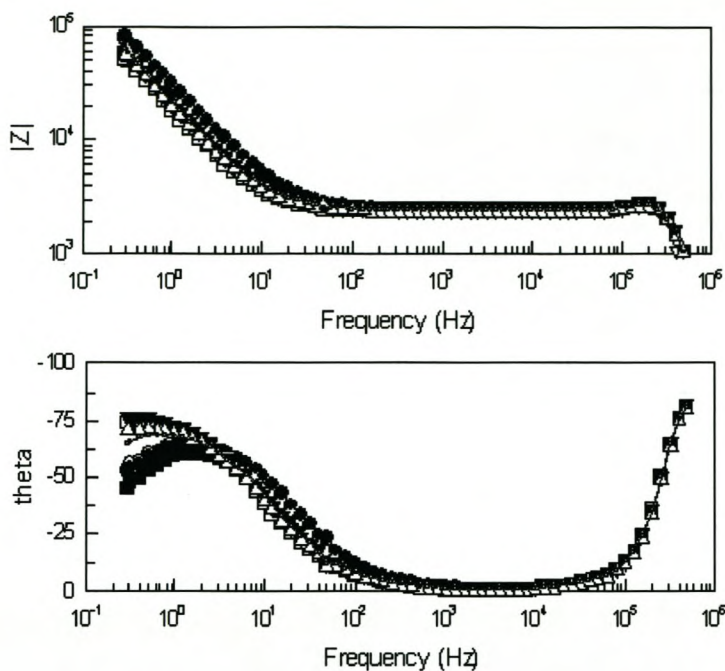


Figure 6.9: (b) Bode plot of Ti/SnO₂.

The bode plots show a strong indication of Warburg impedance in the low frequency region and a good fit for $-R_{ct}-W-$ is expected. The Warburg effect can be confirmed by plotting the real and imaginary parts of Z vs. $1/w^{1/2}$. The lines should be straight and parallel (Figure 6.10). The slope of both lines should be equal to σ , the Warburg constant. The line of the imaginary component (Z'') should intersect the Z axis at zero, while the intercept for the real component (Z') is R_{ct} [84].

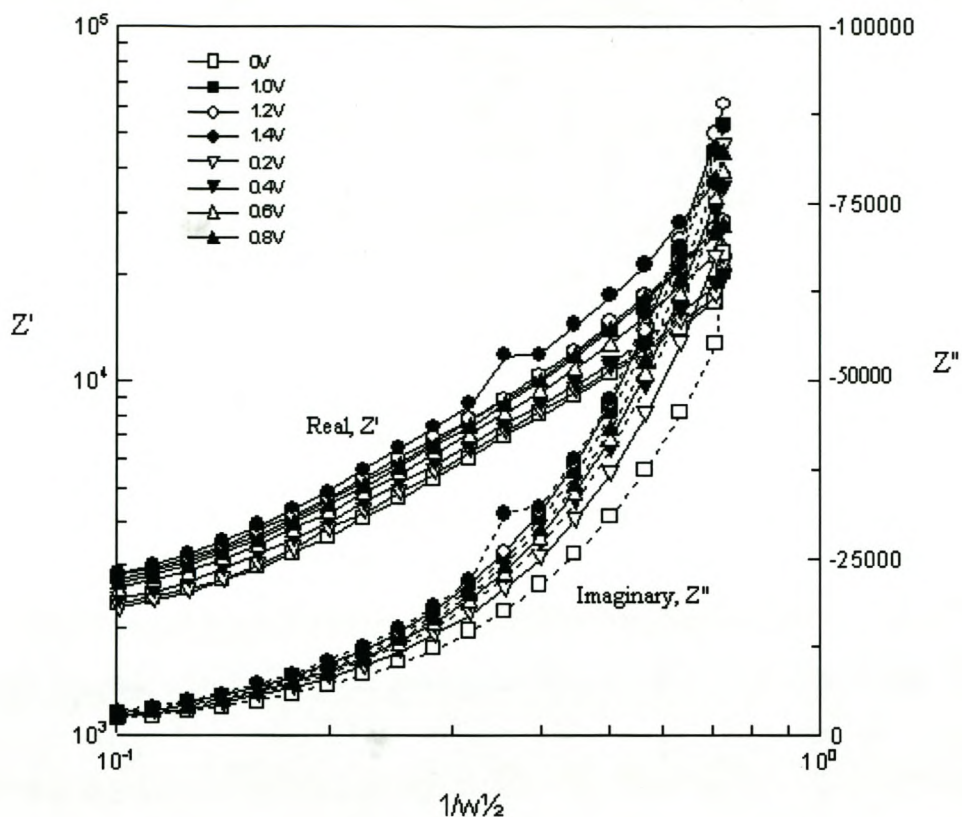


Figure 6.10: Unique plot for Warburg impedance (Z' —, Z'' ----) based on Ti/SnO₂ electrode/solution interface data.

The lines are not parallel and the imaginary component does not intersect the Z axis at zero. Therefore, what appears to be a Warburg impedance from the bode plot diagrams is in fact not. The two series -R-CPE- circuit combination gave the best fit (Table 6.4).

Table 6.4: Equivalent circuit fitting results for Ti/SnO₂

Sample	R1, Ω	CPE1-T, Farads	CPE1-P	R2, Ω	CPE2-T, Farads	CPE2-P	R3, Ω
0	291.9	1.51E-12	1.36	2102	1.12E-05	0.88	773690
100	285	1.65E-12	1.36	2013	1.69E-05	0.88	1126600
200	343	1.56E-12	1.37	2001	1.04E-05	0.87	1.56E+06
300	360.1	1.48E-12	1.37	2020	1.03E-05	0.88	2.07E+06
400	292.9	1.69E-12	1.36	2136	9.93E-06	0.87	1.65E+06
500	299	1.60E-12	1.36	2155	1.01E-05	0.87	2.37E+06
600	295	1.60E-12	1.36	2146	1.00E-05	0.87	7.72E+05
700	296.3	1.56E-12	1.36	2142	9.86E-06	0.87	5.72E+05
800	289	1.62E-12	1.35	2125	9.45E-06	0.87	2.96E+05
900	296.5	1.59E-12	1.36	2127	8.85E-06	0.88	1.07E+05
1000	295.7	1.61E-12	1.36	2131	8.55E-06	0.87	9.80E+04
1100	292.8	1.65E-12	1.36	2144	7.98E-06	0.87	1.43E+05
1200	297	1.59E-12	1.36	2139	7.32E-06	0.87	1.77E+05
1300	292.6	1.61E-12	1.36	2144	6.81E-06	0.86	2.08E+05
1400	291	1.60E-12	1.36	2141	6.37E-06	0.86	1.86E+05
1500	287.8	1.62E-12	1.36	2116	5.74E-06	0.87	5.74E+04

It is not clear why CPE-P values for the high frequency region exceed 1, but fixing the CPE-P = 1 results in unrealistic solution resistance values. As the potential is increased from 0 mV to 1500 mV the capacitance (CPE2-T) and the charge transfer resistance (R3) at the interface decreases. This means that the addition of SnO₂ to the titanium substrate improves the conduction of electrons at the interface. The addition of SnO₂ to the Ti substrate decreases the charge transfer resistance (R_{ct}) of

the bulk material from $\pm 4000 \Omega$ to $\pm 2000 \Omega$. This means that Ti/SnO₂ is more conductive compared to uncoated Ti.

6.4.3 Titanium substrate coated with SnO₂/CuO, in 0.001 M H₂SO₄

The CuO/SnO₂ thin film composition appears to have some activity of its own independent of ions in solution, at potentials between 0 to 500 mV. Two complete semicircles are visible with a third incomplete semicircle appearing in the low frequency region, at potentials between 0 mV and 500 mV (Figure 6.11). At higher potentials one full semicircle is observed at high frequencies and an incomplete semicircle at low frequencies.

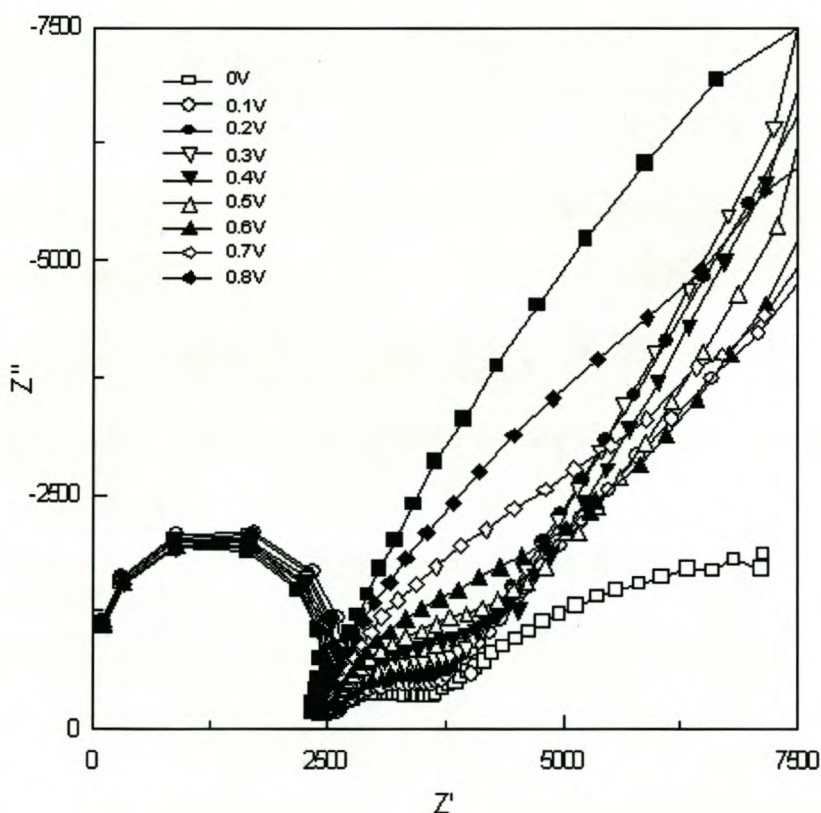


Figure 6.11: Complex plot of Ti/SnO₂/CuO.

The *ecc* used to fit the data has three series –R-CPE- combinations, which give a good fit throughout the potential range (Figure 6.12).

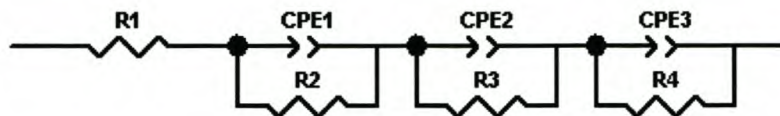


Figure 6.12: Electrical equivalent circuit for CuO/SnO₂.

The results of data fitting are given in Table 6.5.

Table 6.5 Equivalent circuit fitting results for Ti/CuO/SnO₂ electrode in H₂SO₄

mV	R1	CPE1-T	CPE1-P	R2	CPE2-T	CPE2-P	R3	CPE3-T	CPE3-P	R4
100	209.6	8.87E-13	1.39	3194	9.11E-06	0.347	3269	3.49E-05	0.682	37096
200	123.8	9.61E-13	1.38	3236	1.34E-05	0.422	2173	2.05E-05	0.709	213210
300	258.2	8.91E-13	1.385	2886	3.23E-06	0.619	2071	1.50E-05	0.715	492140
400	269	8.69E-13	1.388	2804	3.44E-06	0.6187	2521	1.19E-05	0.719	762240
500	279.2	8.83E-13	1.386	2802	3.24E-06	0.638	3003	9.74E-06	0.71	970010
600	286.4	8.41E-13	1.388	2772	4.21E-06	0.614	4638	7.27E-06	0.734	583360
700	277.5	9.09E-13	1.38	2765	3.19E-06	0.684	4558	6.36E-06	0.67	1058600
800	248.6	9.72E-13	1.385	2505	3.57E-06	0.688	8946	4.51E-06	0.693	663860
900	236.6	1.05E-12	1.385	2328	2.77E-06	0.798	11758	3.16E-06	0.674	617810
1000	226.5	1.84E-12	1.378	2295	2.21E-06	0.854	20699	1.98E-06	0.7187	523180
1100	223.9	1.29E-12	1.372	2338	1.57E-06	1.033	269830	1.12E-06	0.765	148510
1200	242	1.19E-12	1.376	2329	1.12E-06	1.024	284730	1.12E-06	0.768	152150
1300	251.2	1.20E-12	1.375	2345	8.69E-07	1.033	306880	1.09E-06	0.772	137480
1400	256.8	1.18E-12	1.375	2386	8.07E-07	1.033	316790	1.06E-06	0.774	139580
1500	262.3	1.15E-12	1.375	2403	7.91E-07	1.033	300430	9.88E-07	0.781	151180

The high frequency semicircle has fit parameters (CPE1-T, R1) similar to undoped SnO₂. The appearance of an intermediate semicircle (CPE2-T, R2) at applied potentials between 0mV and 500 is ascribed to the oxidation of Cu¹⁺/Cu²⁺ within the catalyst material. The standard reduction for Cu²⁺ to Cu¹⁺ in acidic solution is given as 0.159 V (vs. SHE) [75]. Under the reducing acid environment produced by 0.001 M H₂SO₄ the Cu¹⁺ oxide is favoured. Upon stepping the applied potential in a positive direction, the Cu²⁺ oxide is formed within the SnO₂ host material. At potentials above 500 mV this intermediate semicircle associated with the oxidation of copper, disappears. This means that the copper oxide within the host material is present as CuO under forced anodic conditions, but can be reduced to Cu₂O in a reducing acid environment (i.e. 0.001 M H₂SO₄). A repeat of the experiment with the same sample shows changes to the bulk material due to this redox behaviour of the copper oxide in the first experiment (smaller semicircle at high frequency) and confirms the oxidation of Cu¹⁺/Cu²⁺ under conditions of applied anodic potentials, within the SnO₂ host (Figure 6.12).

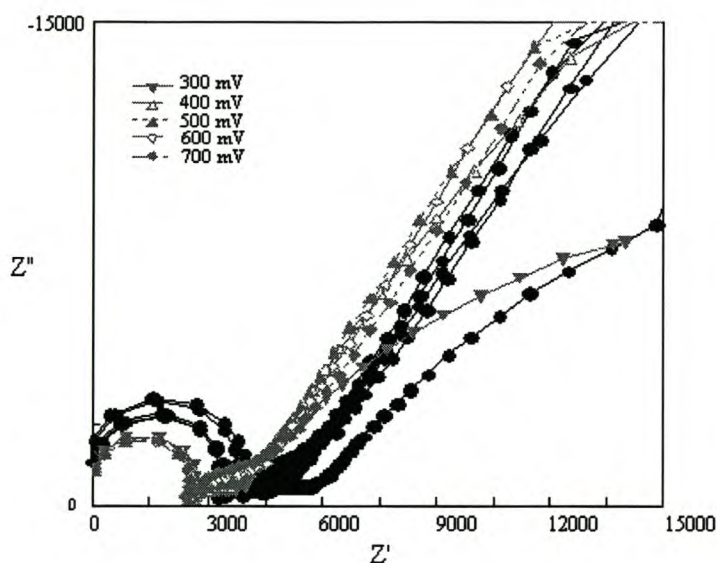


Figure 6.12: Complex plot of Ti/SnO₂/CuO showing the first experiment (black) and the repeat experiment (gray).

A decrease in capacitance (CPE3-T) with increasing potential, in the low frequency loop was also observed for Ti/SnO₂/CuO interface in 0.001 M H₂SO₄ (Figure 6.14).

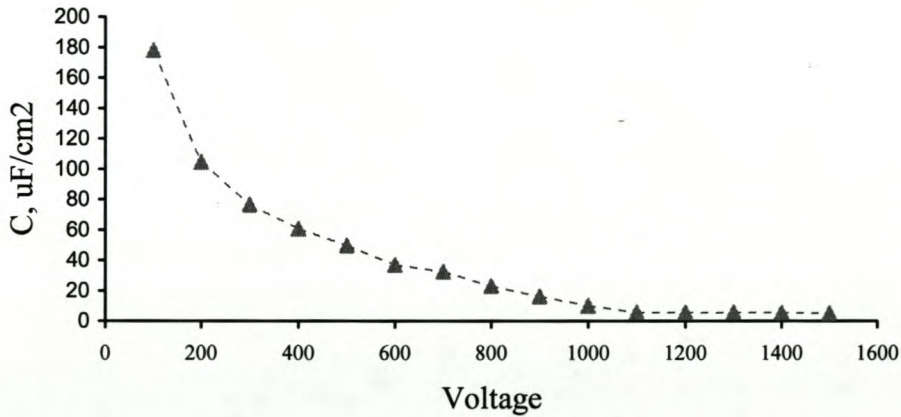


Figure 6.14: Capacitance vs voltage curves for the Ti/SnO₂/CuO thin film

The low frequency capacitance behaviour as a function of applied potential at the Ti/SnO₂/CuO electrode, reflects the change in thickness of the double layer at the interface of the electrode in 0.001 M H₂SO₄. This trend can be related to anion adsorption at the interface, as discussed for the uncoated Ti electrode. The increase in charge transfer resistance (R₄) at the interface as the potential is stepped, implies that the anode becomes increasingly resistant to further electron exchange in the acidic electrolyte.

6.4.4 Titanium substrate coated with SnO₂/MnO_x in 0.001 M H₂SO₄

The high frequency arc of the manganese doped tin oxide does not intersect the imaginary or real axis at zero but hangs suspended ($Z'' = -1000$) and incomplete (Figure 6.15).

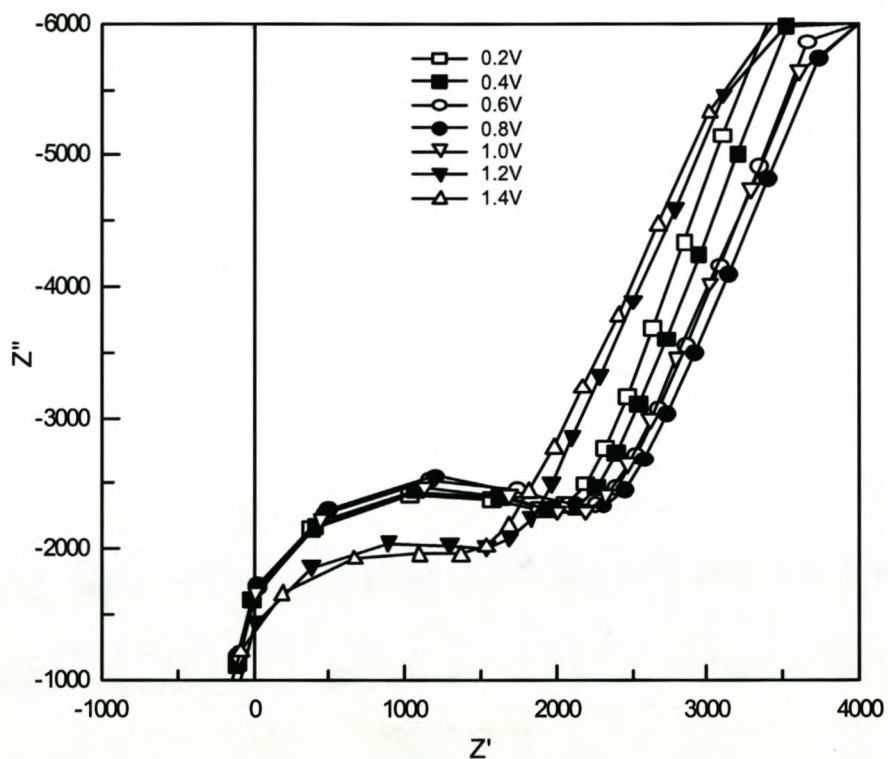


Figure 6.15: Complex plot of Ti/SnO₂/MnO_x electrode/ solution interface.

This is similar to the complex plot behaviour of the uncoated Ti. It could be as a result of instrumental error, but is more likely due to the characteristics of the uncoated Ti. The high frequency end of the spectrum is related to the properties of the bulk material and this observed shift away from zero on the y-axis, could be as a result of a surface effect. The presence of surface cracks in the catalyst thin film exposing the uncoated substrate, may explain the similarity of the impedance behaviour of the MnO₂/SnO₂ thin film to that of uncoated Ti,. This impedance effect is also observed in the complex plot of the PdO₂/SnO₂ solution interface.

The eec in Figure 6.8(a) was used to fit the impedance data obtained for the Ti/MnO₂/SnO₂ in H₂SO₄ and the results are given in Table 6.6.

Table 6.6: Equivalent circuit fitting results for Ti/MnO₂/SnO₂ electrode in H₂SO₄

Potential, mV	R1, Ω	CPE1-T, Farads	CPE1-P	R2, Ω	CPE2-T, Farads	CPE2-P	R3
0	-11.99	6.39E-13	1.44	1574	9.01E-09	0.81	750560
200	-79.5	5.82E-13	1.47	1272	1.21E-08	0.79	573020
400	-91.08	6.76E-13	1.46	1320	1.41E-08	0.77	481550
600	-56.15	5.86E-13	1.46	1416	1.50E-08	0.77	360400
800	-21.7	5.45E-13	1.465	1461	1.33E-08	0.78	235770
1000	-74.14	5.98E-13	1.46	1364	1.65E-08	0.76	214550
1200	-132.2	5.80E-13	1.49	917.7	1.78E-08	0.76	173130
1400	-167.1	6.66E-13	1.47	882	1.77E-08	0.76	150160

The capacitance of the interfacial double layer (CPE2-T) increases as the potential is increased. This implies a charging effect as more energy is supplied to the system by stepping the potential (Figure 6.16). The CPE2-P values decrease concurrently, indicating that the interface less capacitive in nature. The initial high values of charge transfer resistance at the interface (R3) decrease accordingly.

As the capacitance increases, so the conductivity at the interface also increases.

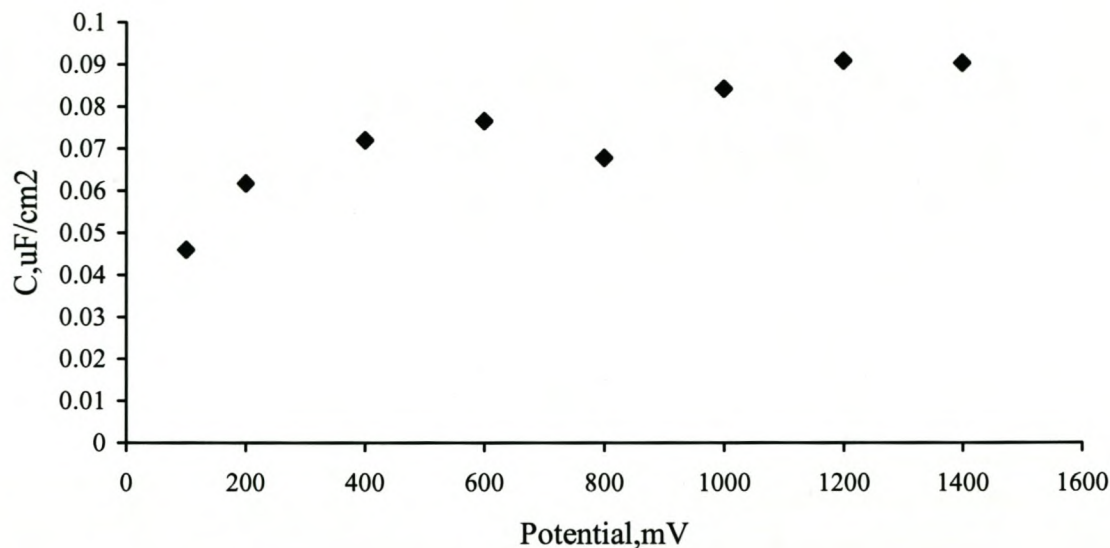


Figure 6.16: Capacitance – voltage plot for Ti/SnO₂/MnO_x electrode in H₂SO₄.

6.3.5 *Titanium substrate coated with SnO₂/PdO₂, in 0.001 M H₂SO₄*

The palladium doped tin oxide gave two clearly distinctive depressed semicircles, which were fitted to two series RC circuits (Figure 6.8a). The high frequency semicircle is fairly consistent in its parameter values. As the potential is increased between 0.1 to 1.4V the low frequency arc decreases progressively (Figure 6.17). This means that the conductivity at the interface improves, as the potential is increased.

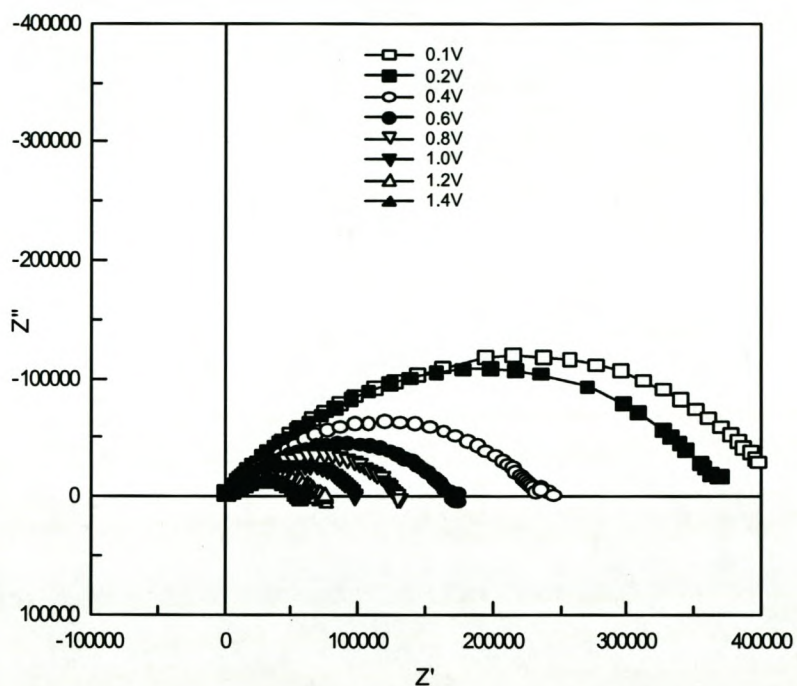


Figure 6.17: Complex plot of Ti/SnO₂/PdO₂ electrode in H₂SO₄.

From capacitance versus voltage plots, an increase in interfacial charging is observed as the potential is increased (Figure 6.18).

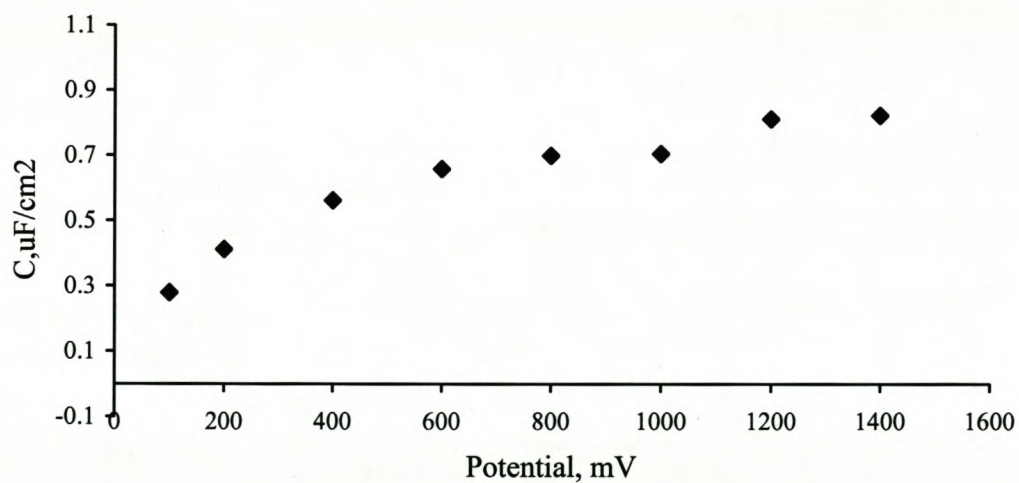


Figure 6.18: Capacitance – voltage plot for Ti/SnO₂/PdO₂ electrodes in H₂SO₄.

The charge transfer resistance at the interface (R3) decreases accordingly (Table 6.7).

Table 6.7: Equivalent circuit fitting results for the Ti/PdO₂/SnO₂ electrode in H₂SO₄

Potential, mV	R1, Ω	CPE1-T, Farads	CPE1-P	R2, Ω	CPE2-T, Farads	CPE2-P	R3
0	-465.2	3.45E-13	1.5	1707	5.47E-08	0.64	424450
200	-506	3.29E-13	1.5	1764	8.06E-08	0.61	389000
400	-433.5	6.16E-13	1.44	2118	1.10E-07	0.59	242840
600	-437.4	5.86E-13	1.45	2083	1.29E-07	0.58	175520
800	-431.4	5.76E-13	1.45	2045	1.37E-07	0.58	132460
1000	-423	5.60E-13	1.45	1958	1.38E-07	0.58	99783
1200	-495.4	4.06E-13	1.48	1768	1.59E-07	0.56	75381
1400	-496	3.93E-13	1.48	1722	1.61E-07	0.56	59286

This implies that charging of the interfacial region, by stepping the potential, gives rise to oxide layer formation at the surface, with higher conductivity compared to the uncharged electrode interface. The capacitance – voltage characteristics of the Ti/SnO₂/PdO₂ electrode in H₂SO₄, are similar to those of manganese doped tin oxide electrode interface.

6.3.6 Titanium substrate coated with SnO₂/ZrO₂, in 0.001 M H₂SO₄

From the complex plot of the data obtained at the Ti/SnO₂/ZrO₂ electrode interface, the low frequency arc does not close and it dominates the high frequency arc (Figure 6.19). The change in the size of the high frequency arc can be related to

potential dependent changes within the bulk material, indicating some instability within the electrode material.

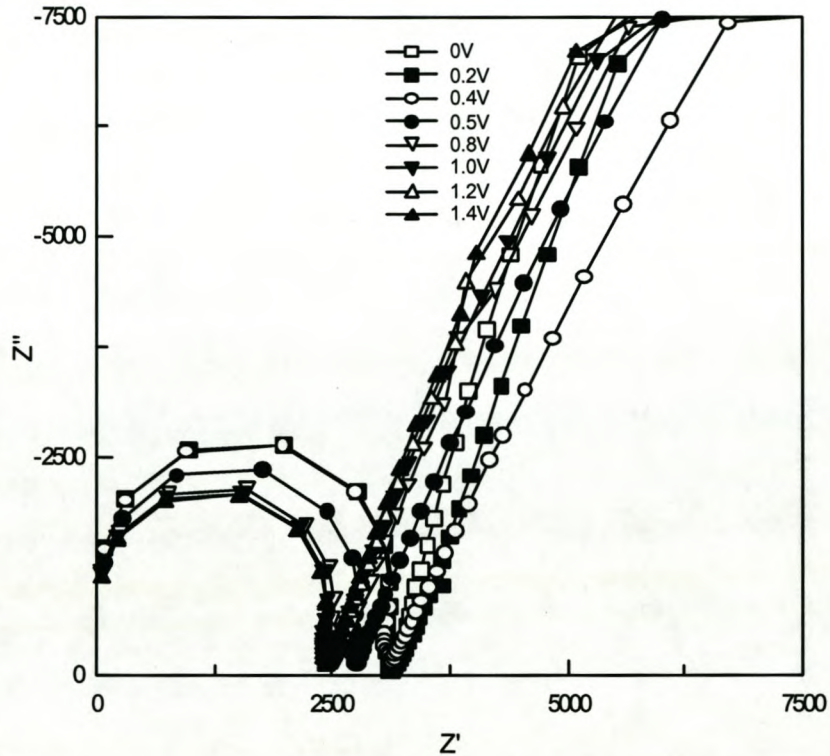


Figure 6.19: Complex plot of Ti/SnO₂/ZrO₂ electrode in 0.001 M H₂SO₄.

The bode plots for these mixed metal oxides also have the characteristic 45° slope at low frequency, suggesting Warburg impedance, but as has been demonstrated with the undoped tin oxide data, data here does not fit the diagnostics plots for Warburg impedance.

The decreasing size of the high frequency arc, as the potential is stepped from 0 to 1.4V, indicates that the conductivity of the bulk material increases. This can be

clearly seen in the decreasing values of the charge transfer resistance parameter, R_{ct} (Table 6.8). The CPE2-P value is close to 1, indicating the capacitive nature of the interface.

Table 6.8: Equivalent circuit fitting results for the Ti/SnO₂/ZrO₂ electrode in H₂SO₄

Potential, mV	R1, Ω	CPE1-T, Farads	CPE1-P	R2, Ω	CPE2-T, Farads	CPE2-P	R3, Ω
0	259.9	1.76E-12	1.34	2642	3.91E-06	0.82	5.18E+06
100	258.2	1.73E-12	1.34	2621	2.74E-06	0.83	4.18E+06
200	260.5	1.17E-12	1.34	2451	2.25E-06	0.82	5.88E+06
300	263.1	1.50E-12	1.35	2552	1.85E-06	0.82	2.88E+06
400	260	1.98E-12	1.32	2576	1.58E-06	0.83	2.46E+06
500	268.9	1.41E-12	1.35	2502	1.48E-06	0.82	2.46E+06
600	269	1.43E-12	1.35	2514	1.26E-06	0.83	2.50E+06
700	270.1	1.40E-12	1.35	2498	1.13E-06	0.84	2.50E+06
800	349.3	1.32E-12	1.36	2392	1.04E-06	0.85	2.50E+06
900	265.4	1.38E-12	1.35	2456	9.57E-07	0.85	2.50E+06
1000	260.3	1.37E-12	1.35	2425	8.94E-07	0.85	2.50E+06

The small high frequency semicircle and in most cases, incomplete semicircle at lower frequency, appears to be characteristic of all the mixed metal tin oxides prepared, with the exception of CuO doped tin oxide.

6.4.7 Titanium substrate coated with $\text{SnO}_2/\text{Sb}_2\text{O}_5$, in $0.001 \text{ M H}_2\text{SO}_4$

Similar to the $\text{SnO}_2/\text{ZrO}_2$ electrode bulk material, a shift in the high frequency impedance profile is observed as the potential is increased (Figure 6.20). The first semicircle merges into the second semicircle with an overlapping loop.

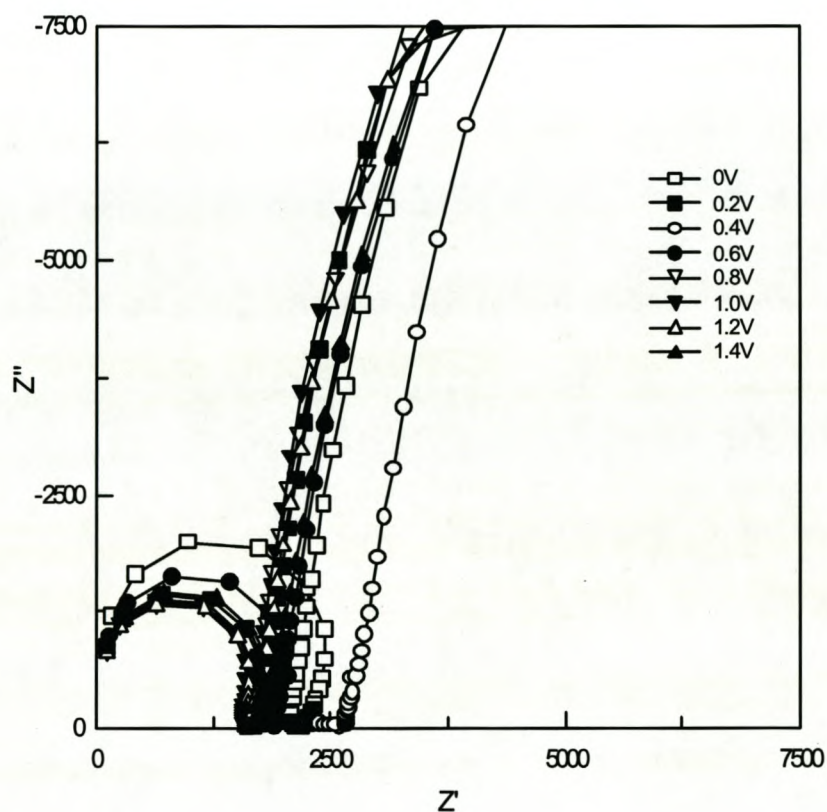


Figure 6.20: Complex plot of $\text{Ti}/\text{SnO}_2/\text{Sb}_2\text{O}_5$ electrode in $0.001 \text{ M H}_2\text{SO}_4$.

The data still gave a good fit with the equivalent circuit (Figure 6.8a), which implies that essentially the kinetics at the interface is still governed by two time constants (Table 6.9).

Table 6.9: Equivalent circuit fitting results for Ti/ SnO₂/Sb₂O₅ electrode in 0.001 M H₂SO₄

Potential, mV	R1, Ω	CPE1-T, Farads	CPE1-P	R2, Ω	CPE2-T, Farads	CPE2-P	R3
0	145	1.06E-12	1.38	2007	2.10E-05	0.93	86973
100	148.3	2.12E-12	1.35	1687	1.84E-05	0.91	96618
200	129.3	2.38E-12	1.35	1558	1.58E-05	0.91	96617
300	123.2	2.61E-12	1.34	1534	1.36E-05	0.92	100370
400	-	-	-	-	-	-	-
500	195.1	1.61E-12	1.35	2091	1.09E-05	0.92	85933
600	145.9	1.79E-12	1.36	1738	1.04E-05	0.91	70694
700	119.8	2.43E-12	1.35	1521	9.94E-06	0.90	65348
800	111.9	2.63E-12	1.34	1471	8.70E-06	0.91	66849
900	108.7	2.76E-12	1.34	1458	7.82E-06	0.92	68790
1000	106.4	2.81E-12	1.34	1464	7.54E-06	0.91	77782
1100	105.5	2.85E-12	1.34	1477	7.56E-06	0.91	87352
1200	106.9	2.86E-12	1.34	1498	7.54E-06	0.90	88542
1300	109	2.87E-12	1.34	1530	7.37E-06	0.89	89302
1400	123.7	2.59E-12	1.34	1611	6.97E-06	0.89	84212

The quality of the data recorded at 400 mV was rather poor. Data cleaning required that too many data points be removed and the spectrum was not included in the data fitting.

The capacitance-voltage characteristics of ZrO_2 and Sb_2O_5 doped tin oxide electrodes, at the solution interface, follow the same exponential trend (Figure 6.21).

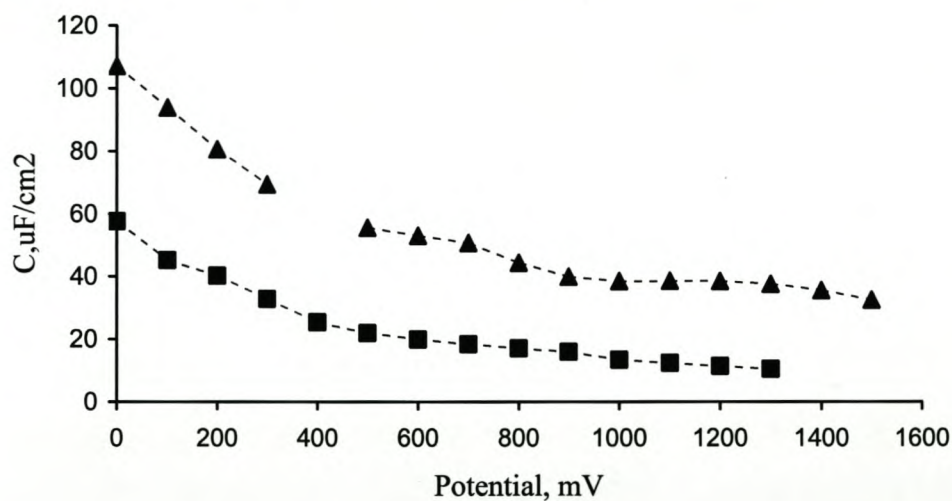


Figure 6.21: Capacitance voltage plots for the (---▲---) $\text{Ti}/\text{SnO}_2/\text{Sb}_2\text{O}_5$ and the (---■---) $\text{Ti}/\text{SnO}_2/\text{ZrO}_2$ electrodes in 0.001 M H_2SO_4 .

The interfacial capacitance of the $\text{Ti}/\text{SnO}_2/\text{Sb}_2\text{O}_5$ electrode is higher than that of the $\text{Ti}/\text{SnO}_2/\text{ZrO}_2$ electrode in H_2SO_4 , over the entire potential range investigated.

6.5 Prediction of double layer capacitance using cyclic voltammetry

It is possible to estimate interfacial capacitance of electrodes in solution, by examining the scan rate dependence of charge at the electrode. Cyclic voltammetry experiments were performed at scan rates of 5 mV/s to 200 mV/s. The relevant plots, based on Equations 6.5 and 6.6, were constructed for the evaluation of inner and outer surface charge distribution at mixed metal tin oxide electrodes in 0.5 M H_2SO_4 .

The CV response at different scan rates can be used to understand the electrochemical interfacial behaviour in terms of accessible surface sites [85]. According to Trassatti's surface formalism, the behaviour that surface charge depend on the scan rate, indicates the existence of different types of accessible sites. The total voltammetric charge (q_{tot}^*) comes from two sources and is related to the entire active surface. The two sources are (i) (q_{in}^*) charges related to inner or less accessible surface regions; and (ii) (q_{out}^*) charges related to the outer surface regions where redox reactions can occur without hindrance. The experimentally measured charge at various scan rates can be linearised if ($1/q_v^*$) is plotted against $v^{1/2}$:

$$(1/q_v^*) = (1/q_0^*) + a(v^{1/2}) \quad (6.5)$$

$$q_0^* = q_{\text{tot}}^* \quad \text{at } v \rightarrow 0 \quad (6.6)$$

The linear extrapolation to $v \rightarrow 0$ gives q_{tot}^* , the surface charge density related to infinitely slow proton exchange (Figure 6.22 a,b).

According to a plot of q_v^* versus $1/v^{1/2}$ at $v \rightarrow \infty$ gives an intercept of q_{out}^* , which represents the amount of charge density related to the outer surface of the oxide. The difference between q_{tot}^* and q_{out}^* will give q_{in}^* , charges related to the inner surface regions.

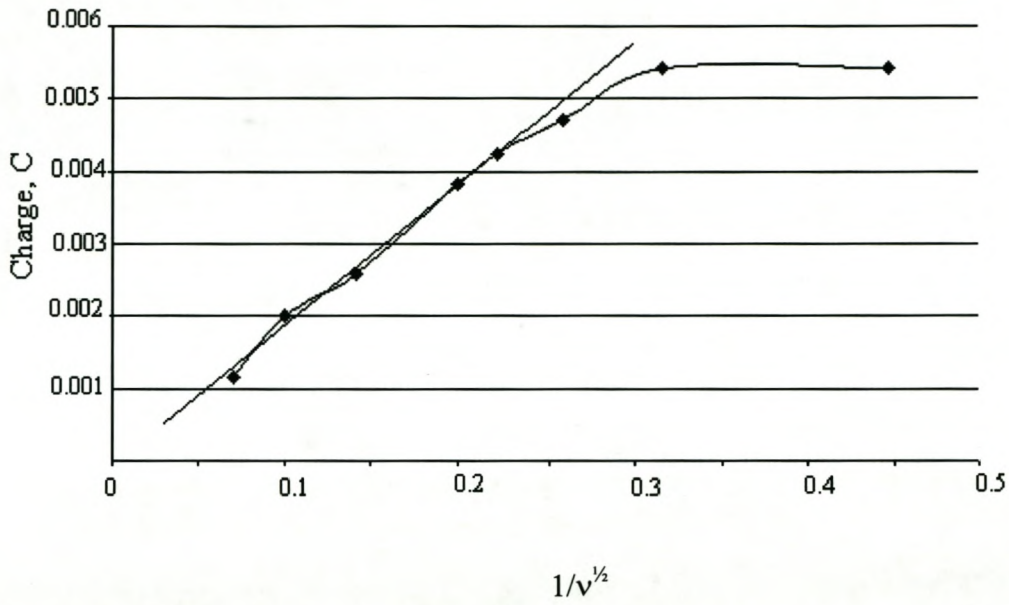


Figure 6.22: (a) Determination of q_{tot} from charge vs scan rate plots for Ti/SnO₂/ZrO₂ electrode.

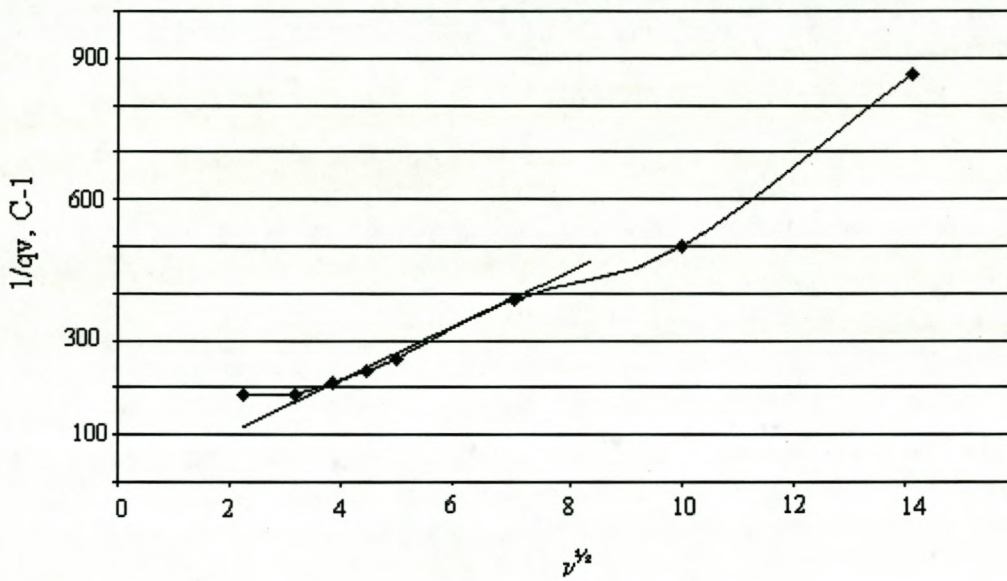


Figure 6.22: (b) Determination of q_{out} from charge vs scan rate plots for Ti/SnO₂/ZrO₂ electrode.

Table 6.10: Values for q_{in}^* , q_{out}^* , and q_{tot}^* obtained for various mixed metal stannates, using cyclic voltammetry

Mixed metal oxide	q_{in}^* , Coulombs	q_{out}^* , Coulombs	q_{tot}^* , Coulombs
Ti/SnO ₂ /Sb ₂ O ₅	13.8×10^{-3}	0.5×10^{-3}	14.3×10^{-3}
Ti/SnO ₂ /ZrO _x	37.8×10^{-3}	2.2×10^{-3}	40×10^{-3}
Ti/SnO ₂ /CuO _x	8.5×10^{-3}	0.3×10^{-3}	8.8×10^{-3}
Ti/SnO ₂ /MnO _x	58.46×10^{-3}	1.54×10^{-3}	60×10^{-3}
Ti/SnO ₂ /PdO _x	23.8×10^{-3}	1.2×10^{-3}	25×10^{-3}

The plots presented two regions of different slopes. For the estimation of surface charges the slow scan rate regions were selected i.e. < 50 mV/s. These experiments follow closely the work of Boodts *et al*, where the double layer capacitance, C_{dl} , of an iridium oxide/solution interface was obtained from the slope of current density versus sweep rate plots [86]. These plots showed a linear relationship for sweep rates between 5 and 200 mV/s, independent of the composition of the oxide mixture.

6.5 Discussion and conclusions

Comparing the fitting parameters obtained for all mixed metal tin oxides shows that the solution resistance for 0.001 M H₂SO₄ varies in the range 200 to 300 Ω. The uncoated Ti surface gave a solution resistance with a wider spread of 200 to 400 Ω. The capacitance and charge transfer resistance of the bulk material can be separated from the capacitance and resistance of the solution interface based on the frequency region of measurements. The high frequency region is associated with material bulk properties whereas the low frequency region can be related to interfacial conditions and reactions.

Table 6.11: Average capacitance and resistance values of mixed metal oxide systems at high frequency, as determined by electrochemical impedance spectroscopy

Mixed metal oxide	Capacitance, F/cm ² *	R, Ω*
Uncoated Ti	1.33E-11	4440
Ti/SnO ₂	8.16E-12	2100
Ti/SnO ₂ /CuO	5.46E-12	2626
Ti/SnO ₂ /MnOx	3.11E-12	1275
Ti/SnO ₂ /PdO ₂	2.43E-12	1896
Ti/SnO ₂ /ZrO ₂	7.14E-12	2500
Ti/SnO ₂ /Sb ₂ O ₅	1.22E-11	1615

* The average of all values recorded over the potential range 0 to 1.5V, was calculated.

The conductivity of the uncoated Ti bulk material was increased by $\pm 50\%$ by the addition of SnO₂ or doped SnO₂ catalyst to the uncoated Ti.

The effect of dopant on the capacitive nature of the electrode material decreases in the order Sb > Sn > Zr > Cu > Mn > Pd. The resistance values of the bulk material, obtained from the equivalent circuit fitting, can be related to the charge carrying ability of the electrode material. The effect of the dopant on the resistance to charge transfer, shows a decreasing trend, i.e. the conductivity increases in the order Cu < Zr < Sn < Pd < Sb < Mn. If we exclude Pd and Mn from these two series, the antimony doped tin oxide has the highest capacitance and conductivity.

The addition of ZrO₂ to tin oxide lowers the capacitance and decreases the charge carrying ability, although the values for the respective parameters are smaller of antimony doped tin oxide. Sb₂O₅/SnO₂ would require a greater input of energy than ZrO₂/SnO₂ initially to overcome its capacitive nature, but should be a better charge carrier than ZrO₂/SnO₂. It is proposed that oxidation at these surfaces would proceed via chemisorbed oxygen i.e. oxygen within the metal oxide lattice and that combustion would be incomplete and give rise to selective oxidation products.

Zirconium and antimony doped tin oxide both show a decreasing trend for capacitance as a function of applied potential, in H₂SO₄ (Figure 6.23). The double layer at the electrode interface and the dielectric capacitance of the oxide film can contribute to the total capacitance measured at the electrode. Since the electrode materials are conductive, it is unlikely that the dielectric capacitance is the cause of

the decreasing trend observed with increasing potential. Anion adsorption, involving partial charge transfer, is usually enhanced when the electrode surface is positively charged. The adsorption pseudo-capacitance would be potential dependent and increase with increasing potential. The variation in capacitance can therefore be attributed to the reduction in specific adsorption of HSO_4^- at electrode surfaces as potential becomes more positive and coverage of O species increases [87]. The undoped SnO_2 and CuO doped electrodes, also exhibit this same decreasing trend in capacitance with increasing potential.

The manganese and palladium doped tin oxide electrodes show similarities in their interfacial behaviour. The increase in double layer capacitance as the potential is increased is typical of potential dependent oxide layer formation [88]. The concurrent decrease in charge transfer resistance at the interface indicates that the oxide layers formed, increase the conductivity of the electrodes compared to that of the unpolarised bulk material. Anodic oxide formation (Figures 6.18 and 6.20) appears to reach a plateau value at around +1200 to 1400 mV. It is therefore possible that a stable oxide layer can be generated that will also have good conductivity.

The capacitance data obtained by EIS do not compare well to the estimations of inner and outer capacitances from CV. Double layer charging effects determined by linear extrapolation of CV data suffer a number of disadvantages. The double layer charging region of the electrode material should be known beforehand, the potential of zero charge is almost certainly changed by the deposition of electrosorbed species i.e. OH and O and the presence of these species affect the potential dependent desorption of previously adsorbed species such as HSO_4^- [87]. It is therefore

reasonable to assume that the data obtained from EIS is more realistic than the information obtained by extrapolation of CV data.

However, the inner and outer capacitance calculated from CV data, do show that the interfacial charge characteristics of PdO₂ and MnO_x doped tin oxide electrodes, are similar to each other. They both have positive values associated with inner surface region charging and the inner charge region dominates the total charging of the interface.

The ZrO₂ doped tin oxide electrode is the only electrode, which has a negative surface charge value as evaluated in acid medium. The magnitude of the surface charge value is also about 10 times bigger than at any other surface in the same electrolyte. EIS data recorded at the ZrO₂ tin oxide electrode interface shows that the electrode material becomes more conductive as the potential is stepped from 0 to 1000 mV and the interfacial capacitance also decreases consistently over this range. The EIS data at the zirconium doped electrode shows the same trends as the data recorded at the antimony doped interface and the copper doped interface. It is therefore reasonable to assume that the interfacial charging data for the zirconium doped tin oxide electrode obtained by CV, is not reliable.

Chapter seven

Electrochemical Impedance Spectroscopy of charge transfer reactions at ZrO_2 and Sb_2O_5 doped tin oxide thin films.

7.1 Introduction

From cyclic voltammetry it emerged that the two electrode compositions worth pursuing for oxidation of organic target molecules were Ti/SnO₂/ZrO₂ (1mol%) and Ti/SnO₂/Sb₂O₅ (10 mol%). The fixed frequency electrochemistry of antimony doped tin oxide has been used as a reference to the newly developed zirconium system. Here we would like to investigate the frequency dependent characteristics of both metal oxide systems in the presence of one or more electron carriers. The antimony doped and zirconium doped tin oxides were evaluated for their electrocatalytic ability using K₃Fe(CN)₆ (one electron system), hydroquinone (more than one electron system) and phenol, the most widely used organic target molecule in preliminary studies targeted at electrolytic water purification.

7.2 Experimental

7.2.1 Preparation of test solutions

An appropriate amount of the potassium ferrocyanide salt was weighed out and made up to volume in 0.001 M H_2SO_4 to produce a 0.002 M $\text{K}_3\text{Fe}(\text{CN})_6$ solution, representing one electron transfer, for evaluation of electron transfer at the mixed metal oxide electrode interfaces. Similarly 0.002 M solutions of hydroquinone ($\text{C}_6\text{H}_6\text{O}_2$) and phenol ($\text{C}_6\text{H}_6\text{O}$) were prepared. Hydroquinone was chosen to represent more complex electron transfer. Since phenol was the original target molecule in water purification applications of the Sb_2O_5 doped tin oxide electrode, some EIS experiments were performed to evaluate the interfacial properties of these electrodes, during oxidation of phenol.

The solutions were stirred and de-aerated in the coating flat cell and the impedance measurements were then recorded at applied potential steps of 100 mV between 0-1500 mV. All experimental parameters were kept the same as in the experiments performed in background electrolyte.

7.3 Results and discussion

7.3.1 Oxidation of $\text{K}_3\text{Fe}(\text{CN})_6$ at $\text{Ti}/\text{SnO}_2/\text{Sb}_2\text{O}_5$ electrode

The data collected for the oxidation of $\text{K}_3\text{Fe}(\text{CN})_6$ at $\text{Ti}/\text{SnO}_2/\text{Sb}_2\text{O}_5$ electrodes, gave a good fit for the series resistance-CPE equivalent circuit, described in Chapter 6 (Figure 6.8a). The solution resistance and the charge transfer resistance

parameters were reduced by approximately half. This reflects the increased conductivity of the solution as a result of the potassium salt added.

The oxidation of $\text{K}_3\text{Fe}(\text{CN})_6$ is observed at 200 to 300 mV (vs Ag/AgCl) and is clearly visible as a closing of the low frequency arc in the complex plot. The oxidation was represented in the equivalent circuit as a nested $-R\text{-CPE-}$ circuit (Figure 7.1).

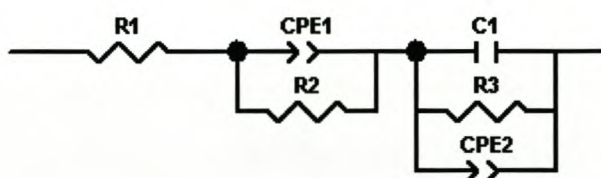


Figure 7.1: Equivalent electrical circuit representing oxidation of $\text{K}_3\text{Fe}(\text{CN})_6$ at $\text{Ti}/\text{SnO}_2/\text{Sb}_2\text{O}_5$.

In the complex plot representing the oxidation of $\text{K}_3\text{Fe}(\text{CN})_6$ at $\text{Ti}/\text{SnO}_2/\text{Sb}_2\text{O}_5$, the low frequency region is of greater importance since it represents the solution interface where electron transfer takes place. The oxidation of $\text{K}_3\text{Fe}(\text{CN})_6$ is confirmed by the closing of the low frequency loop in the oxidation curve, indicated by the open triangles in Figure 7.2. The high frequency loop in the oxidation curve shows some deviation from the same loop in the absence of $\text{K}_3\text{Fe}(\text{CN})_6$. This implies that the surface properties of the electrode material is affected by the oxidation process, taking place at the electrode surface.

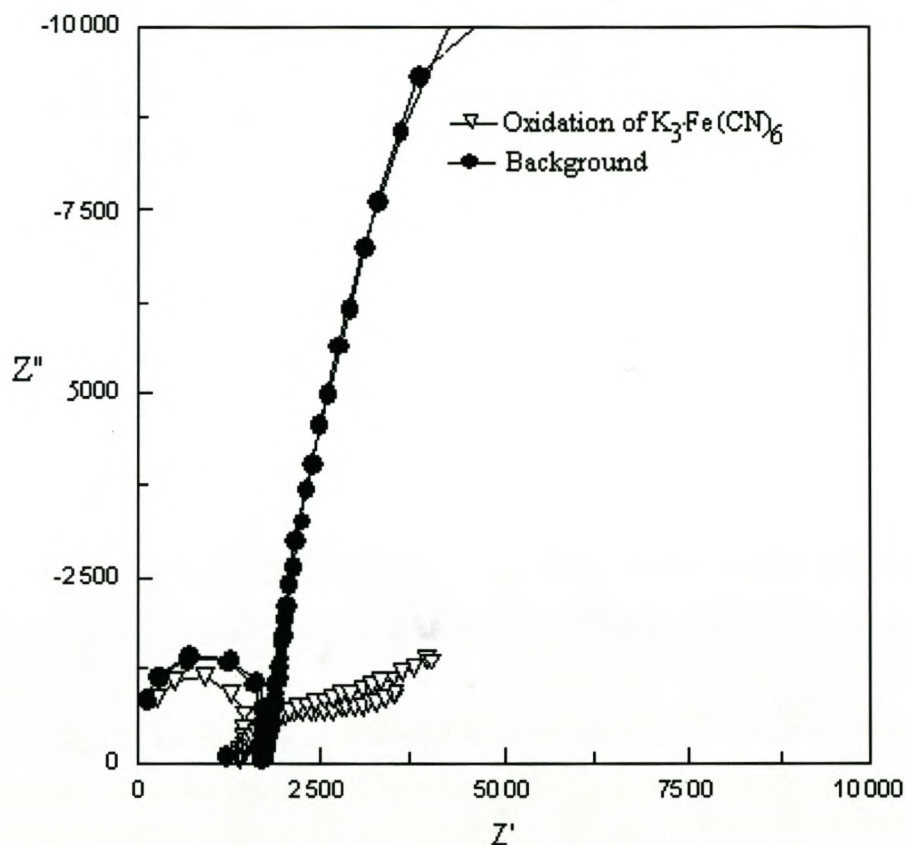


Figure 7.2: Complex plot of oxidation of $K_3Fe(CN)_6$ at $Ti/SnO_2/Sb_2O_5$ electrode at 200 mV to 300 mV.

The results of fitting the data obtained for the oxidation of $K_3Fe(CN)_6$ to the nested – R-CPE- equivalent circuit , is given in below (Table 7.1).

In terms of the electrochemical cell parameters, a reduction in the solution resistance ($\pm 150\Omega$) as a result of the addition of $K_3Fe(CN)_6$, is observed . The bulk electrical properties remain relatively constant over the entire potential range and is comparable to the data obtained in the background electrolyte i.e. $CPE1-P = \pm 2e-12$; $CPE1-T = 1.35$ and $R2 = \pm 1200 \Omega$.

Table 7.1: Parameters for oxidation of $K_3Fe(CN)_6$ at $Ti/SnO_2/Sb_2O_5$ thin film electrodes

Potential, mV	R1, Ω	CPE1-T F	CPE1-P	R2, Ω	C1, F	CPE2-T, F	CPE2-P	R3, Ω
0	171.9	1.72E-12	1.37	1293		2.79E-05	0.89	50440
100	164.1	1.90E-12	1.36	1225		3.27E-05	0.83	23333
200	162.7	2.02E-12	1.36	1227	8.73E-06	3.22E-04	0.25	18948
300	159.5	1.99E-12	1.36	1220	7.13E-06	2.68E-04	0.28	84694
400	155.5	2.008E-12	1.36	1209		1.86E-5	0.85	50679
500	156.3	2.2E-12	1.35	1222		1.21E-5	0.922	97356

The oxidation potential of $K_3Fe(CN)_6$ at the $Ti/SnO_2/Sb_2O_5$ electrode is confirmed in the range 200 to 300 mV and is identified by the closing of the low frequency arc at these potentials.

The low frequency arc that develops as a result of the oxidation taking place under diffusion controlled conditions and can be fitted to an expanded equivalent circuit in the low frequency region. After completion of the oxidation reaction, the electrochemical interface parameters again matched the original circuit, representing two capacitive loops.

7.3.2 Oxidation of $K_3Fe(CN)_6$ at $Ti/SnO_2/ZrO_2$ electrode

The data for the oxidation of $K_3Fe(CN)_6$ at the $Ti/SnO_2/ZrO_2$ electrode, is similar to the data obtained at the $Ti/SnO_2/Sb_2O_5$ electrode. The oxidation of $K_3Fe(CN)_6$ at the zirconium doped electrode, takes place at 200 to 300mV (vsAg/AgCl) (Figure 7.3). The oxidation can be seen in the closing of the low frequency semicircle and is reflected in the reduction of charge transfer resistance values

($R_3 = 4308 \Omega$) at these potentials. The similarity in the complex data obtained for the antimony and zirconium doped electrodes, is not surprising, since cyclic voltammetry scan rate dependence studies indicated that the half wave potentials for these two mixed oxide compositions are very close ($E_{1/2} = 177$ and 146 mV respectively).

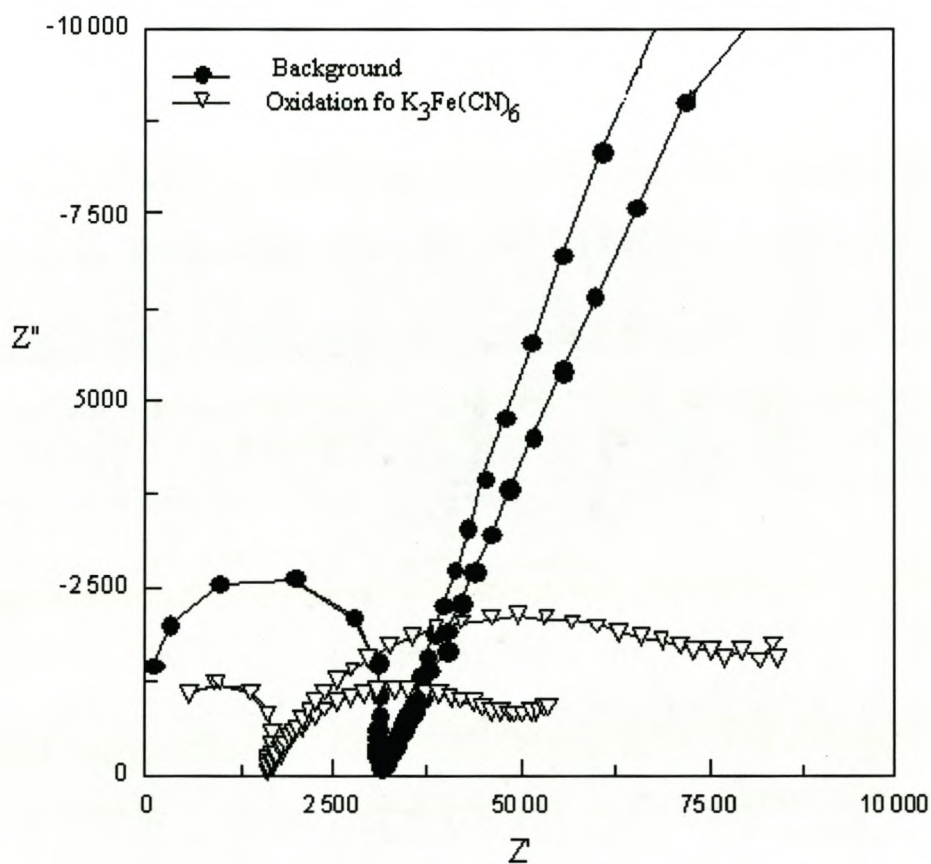


Figure 7.3: Complex plot of oxidation of $K_3Fe(CN)_6$ at $Ti/SnO_2/ZrO_2$ electrode at 200mV to 300 mV.

The low frequency loop undergoes similar changes in its electrical equivalent circuit composition i.e. inclusion of a nested -R-CPE- circuit element to represent oxidation (cf. Figure 7.1) and the fitting parameter values are given in Table 7.2.

Table 7.2: Fitting results for oxidation of $K_3Fe(CN)_6$ at the $Ti/SnO_2/ZrO_2$ electrode

Potential, mV	R1, Ω	CPE1-T F	CPE1-P	R2, Ω	C1, F	CPE2-T, F	CPE2-P	R3, Ω
0	256.9	1.76E-12	1.35	1319		2.12E-05	0.83	38137
100	269.7	1.46E-12	1.36	1313		2.47E-05	0.72	20230
200	273.2	1.55E-12	1.36	1327	7.97E-07	2.97E-05	0.56	4308
300	275.6	1.39E-12	1.37	1309	2.59E-07	1.59E-05	0.62	7737

The fact that two different oxide systems obey the same electrical equivalent circuit for the same redox couple confirms that the lower frequency loop represents charge transfer at the thin films solution interface. The bulk properties would be indicative of the preparation and nature of the electrode material.

7.3.3 Oxidation of hydroquinone ($C_6H_6O_2$) at $Ti/SnO_2/Sb_2O_5$ and $Ti/SnO_2/ZrO_2$ electrodes

Two clearly defined semi circles are evident in the complex plot of the oxidation of hydroquinone at both electrodes. The data obtained, gave a good fit to the two capacitive loop equivalent circuit, in both cases. The low frequency arc shows an incomplete semicircle at around 600-700 mV, which can be associated with the oxidation of hydroquinone at the antimony doped electrode (Figure 7.4).

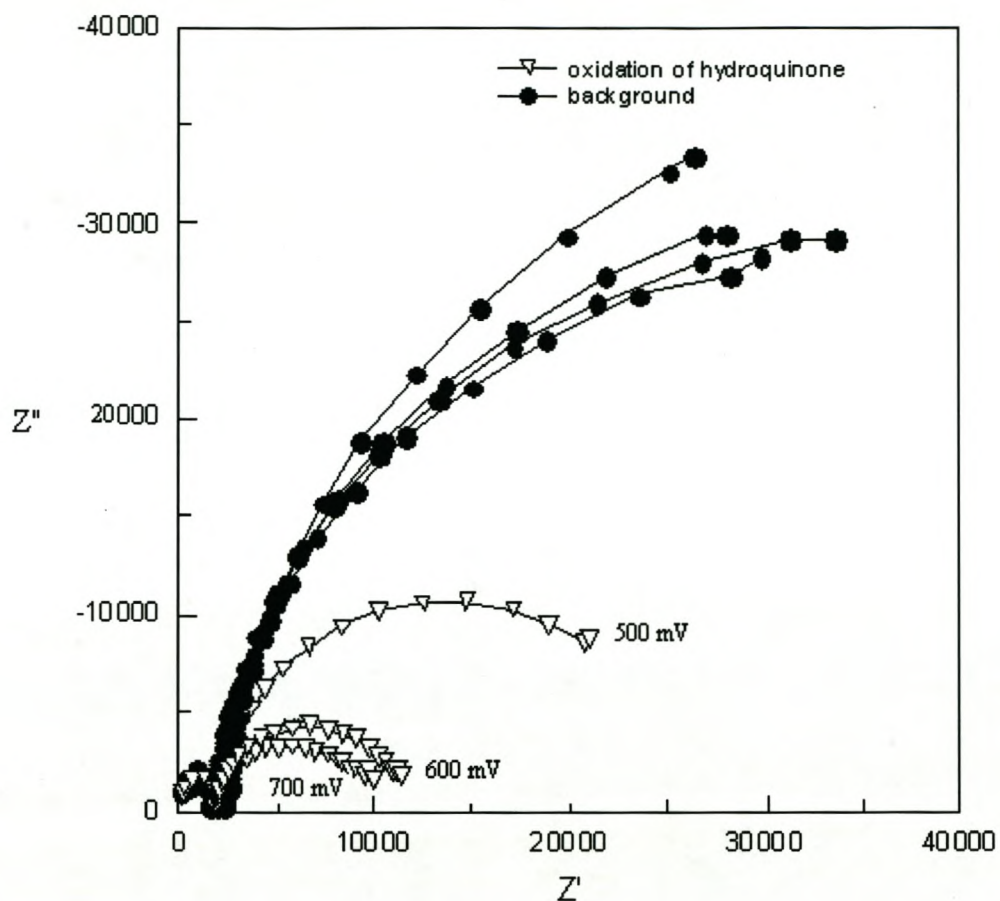


Figure 7.4: Oxidation of Hydroquinone at $\text{Ti/SnO}_2/\text{Sb}_2\text{O}_5$ electrode at 600 mV to 700 mV.

The use of distributed circuit elements throughout, in the equivalent circuit used for data fitting, indicates that the oxidation mechanism at these electrodes rely on adsorption of active species to facilitate the oxidation. It is not evident from the data obtained, to what extent and at what rate the oxidised molecules are removed from the catalytic interface.

The oxidation of hydroquinone at the zirconium doped electrode is observed at higher potentials i.e. 1200 to 1300 mV compared to antimony doped tin oxide (Figure 7.5)

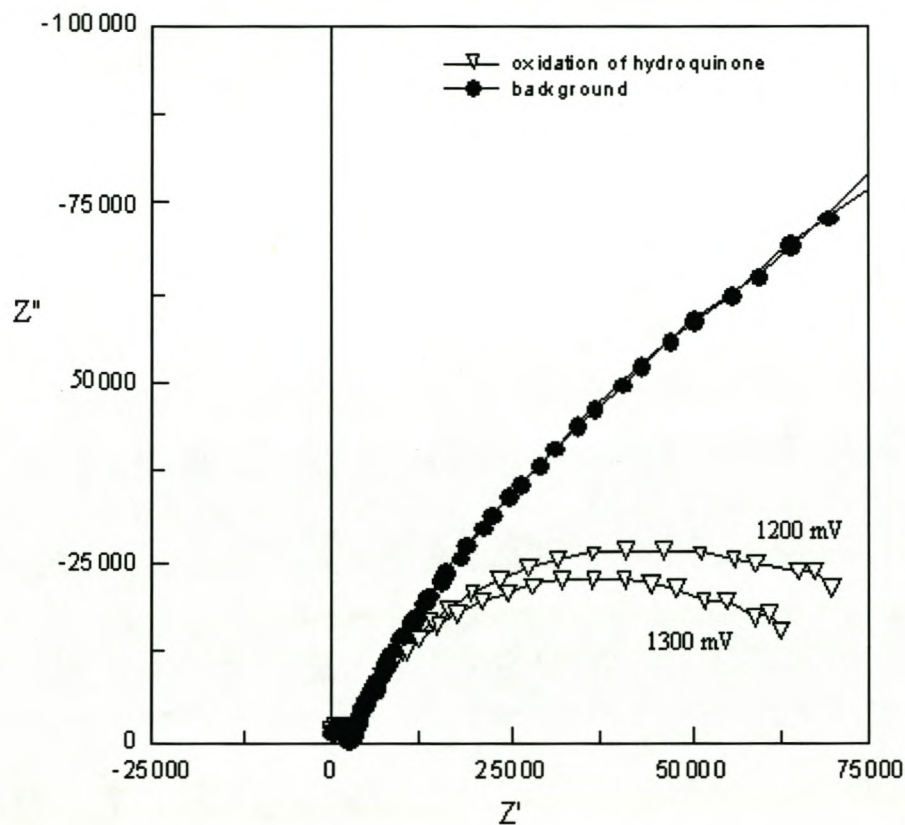


Figure 7.5: Complex plot of oxidation of hydroquinone at $\text{Ti/SnO}_2/\text{ZrO}_2$ electrode at 1200 mV to 1300 mV.

From the complex plot the oxidation at the electrode interface is identified by the change in shape of the low frequency arc to a completed semicircle. From the data fitting results, the oxidation process at the electrode interface is best reflected by the reduction in charge transfer resistance for the low frequency impedance loop (Table 7.3).

The oxidation of hydroquinone at antimony and zirconium doped electrodes does not seem to affect the surface characteristics of the electrodes since no differences between the complex plot of the oxidation curve (open triangles) and the background curve (filled circles) are observed. This was not the case for the oxidation of $K_3Fe(CN)_6$ at these electrodes. It is suggested that this indicates differences in the mechanism of oxidation for $K_3Fe(CN)_6$ and hydroquinone at these mixed metal oxide electrodes.

Table 7.3 Fitting results for oxidation of hydroquinone at $Ti/SnO_2/Sb_2O_5$ and $Ti/SnO_2/ZrO_2$ electrodes

Electrode composition	Oxidation Potential, mV	CPE-T2	CPE-P2	Rct, Ω
$Ti/SnO_2/Sb_2O_5$	600	1.06E-5	0.91	9914
$Ti/SnO_2/Sb_2O_5$	700	1.17E-5	0.87	8191
$Ti/SnO_2/ZrO_2$	1200	2.26E-6	0.78	45497
$Ti/SnO_2/ZrO_2$	1300	2.12E-6	0.78	44214

7.3.4 Oxidation of phenol (C_6H_6O) at the $Ti/SnO_2/Sb_2O_5$ and the $Ti/SnO_2/ZrO_2$ electrodes

The oxidation of phenol at the $Ti/SnO_2/Sb_2O_5$ electrode was not observed in the potential range investigated (Figure 7.6). No difference in the low frequency complex plot is observed for the oxidation curve (open triangles) compared to the

background curve (filled circles). It is possible that the oxidation of phenol takes place at higher potentials.

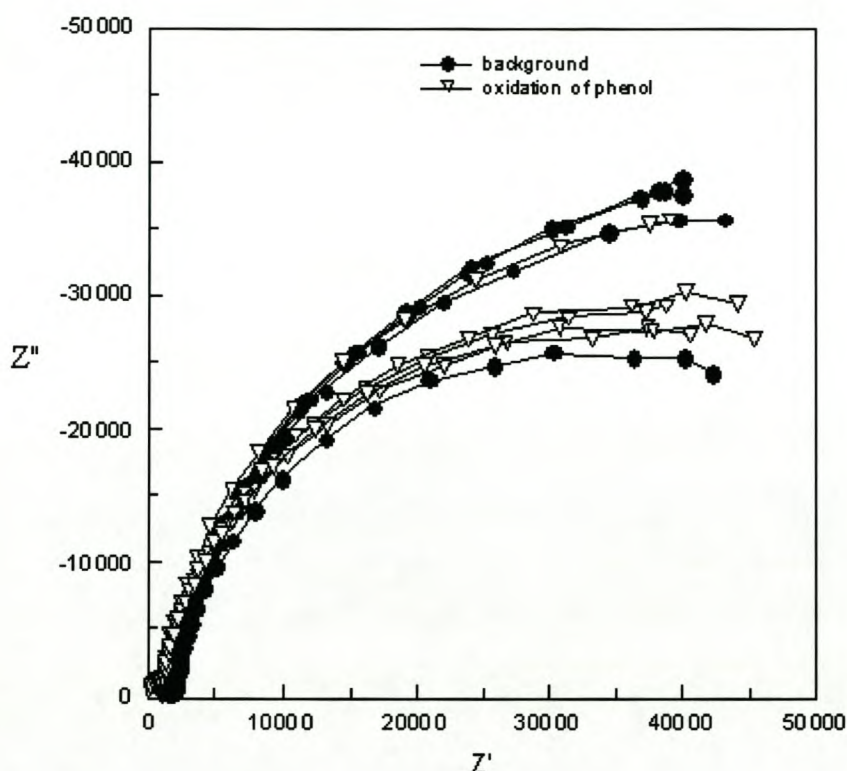


Figure 7.6: Oxidation of phenol at $\text{Ti/SnO}_2/\text{Sb}_2\text{O}_5$ electrode at 1200 mV to 1500 mV.

The high frequency impedance data is indicative of the bulk properties of the electrode material. A reduction in the size of the high frequency loop is observed for the oxidation of phenol at the antimony doped surface (Figure 7.7). It is possible that the electrode surface becomes passivated by the polymerisation of phenol as the potential is increased from 0 to 1500 mV. The polymerised material adsorbed at the electrode active surface is also electrochemically active, even though no oxidation of phenol is indicated by the impedance data.

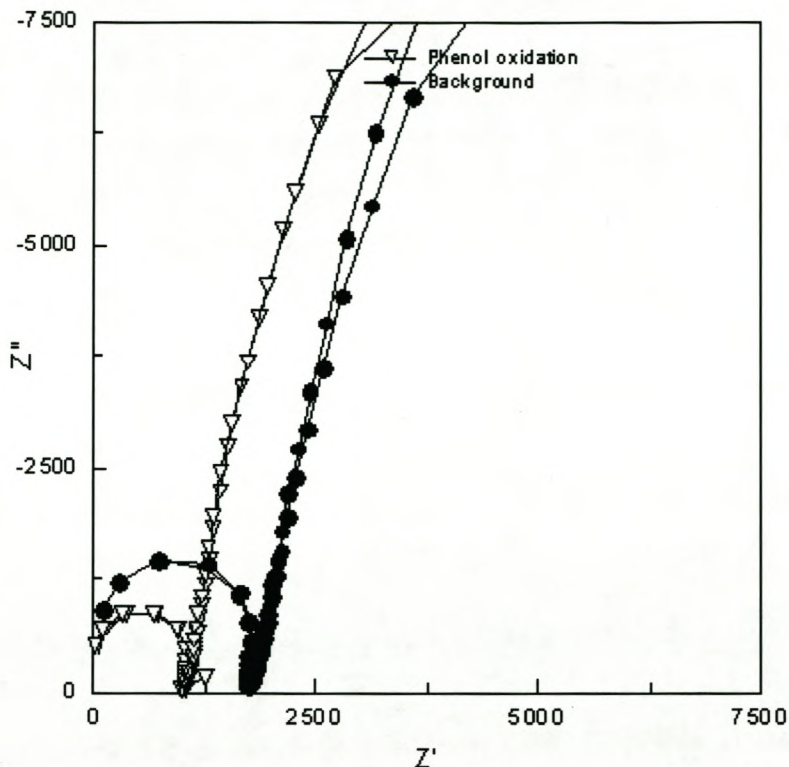


Figure 7.7: Complex plot of oxidation of phenol at $\text{Ti/SnO}_2/\text{Sb}_2\text{O}_5$ electrode, with the high frequency region expanded.

Similarly, the oxidation of phenol was not observed at the zirconium doped electrode over the potential region investigated (Figure 7.8). The oxidation curve (open triangles) was no different from the background curve (filled circles) in the low frequency region.

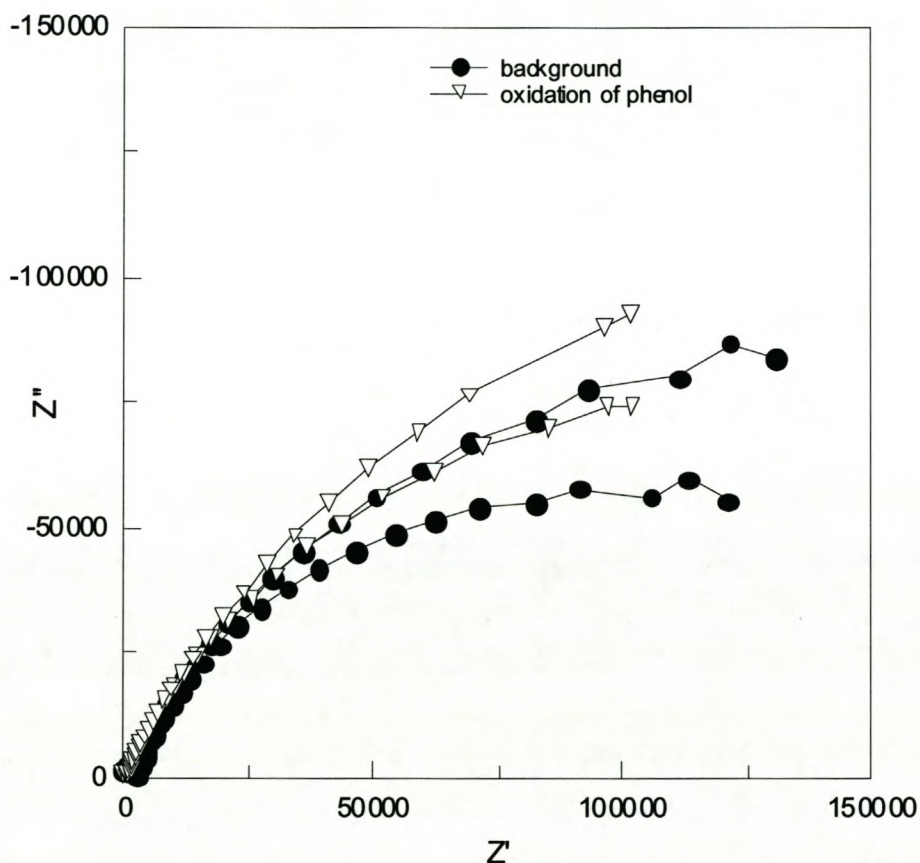


Figure 7.8: Complex plot of oxidation of phenol at the Ti/SnO₂/ZrO₂ electrode at 1400 mV to 1500 mV.

Expansion of the high frequency range of the impedance data shows a similar reduction in the size of the high frequency arc to that observed in the complex plot of phenol oxidation at the antimony electrode. This is associated with changes in the bulk properties of the electrode material (Figure 7.9).

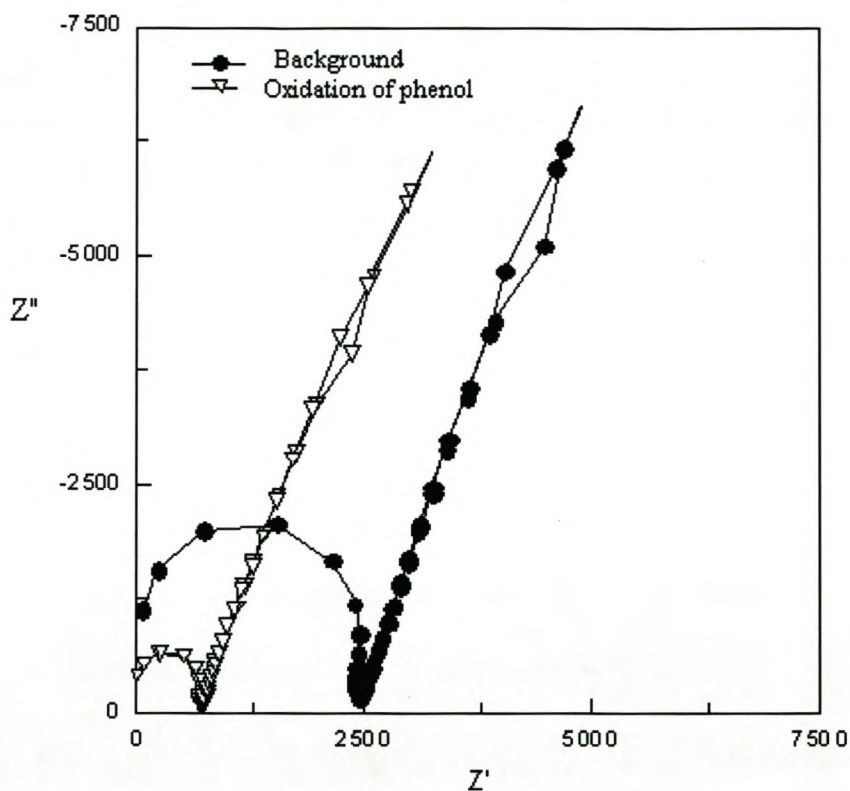


Figure 7.9: Complex plot of oxidation of phenol at Ti/SnO₂/ZrO₂ electrode, with the high frequency region expanded.

7.4 Conclusions

When the number of electrons required for oxidation is limited to one, the Ti/SnO₂/Sb₂O₅ and Ti/SnO₂/ZrO₂ electrodes have similar energy requirements and have the same electrical parameters associated with the interface. However, when the number of electrons required for oxidation increases to two (eg of hydroquinone), excluding aromatic systems, the Ti/SnO₂/Sb₂O₅ is more energy efficient.

The oxidation of phenol at $\text{Ti/SnO}_2/\text{Sb}_2\text{O}_5$ and $\text{Ti/SnO}_2/\text{ZrO}_2$ electrodes is not observed at potentials between 0 and 1500 mV. The $\text{Ti/SnO}_2/\text{Sb}_2\text{O}_5$ electrode has a higher double layer capacitance associated with it and the CPE-P values (close to 1) consistently confirm the capacitive nature of the interface. The values of CPE-P for $\text{Ti/SnO}_2/\text{ZrO}_2$ electrodes, indicate that the interface shows greater deviations from absolute capacitive behaviour. It is suggested that the capacitive nature of the $\text{Ti/SnO}_2/\text{Sb}_2\text{O}_5$ electrodes, facilitate the approach of active molecules to the oxidative surface and this could have a beneficial effect on the oxidation of larger molecules. The absence of this charge space region at the $\text{Ti/SnO}_2/\text{ZrO}_2$ electrodes could prevent larger target molecules from being in close contact with the oxidative surface, for effective oxidation. This could explain why hydroquinone is oxidised at lower potentials at the antimony electrodes than at the zirconium electrodes.

The experiments were not designed to evaluate the rate and extent to which the active molecules are adsorbed and desorbed at the interface, since the test solutions were not stirred in between stepping the potential and collecting data. However this is an important aspect to consider when optimising electrocatalytic ability of an interface. It is possible to evaluate the extent of adsorption and desorption processes under conditions of controlled convection, with techniques such as Electrochemical Hydrodynamic Impedance. EHI could provide information useful in the elucidation of fouling mechanisms at mixed metal tin oxide electrodes.

Chapter eight

Electrochemical treatment of wastewater

8.1 Introduction

Wastewater containing organic pollutants has to be treated by chemical oxidation. Chemical oxidation is often effective in complete elimination of the target organic molecule, but removal of total organic carbon (TOC) is more difficult. An oxidant like ozone only allows for 30% TOC removal [89]. Electrochemical oxidation behaves in a similar way to chemical oxidation but TOC removal is more efficient. It has been demonstrated that doped SnO₂ anodes oxidise a wide range of organic compounds, with efficiency about five times higher than with platinum electrodes [90,91].

8.2 Electrochemical treatment of wastewater

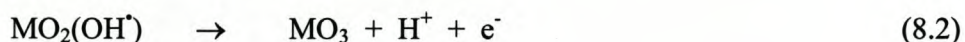
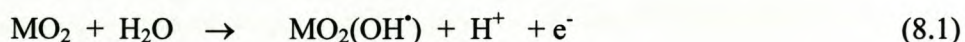
Many industrial wastewater streams contain toxic organic contaminants such as phenols and quinones. Electrochemistry as a tool for the clean up of these waters has attracted much attention since it requires no addition of chemicals to the wastewater and the organic pollutants can be oxidised to less harmful organic acids or even carbon dioxide, using metal oxides as anodes [21].

The electrochemical oxidation of toxic organic waste products can be achieved via (i) direct electrochemical oxidation or (ii) Ag catalysed process. In the direct electrochemical oxidation the organic species is destroyed at the surface of the working electrode. In the Ag catalysed method, Ag(I) is electrochemically oxidised to Ag(II) which oxidises organics to CO₂, CO and H₂O. Inorganic species are converted to their corresponding acids. The remaining Ag(I) is re-oxidised to Ag(II) to continue the process [92].

The low ionic conductivity of many types of wastewater presents a problem in the direct electrochemical oxidation methods, since the electrical resistance between the anode and the cathode is high. The addition of acid, base or salt is required to produce an effective electrolyte for organic waste oxidation.

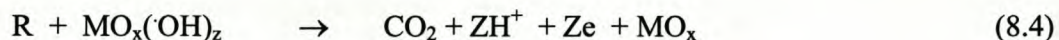
8.2.1 Mechanisms for combustion of organics at metal oxide anodes

The oxidation of toxic organic pollutants in wastewater at metal oxide anodes involves the evolution of oxygen and follows the following general pathway (Equations 8.1 to 8.3).



(The exact pathway of oxygen evolution is dependent on the nature of the metal oxide.)

It has been suggested that the adsorbed hydroxy radical generated as an intermediate species (step 1) is responsible for the oxidation of organic compounds to CO₂. The adsorbed hydroxyl radical may interact with oxygen already present in the oxide anode to form the so-called higher oxide, M_{x+1} (step 2). Therefore at the anode surface we may have two states of active oxygen viz. (i) physisorbed oxygen (adsorbed hydroxyl radicals) and (ii) chemisorbed oxygen (oxygen in the metal oxide lattice). It is suggested that physisorbed oxygen cause the complete combustion of organics (Equation 4), whereas chemisorbed oxygen participate in the formation of selective oxidation products (Equation 5). For the selective oxidation of organics, the concentration of adsorbed hydroxyl radical on the surface must be almost zero [93].



8.3 Organic pollutants in wastewater

Phenols and its derivatives represent a significant proportion of organic pollutants in water. They find their way into our environment as waste products of a number of industrial processes such as the manufacture of plastics, dyes, drugs and antioxidants [94]. Phenols are also by-products of the paper pulp industry and breakdown products of pesticide production. Phenols and substituted phenol compounds are inherently toxic and are of concern as pollutants in a variety of environmental matrices. Classical analytical methods for measuring phenols include colorimetry, chromatography and capillary electrophoresis. These methods are highly sensitive and specific but can be costly. By

contrast electrochemical biosensors have proven to be fast and effective as screening tools for selected phenols [95].

Direct electrochemical oxidation of phenols has a high positive potential of +1.0 V (vs Ag/AgCl) and is subject to the risk of interference from other contaminants in the sample matrix, which can also be oxidised or reduced before this high potential is reached. Carbon paste electrodes imbedded with the enzyme tyrosine have shown good sensitivity towards the detection of mono-phenols and *ortho*-catechols in environmental samples. The enzyme electrode requires no preconcentration and appears more stable and selective. Oxidation by the enzyme is followed by reduction at the electrode, which results in cycling between the catechol and quinone. This cycling effect gives rise to a catalytically amplified signal. The oxidation potential for phenol was observed at -0.2 V (vs Ag/AgCl) and very few environmental contaminants are reduced at potentials between 0 and -0.2 V [96].

Phenol is frequently used as a model organic compound for studying the anodic oxidation process at metal oxide surfaces [97]. Its usefulness as a representative target molecule is hampered by the fact that phenol polymerises at the anode surface. The polymeric film adsorbs on the anode surface, impairing the active electrode area and limiting the evaluation of the effectiveness of different anodes in the oxidation of organic compounds [24,25]. To circumvent the problem of electrode fouling, intermediates of the oxidation process are often used as model organic compounds.

Another widely used organic target molecule in the evaluation of metal oxide surfaces as anodes, is *p*-benzoquinone. Anodes such as Sn(Sb)-oxides, IrO₂ and mixed iridium and titanium oxides, as well as Fe and fluorine doped PbO₂ have been reported as anodes for oxidation of *p*-benzoquinone. It was found that the rate of *p*-benzoquinone removal depends on the chemical nature of the anode material as well as the anode morphology [24].

8.4 Controlled Potential Bulk Electrolysis

Controlled potential bulk electrolysis is also sometimes referred to as coulometry and is widely used to determine the number of electrons involved in an electrode reaction. In contrast to many other electrochemical techniques bulk electrolysis requires a large surface area to sample volume ratio. The potential of the working electrode is fixed at a value where the reaction of interest is proceeding at a mass transport limited rate. The current (or charge which can be found by integration of the current) is then monitored as a function of time, until it drops to very low values, usually about 1% of its initial value. For a simple reaction with constant mass transfer of the type (Equation 8.6);



the current should fall exponentially as defined in Equation 8.7;

$$i(t) = i(0)\exp(-bt) \quad (8.7)$$

and the charge passed as a function of time, $q(t)$, is given by (Equation 8.8):

$$q(t) = \int i dt \quad (8.8)$$

Integration of the current with time gives rise to Equation 8.9:

$$q(t) = q(\infty)(1-\exp(-bt)) \quad (8.9)$$

where $q(\infty)$ is the total charge consumed at the end of the reaction and b is a constant related to mass transfer coefficient and cell and electrode dimensions.

It follows from Equations (8.7) and (8.8.), that a linear plot of $q(t)$ with $i(t)$ should yield a straight line and $q(\infty)$ can be obtained by extrapolation to $i(t) = 0$ or by exhaustive electrolysis. Any deviation from linearity indicates more complex reactions than the one suggested here. The charge at infinity can be related to the number of electrons involved in the overall reaction by Equation 8.10:

$$q(\infty) = nFcV \quad (8.10)$$

Where c is the concentration of electroactive species and V is the volume of solution to which the working electrode is exposed. F is Faradays constant. The value of n obtained is sometimes different from that obtained by other techniques such as cyclic voltammetry or rotating disc electrode and this implies the possibility of coupled reaction mechanisms. This can be verified by independent monitoring of the concentration of the electroactive species using spectroscopic methods i.e. UV analysis, or other methods [55].

8.5 Bulk electrolysis experiments

Careful characterization and electrochemical evaluation of the mixed metal tin oxide electrodes have shown that the $\text{ZrO}_2/\text{SnO}_2$ electrodes show some advantages over the $\text{Sb}_2\text{O}_5/\text{SnO}_2$ electrodes. Application of these electrodes as catalysts for phenol oxidation in a bulk electrolysis set up was performed to measure efficiency of combustion and to identify combustion products by HPLC analysis.

The $\text{ZrO}_2\text{-SnO}_2$ system, which emerged as the best electron carrier with the best energy efficiency in the range of electrocatalysts prepared, was selected as the working electrode in the oxidation of the target molecule, phenol. The oxidation potential of 1.5 V (vs Ag/AgCl reference) was selected as the fixed potential applied to the working electrode, during the bulk electrolysis experiments. Phenol was selected as target molecule for the electrolysis experiments, since it is a common contaminant in wastewater and the current challenge for electrochemical combustion [89, 93, 97]. The proposed scheme for the complete combustion of phenol at dimensionally stable anodes involves the initial conversion to quinones and subsequent degradation to organic acids (Figure 8.1) [98].

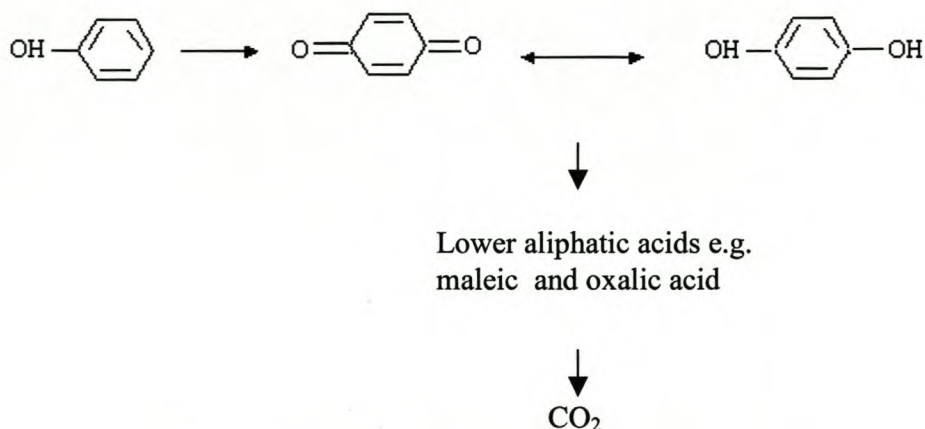


Figure 8.1: Reaction scheme for anodic oxidation of phenol.

Using the 0.001 M H_2SO_4 electrolyte, 0.002 M phenol was prepared as starting solution. The oxidative potential was applied to the working electrode for at least six hours. The initial phenol solution of volume 200 mL, was exposed to the working electrode (1 cm^2 porous surface area). The working electrode and the counter electrode were in the same sample compartment. The phenol solution was purged with nitrogen gas to remove all dissolved oxygen. Samples were collected at one hour intervals and analysed by HPLC to observe the extent of oxidation by monitoring the decrease in the phenol concentration as well as the identity of the breakdown products formed.

Bulk electrolysis experiments were run for one hour initially, on working electrodes of the same composition and size ($\text{ZrO}_2/\text{SnO}_2$, 1 cm^2) exposed to smaller sample volumes ($\pm 15 \text{ mL}$). These shorter experiments were designed to acquire an estimate of the oxidation rate and to see if fouling of the electrode surface will inhibit the effectiveness of electrolysis.

Exhaustive electrolysis (down to 1% of initial current) yielded a value of $q(\infty)$ of about 200 mC (Figure 8.2). However, it is evident that the curve is not a straight line and the assumption of simple oxidation uncomplicated by competing reactions, does not apply. It is therefore not possible to determine the number of electrons involved in the oxidation, accurately, from this simple experiment. More likely we have oxidation competing with adsorption and coupled electrochemical reactions which we will attempt to de-convolute using impedance measurements of the mixed metal oxide interfaces at various potentials.

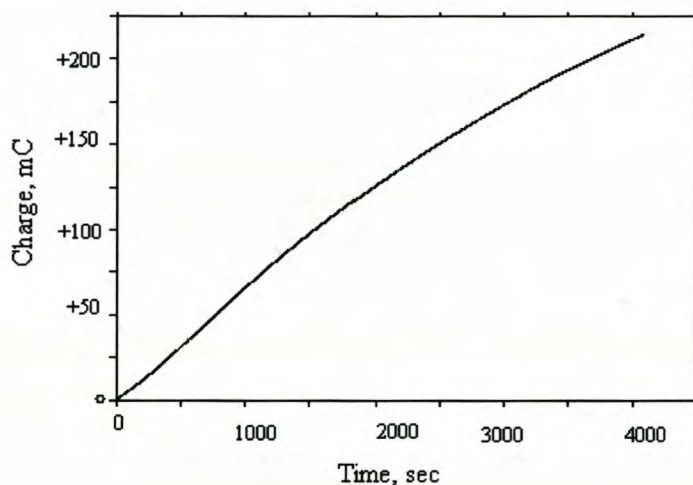


Figure 8.2: Bulk electrolysis of a 0.0019 M phenol solution at the $\text{ZrO}_2\text{-SnO}_2$ electrode for 1 hour.

8.6 Analysis of samples by High performance liquid chromatography

Samples extracted from the bulk solution were analysed on a WATERS Separations module 2690 using a LUNAR C18 column (5 μm particle size; 20 cm long). The mobile phase used was 50:50 methanol–water and detection was done with a WATERS 996

Photodiode Array detector. The method was adapted from literature [18,19,98]. Standards of phenol, hydroquinone, catechol and benzoquinone were prepared for the identification and quantification (calibration curves) of breakdown products [99].

8.6.1 High performance liquid chromatography results

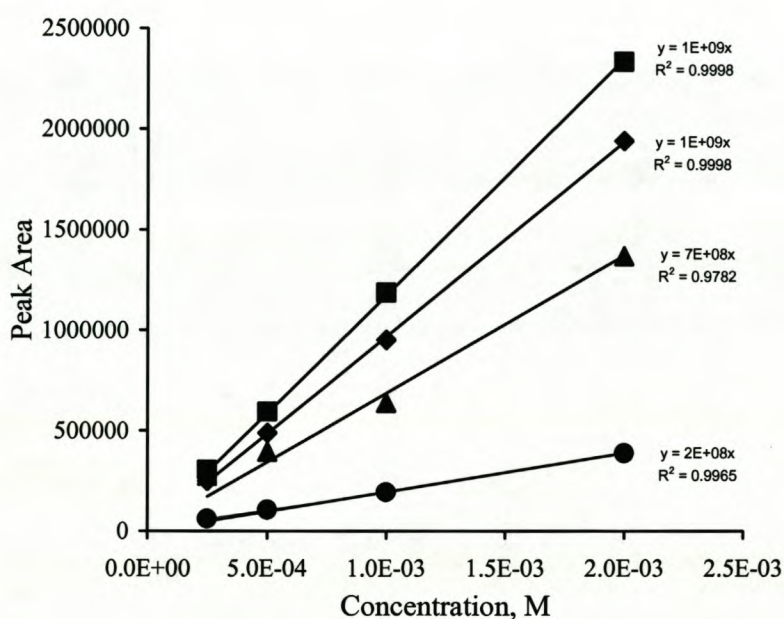


Figure 8.3: Calibration curves for phenol and its breakdown products (◆phenol, ■catechol, ▲hydroquinone, ●quinone).

Standards of phenol, hydroquinone, catechol and benzoquinone were prepared in the concentration range 0.002 M to 0.00025 M (Figure 8.3). Good linearity was maintained over this concentration range for all ($R^2 \sim 0.99$) with the exception of hydroquinone, which gave the lowest regression coefficient ($R^2 \sim 0.96$). The straight line equation was used in

the conversion of peak area to concentration values. The retention times in minutes, for the standards, were: phenol = 4.3, hydroquinone = 1.76, quinone = 2.04 and cathecol = 2.76. These retention times were used to identify breakdown products in the interpretation of the chromatograms (Figure 8.4).

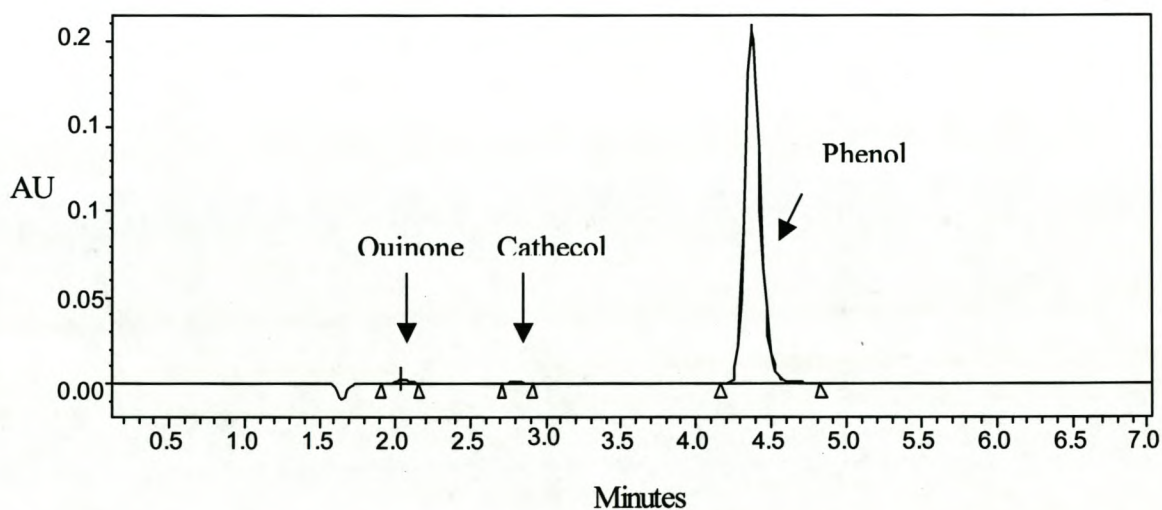


Figure 8.4: An example of a chromatogram obtained for the products of phenol bulk electrolysis (6 hours).

The $\text{ZrO}_2/\text{SnO}_2$ catalyst was effective reducing the initial concentration of phenol (0.0019 M) by 19.3% after 6 hours of electrolysis (Figure 8.5).

Photodiode Array detector. The method was adapted from literature [18,19,98]. Standards of phenol, hydroquinone, catechol and benzoquinone were prepared for the identification and quantification (calibration curves) of breakdown products [100].

8.6.1 High performance liquid chromatography results

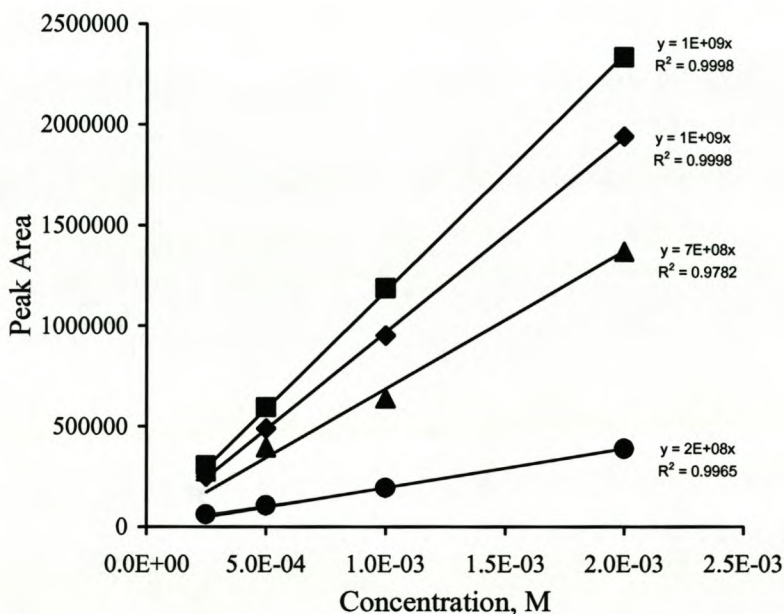


Figure 8.3: Calibration curves for phenol and its breakdown products (♦phenol, ■catechol, ▲ hydroquinone, ●quinone).

Standards of phenol, hydroquinone, catechol and benzoquinone were prepared in the concentration range 0.002 M to 0.00025 M (Figure 8.3). Good linearity was maintained over this concentration range for all ($R^2 \sim 0.99$) with the exception of hydroquinone, which gave the lowest regression coefficient ($R^2 \sim 0.96$). The straight line equation was used in

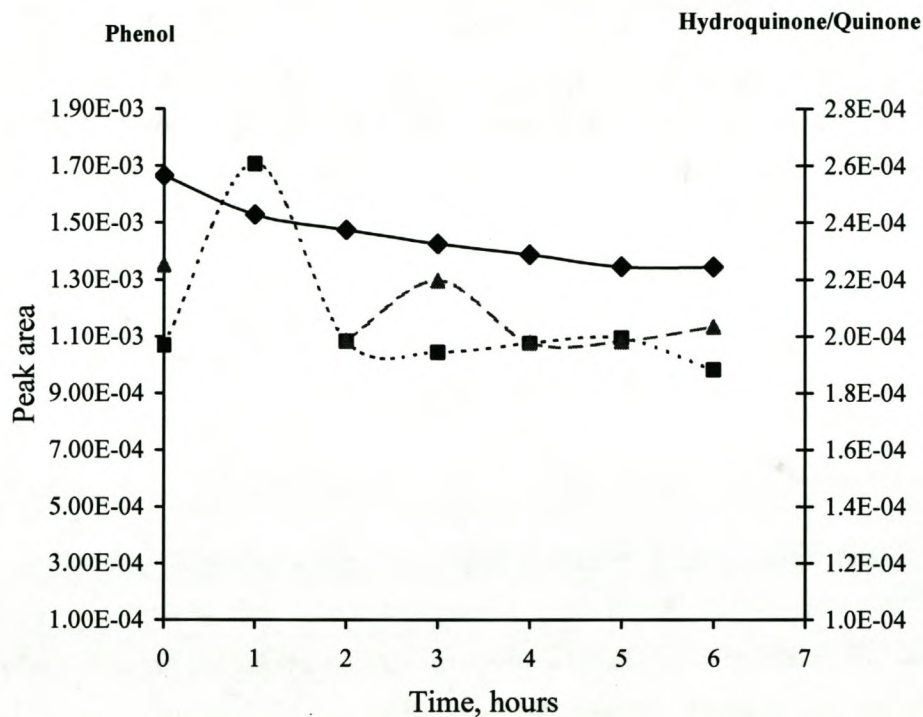


Figure 8.5: Phenol degradation at ZrO_2/SnO_2 electrode (-♦-phenol,--■-- hydroquinone, --▲-- quinone)

The major products of oxidation after six hours of hydrolysis at an applied potential of 1.6 V (DC) was identified as hydroquinone and benzoquinone. From the degradation profiles, it would appear that there is an inter conversion between hydroquinone and quinone initially. The degradation rate of phenol decreases as a result of this interconversion.

8.7 Reactor design and testing of catalyst

A flow through reactor capable of handling volumes up to 50 L and operation times in excess of 24 hours has been designed. Experiments were implemented to observe the effect of prolonged electrolysis on (a) the extent of phenol reduction and (b) the nature of breakdown products observed.

The reactor design and testing of the catalysts formed the basis of an M.Sc project registered at the University of Stellenbosch (Chemical engineering). This joint venture between Chemistry and Chemical Engineering, was financially supported by the Water Research Commission (WRC). The design and optimisation of a scaled up reactor was the focus of Chemical Engineering and the development and characterisation of mixed metal oxide composite electrocatalysts was done by Chemistry. Among the electrocatalysts that were evaluated were $\text{Sb}_2\text{O}_5/\text{SnO}_2$ and $\text{ZrO}_2/\text{SnO}_2$. The success established for phenol degradation at $\text{Sb}_2\text{O}_5/\text{SnO}_2$ electrodes in previous studies could not be reproduced [20]. However the $\text{ZrO}_2/\text{SnO}_2$ electrodes gave promising results in bulk electrolysis experiments and in flow-through reactor testing. The flow-through reactor design based on $\text{ZrO}_2/\text{SnO}_2$ electrocatalyst gave high efficiencies for oxidation of microbes such as *Streptococcus*, *E.Coli* and others [101].

8.8 Conclusions

The oxidation of phenol at $\text{Sb}_2\text{O}_5/\text{SnO}_2$ electrodes was shown to be very efficient and produced predominantly organic acids and CO_2 [93]. Based on cyclic voltammetry experiments, interfacial kinetic and charge transfer efficiency predictions implied that $\text{ZrO}_2/\text{SnO}_2$ electrodes should give improved efficiency for the oxidation of phenol. However the $\text{ZrO}_2/\text{SnO}_2$ catalyst was only effective in reducing the initial concentration of phenol (0.0019 M) by 19.3% after 6 hours.

The reaction appeared to stop at this point. It is possible that a passivating layer is formed over the electrode, inhibiting further breakdown to CO_2 . Quinones, which are byproducts of phenol oxidation, are known to adsorb strongly and irreversibly on Pt electrodes causing similar passivation of the electrode surface [98]. However, experimental conditions of the bulk electrolysis experiment, also affect the eventual breakdown products. At low current density (5 mA/cm^2), high phenol concentration (20 mM) and low phenol conversion only aromatic compounds (benzoquinone, hydroquinone and catechol) are formed [100].

During the six hour electrolysis there is no evidence of ring opening and complete combustion to organic acids. It was therefore not feasible to analyse for acids, at this stage, since the efficiency of conversion was not very good. It has been demonstrated with CV however that the catalyst is effective for one electron exchange reactions. The lack of complete combustion of phenol at $\text{ZrO}_2/\text{SnO}_2$ electrodes, underlines the fact that oxidation mechanisms are strongly dependent on the chemical nature and morphology of the anode.

Chapter nine

Conclusions and recommendations for future work

9.1 Conclusions

Intrinsically doped transition metal tin oxide gels have been prepared successfully using the sol-gel method. Sb_2O_5 , PdO_2 , CuO , MnO_2 and ZrO_2 have been introduced successfully into a SnO_2 host, at very low dopant levels to produce mixed metal oxide electrodes. Sol-gel synthesis of mixed metal oxides was established as an efficient yet simple way to produce intrinsically doped mixed metal tin oxide gels, reproducibly. Thin film electrodes were produced by dip coating the gels onto solid titanium substrates, which were then annealed to produce dimensionally stable electrodes.

In an attempt to produce electrodes with increased surface area, surfactants were added to the mixed metal oxide gels. However, the thin films electrodes produced from these modified gels were not reproducible and not suitable for electrochemical evaluation. Dip coating the mixed metal tin oxide gels onto porous titanium substrates gave the desired thin film electrode with increased surface area.

TGA analysis showed that $\text{PdO}_2/\text{SnO}_2$ formed the most stable phase. It also confirmed that the calcination temperature of 600°C , was high enough to ensure that all mixed

metal oxides form stable phases. UV/vis measurements were able to confirm the band gap energies for all mixed metal oxides to be in the range 2.37 to 3.37 eV. These values are not significantly different from the band gap energy of undoped SnO₂.

XRD analysis was not able to characterise the chemical composition of the thin films, since the catalytic metal oxide element was introduced at very low concentration. XRD analysis of each mixed metal oxide system, only gave confirmation of the syn cassiterite SnO₂ host material.

Morphological characterisation of the thin film electrode surfaces, using SEM confirmed that the coatings were free from cracks and other surface imperfections. AFM was useful in differentiating between thin film preparation techniques. The spin coated samples consistently appeared smoother with lower surface roughness estimates. The morphology of all mixed metal oxide surfaces showed regularly repeating triangular units. It was not possible to relate these patterns to any structural parameters due to limitations of the instrument used.

The PIXE/RBS combination was used to confirm the presence of the dopant atom in the thin film mixed metal tin oxide samples, but quantitative determination was not in good agreement with calculated values. The mixed metal oxide samples did however provide a challenge for the application for this combined technique. Good separation between the titanium (substrate) signal and the signal of the thin film elements was observed. Therefore, quantification as performed, is reliable.

Cyclic voltammetry showed that SnO_2/CuO and $\text{SnO}_2/\text{MnO}_2$ electrodes displayed oxidation and reduction peaks in the background electrolyte, indicating that these mixed metal oxides were not stable anodes for the evaluation of redox reactions. The copper oxide within the tin oxide host material, changes from Cu_2O to CuO as a function of applied potential. In the case of the MnO_2 dopant it is speculated that the dopant undergoes oxidation as the potential is increased to produce species such as H_3MnO_4 and HMnO_4 . These may leach out of the electrode material into the electrolyte and so change the nature of the chemical nature of the electrode material. Evaluating the residual current density as a function of sweep rate showed that PdO_2 , Sb_2O_5 and ZrO_2 doped tin oxide, gave the best linear current density response. Good separation between the residual current and the current due to analyte charge transfer at the electrode surface was observed for Sb_2O_5 and ZrO_2 doped tin oxide, using 0.002 M $\text{K}_3\text{Fe}(\text{CN})_6$ as test solution. These electrodes displayed irreversible electron transfer kinetics, which were confirmed by oxidation and reduction peak separations in excess of 59 mV and low transfer coefficients (Tafel plots).

The efficiency of $\text{SnO}_2/\text{Sb}_2\text{O}_5$ electrodes for the complete oxidation of phenol to organic acids could not be reproduced in bulk electrolysis or flow through reactor experiments. The $\text{SnO}_2/\text{ZrO}_2$ catalyst was effective in reducing the initial concentration of phenol (0.0019 M) by 19.3% after 6 hours of bulk electrolysis. The breakdown products were identified as hydroquinone, quinone and small traces of catechol.

Impedance spectroscopy was used to evaluate the electrical parameters associated with the electrode material and the electrode solution interface parameters. The effect of

dopant on the capacitive nature of the electrode material decreases in the order $\text{Sb} > \text{Sn} > \text{Zr} > \text{Cu} > \text{Mn} > \text{Pd}$ and the resistance to charge transfer, shows a decreasing trend i.e. its conductivity increases in the order $\text{Cu} > \text{Zr} > \text{Sn} > \text{Pd} > \text{Sb} > \text{Mn}$. Undoped tin oxide, Sb_2O_5 , ZrO_2 and CuO doped tin oxide all show a decreasing trend for capacitance versus increasing positive potential. Anion adsorption (e.g. HSO_4^-) would usually be enhanced when the electrode surface is positively charged. The adsorption pseudo-capacitance would be potential dependent and increase with increasing potential. As the potential becomes more positive the electrode coverage of O species increases, causing a reduction in anion adsorption.

The resultant decreasing adsorption pseudo-capacitance contribution, is the reason for the decreasing trend observed in the overall capacitance at these electrode interfaces, as the potential is increased. The reverse trend in double layer capacitance as the potential is increased, observed for manganese and palladium doped tin oxide electrodes, is typical of potential dependent oxide layer formation and growth. Stable anodic oxide formation, is indicated by the plateau reached by this trend, around 1200 to 1400 mV, but the charge transfer properties of these oxide layers have not been investigated further.

Charge transfer characteristics of the interfacial region of Sb_2O_5 and ZrO_2 doped tin oxide electrodes, show that they have comparable energy requirements and reaction efficiencies for the oxidation of $\text{K}_3\text{Fe}(\text{CN})_6$. $\text{SnO}_2/\text{Sb}_2\text{O}_5$ electrodes oxidise hydroquinone at lower potentials and higher efficiency than $\text{SnO}_2/\text{ZrO}_2$. The oxidation of phenol at the $\text{Ti}/\text{SnO}_2/\text{Sb}_2\text{O}_5$ electrode and $\text{Ti}/\text{SnO}_2/\text{ZrO}_2$ electrodes could not be confirmed by impedance spectroscopy at potentials between 0 and 1500 mV.

9.2 Main scientific contributions of the dissertation

We have shown that sol-gel technology is suitable for the preparation of mixed metal tin oxides of which the dopant level can be controlled accurately and reproducibly. The gel materials produced by sol-gel are stable at room temperature and atmospheric pressure for at least 6 months. The gel material undergoes densification when stored for longer periods. Full characterization of the surface morphology and electrochemical behaviour of the gel material prepared as thin films by (i) spin coating and (ii) dip coating, was achieved and could support the electrochemical behaviour observed for the mixed metal oxide electrodes. Cyclic voltammetry was used to evaluate the solution electrochemistry of the electrode material in acidic medium and the kinetics of electron transfer at the mixed metal oxide electrode surfaces. Evaluation of the electrical parameters associated with the electrode bulk material could be distinguished clearly from that associated with the interface of the mixed metal oxide electrodes in acidic medium, using electrochemical impedance spectroscopy. The experimental evidence provided in this dissertation in support of the redox behaviour of the CuO and MnO₂ dopants within the SnO₂ host material, have led us to eliminate them as candidates for dimensionally stable anodes. PdO₂ doped SnO₂ produced a stable thin film anode, but with no remarkable electrocatalytic ability. The most promising anode material produced by this research is the ZrO₂ doped tin oxide, which will be evaluated further in terms of its suitability as oxidative electrocatalyst. Thus far reasonable success has been demonstrated with the use of Ti/SnO₂/ZrO₂ anode material for the destruction of micro-organisms associated with waterborne diseases.

9.3 Recommendations for future work

The electrodes evaluated in this study represents only a sample of the transition metal oxide doped tin oxide electrodes family. Further evaluation of this class of electrodes should include varying the dopant ratio to find the most effective electrocatalyst within a given combination. It has been demonstrated that the conductivity of SnO₂/ZrO₂ thin films increases up to a doping level of 5 wt%, after which they become insulating [63]. Combinations of different dopant elements in order to obtain the best possible combination for anodic oxidation, should also be investigated further. In phosphine sensing experiments, SnO₂ doped with PdO only or ZrO₂ only, have shown weaker sensitivity towards phosphine detection than a Pd activated SnO₂/ZrO₂ thin film [102]. CuO/ZrO₂ catalysts were shown to be effective for low temperature CO oxidation [103]. Investigation of adsorption processes at the individual electrode surfaces, as is possible with subtractively normalised interfacial fourier transform infrared spectroscopy (SNIFT-IRS) in order to understand the kinetics of the electrode processes better, could also be pursued [104,105].

Electrochemical impedance spectroscopy of these and other novel electrodes, provides useful information in understanding the properties of these mixed metal oxide electrocatalysts and their interfacial behaviour in oxidation and reduction reactions. The focus in this study has been on the oxidative ability of the mixed metal tin oxide electrodes prepared, whereas they are known to be good reducing gas sensor materials. The usefulness of PdO₂, ZrO₂, CuO and MnOx doped tin oxide as catalysts for reduction reactions and the kinetics of such reactions, should be further investigated.

The approach established in this dissertation provides excellent guidelines for further studies suggested here. The versatility and usefulness of impedance spectroscopy as an analytical tool has been demonstrated. However, advances in impedance spectroscopy techniques and data analysis software applied to mixed metal oxide systems, present a whole new field of research to be explored.

Examples of advance in impedance spectroscopy techniques that could prove useful are electrochemical hydrodynamic impedance (EHI) and the use of transfer functions. In EHI the rate of mass transport of reactants to, or products from, an electrochemical interface is modulated (sine wave) and the response is monitored at constant potential or constant current. This transfer function is most easily evaluated using a rotating disk electrode. Transfer functions related to the propagation of a crack through an elastic-plastic material, for which the stress intensity, instantaneous crack velocity and fracture transfer function may be evaluated, forms the basis for fracture transfer function (FTF) impedance analysis [79].

Mixed metal oxide electrodes have been and will be the focus of electrocatalyst development and the evaluation of its applications. The control over sensitivity and selectivity that can be achieved by the (i) combinations of metal oxides and (ii) the thin film preparation methods, leaves this field wide open for development in future work. We have demonstrated how these mixed metal oxides can be synthesised at relatively low cost and characterised fully (depending on the sophistication of the characterisation tools used). The dynamics of the electrochemical interface in an oxidation or reduction electron exchange can be fully analysed using CV and EIS.

9.4 Output from this dissertation

9.4.1 Contributions at conferences

1. Baker PGL, Sanderson RD, Crouch AM. *Synthesis and characterisation of thin film mixed metal tin oxides.* 35th Convention of SACI, 24-29 September 2000, Potchefstroom, South Africa.
2. Baker PGL, RD Sanderson, Crouch AM. *Preparation and characterisation of thin film mixed metal tin oxides.* 4th Annual UNESCO School and IUPAC Conference on Macromolecules and Materials Science. 7-11 April 2001, Stellenbosch, South Africa.
3. Baker PGL, Sanderson RD, Crouch AM. *Sol-gel preparation and characterisation of mixed metal oxide thin films for application as electrocatalysts.* 36th Convention of SACI, 1-5 July 2002, Port Elizabeth, South Africa.
4. Baker PGL, RD Sanderson, Crouch AM. *AC impedance and cyclic voltammetric analysis of some novel mixed metal stannates.* 6th Annual UNESCO School and IUPAC Conference on Macromolecules and Materials Science. 7-11 April 2003, Kruger National Park, Mpumalanga.

9.4.2 Papers prepared for publication

- 1 *Preparation and characterisation of mixed metal tin oxide catalyst materials.*
Baker PGL, RD Sanderson, Crouch AM.
- 2 *Electrochemical evaluation of mixed metal stannates by cyclic voltammetry and electrochemical impedance spectroscopy.* Baker PGL, RD Sanderson, Crouch AM.
- 3 *Evaluation of selected oxidation reactions at modified SnO₂ electrodes by cyclic voltammetry and electrochemical impedance spectroscopy.* Baker PGL, RD Sanderson, Crouch AM.

References:

1. Chemistry: The molecular nature of matter and change 2nd Edition, MS Silberberg, McGraw-Hill Higher Education, Chapter 23, 2000.
2. Chemistry, M Clugston, R Flemming, D Vogt; Oxford University press, Chapter 20, 2002.
3. The anodic evolution of oxygen and chlorine on foreign metal doped SnO₂ film electrodes. C Iwakura, M Inai, T Uemura, H Tamura; *Electrochimica Acta* 26(4), 1981, p579-584.
4. The electrode properties of polycrystalline SnO₂ containing up to 10% Sb or Ru oxides. W Badawy K Doblhofer, I Eiselt, H Gerischer, S Krause, J Melsheimer. *Electrochimica Acta* 29(12), 1984, p1617-1623.
5. Structural, electrical and interfacial properties of sprayed SnO₂ films. J Bruneaux, H Cachet, M Froment, A Messad. *Electrochimica Acta* 39 (8/9) 1994, p1251-1257.
6. Electrochemical and surface characteristics of tin oxide and indium oxide electrodes. NR Armstrong, AWC Lin, M Fujihira, T Kuwana. *Analytical Chemistry* 48 (4) 1976, p741-750.
7. Influence of microstructure on electrical properties of SnO₂ films prepared by CVD. L Bruno, R Lalauze, C Pijolat *Advances in Inorganic Films and Coatings* 5, 1995, p497-504.
8. Behaviour of a fluorine doped tin electrode. M Szekeley, C Mathieu, E Caillot *et al*; *Jnl of Electroanal Chem* 401, 1996, p89-93.
9. Synthesis and characterization of tin doped iron oxides. FJ Berry, C Greaves, O Helgason, J McManus. *Jnl of Materials Chemistry* 9, 1999, p223-226.

10. Preparation and characterization of SnO₂ and WO_x-SnO₂ nano sized powders and thick films for gas sensing. A Chiorino, G Ghiotti, G Martinelli *et al.* Sensors and Actuators B 78, 2001, p89-97.
11. Composition and structure of tin/vanadium oxide surfaces for chemical sensing applications. A Lavacchi, B Cortigiani, A Poggi *et al.* Sensors and Actuators B 71, 2000, p123-126.
12. Wet chemical synthesis of doped nanoparticles. T Nutz, U zum Felde, M Haase. Jnl of Chemical Physics 110 (24), 1999, p12142-12150.
13. Electrochromism of nano particulate doped metal oxides. JP Coleman, JJ Freeman, P Madhukar, JH Wagenknecht. Displays 20, 1999, p145-154.
14. Electrocatalytic behaviour of Zr₆₄Ni₃₆ and Zr₄₈Ni₂₇Al₂₅ amorphous alloys. S Spriano, M Baricco, C Antonione, P Spinelli *et al.* Electrochimica Acta 39 (11/12), 1994, p1781-1786.
15. Zirconium titanate films via aqueous polymeric precursor route. A Bianco, M Viticoli, P Scardi *et al.* Materials Science and Engineering C 15, 2001, p211-213.
16. Preparation and characteristion of mesoporous zirconium oxide. VI Parvulescu, H Bonneman, G Poncelet *et al.* Applied Catalysis A 214(2), 2001, p273-287.
17. Synthesis of nanocrystalline redispersible antimony doped tin oxide particle for the preparation of conductive, transparent coatings. D Burgard, C Goebbert, R Nass; Jnl of Sol-gel Science and Technology 13, 1998, p789-792.
18. Degradation of phenolic wastewater over Ni-oxide. St. Christoskova, M Stoyanova. Water Research 35(8), 2001, p2073-2077.

19. Low temperature iron-modified cobalt oxide system Part 2. Catalytic oxidation of phenol in aqueous phase. St. G. Christoskova, M Stoyanova, M Georgieva. *Applied Catalysis A* 208, 2001, p243-249.
20. Sol-gel film preparation of novel electrodes for the electrocatalytic oxidation of organic pollutants in water. J Grimm, D Bessarabov, W Maier, S Storck, RD Sanderson. *Desalination* 115, 1998, p295-302.
21. Direct electrochemical oxidation of organics for wastewater treatment. O J Murphy, GD Hitchens, L Kaba, CE Verostko. *Water Research* 26 (4) 1992, p443-451.
22. The anodic oxidation of p-benzoquinone and maleic acid. C Bock, B MacDougall. *Jnl of the Electrochemical Society* 146 (8), 1999, p2925-2932.
23. Ti and Ce acidic solutions. VA Alves, LA da Silva, JFC Boodts, S Trasatti. *Electrochimica Acta* 39 (11/12), 1984, p1585-1589.
24. The influence of metal oxide properties on the oxidation of organics. C Bock, B Mc Dougall ; *Jnl of Electroanalytical Chemistry* 491, 2000, p48-54.
25. A study of electrode passivation during aqueous phenol electrolysis. M Gattrell, DW Kirk. *Journal of the Electrochemical Society*, 140(4), 1993, 903-911].
26. Anodic oxidation of phenol for wastewater treatment. Ch Comninellis, C Pulgarin. *Journal of applied electrochemistry* 21 (1991) 703-708.
27. Service life of Ti/SnO₂-Sb₂O₅ anodes. B Corea-Lozano, Ch Comninellis, A de Battisti. *Journal of Applied Electrochemistry* 27, 1997,970-974.
28. Nanocatalyst sensitisers by agglomeration of nanofilms. J Mizsei, L Pirttiahho, M Karppinen, V Lanto. *Sensors and Actuators B* 65 (2000) 195-198.
29. LE Cadus, O Feretti, *Applied Catalysis A* 233 (2002) 239-253.
30. LM Gandia, MA Vicenti, A Gill. *Applied Catalysis B* 38(4) (2002) 295-307.

31. Y Liu, Z Wei, Z Feng, M Luo, P Ying, C Li. *Journal of Catalysis* 202, (2001) 200-204.
32. Nanoporous amorphous manganese oxide as electrocatalyst for oxygen reduction in alkaline solutions. J Yang, JJ Xu; *Electrochemistry Communications* 2 (2003) 306-311.
33. KCC Kharas. *Applied Catalysis B* 2(2) (1993) 207-224.
34. R Zhou, T Yu, X Jiang, F Chen, X Zheng. *Applied Surface Science* 148 (1999) 263-270.
35. A Dandekarr, MA Vanice. *Applied Catalysis B* 22 (1999) 179-200.
36. J Ramirez-Ortiz, T Ogura, J Medina-Valtierra, SE Acosta-Ortiz, P Bosch, JA de los Reyes, VH Lara. *Applied Surface Science* 174 (2001) 177-184.
37. Preparation of SnO₂ -CuO nanocrystalline powders in two different ways by the sol-gel technique. G Fang, Z Liu, Z Zhang *et al.* *Phys. Stat. Sol. A* 156 1996, p15-22.
38. Preparation of ZrO₂-SnO₂ thin films by the sol-gel technique and their gas sensitivity. G Fang, Z Liu, Z Zhang *et al.* *Phys. Stat. Sol. A* 156, 1996, p81 - 85.
39. Chemical synthesis of homogeneous SnO₂ powders doped with manganese. D Gouvea, JA Varela, E Longo. *Eur. J. Solid State Inorg. Chem.* 33(4), 1996, p343-354.
40. Structural characterisation of Pd-doped SnO₂ thin films using XPS. X Cao, L Cao, W Yao, X Ye. *Surface and Interface Analysis* 24, 1996, p662-666.
41. Sol-gels and electrochemistry. MM Collinson, AR Howells. *Analytical Chemistry*, November, 2002, p702A-709A.
42. Review of sol-gel thin film formation. CJ Brinker, AJ Hurd, PR Schunk,

- GC Frye, CS Ashley. *Journal of Non-Crystalline Solids* 147&148, 1992, p424-436.
43. Microporous layers from sol-gel techniques. A Larbot, JA Alary, JP Fabre, C Guizard. *Mat. Res. Soc. Symp. Proc.* 73, 1986, p659-664.
44. Morphology of SnO₂ thin films obtained by sol-gel technique. JP Chaleton, C Terrier, E Bernstein. *Thin Solid Films*, 247, 1994, p162-168.
45. Introduction to thermal analysis. ME Brown. Chapman and Hall publication. 1988; Chapter 3, p7-22.
46. Solid State Chemistry Techniques: AK Cheetman, P Day; Clarendon Press, Oxford 1987, Chapter 2, p39-49.
47. Microscopy and analysis: P J Goodhew. Wykeham Publications (London) LTD; 1975.
48. Microscopy in the Nano scale. Honours student guide 2001, University of Stellenbosch.
49. Formation and characterization of metal-polymer nanostructured composites. SA Zavyalov, AN Pivkina, J Schoonman. *Solid State Ionics* 147, 2002, p415-419.
50. Particle induced X-ray emission spectrometry (PIXE). SAE Johansson, JL Campbell, KG Malmqvist. John Wiley & Sons, Inc. 1995 Chapter 3, p101-161.
51. Electron microprobe analysis, 2nd Edition SJB Reed. Cambridge University Press, 1997, Chapter 5, p49-57.
52. <http://www.cea.com/literature/rbsbroch.pdf>
53. Charles Evans and associates: Application bulletin no. 6.
<http://www.cea.com/literature/rbsapp6.pdf>

54. Instrumental methods in Electrochemistry. Southampton Electrochemistry Group; Horwood publishing, Chichester. Chapter 2 and 6, p178-228.
55. Analytical Electrochemistry 2nd Edition. J Wang; Wiley-VCH; Chapter 1, p1-27
56. Textbook of electrochemistry. G Kortüm, JO'M Bockris, volume 1951)
57. Platinum microelectrodes with unique high surface areas. JM Elliott, PR Birkin, PN Bartlett, GS Attard. *Langmuir* 15 (22), 1999, p7411-7415.
58. Design of oxide electrodes with large surface area. Y Takasu, Y Murakami. *Electrochimica Acta* 45 (25-26), 2000, p4135-4141.
59. Surfactant induced modification of dopants reactivity in sol-gel matrices. C Rottman, G Grader *et al.* *J Am. Chem. Soc.*, 121, 1999, p8533-8543.
60. Sol-gel template synthesis of semiconductor oxide micro- and nanostructures. BB Lakshmi, CJ Patrisi, CR Martin; *Chem. Mater.* 9, 1997, p2544-2550.
61. Ordered media in chemical separations. Edited by WL Hinze, DW Armstrong. American Chemical Society, Symposium Series 342, p1-20.
62. Thermolytic degradation behaviour of inorganic ion exchanger incorporated Nafion-117. S K Tiwari, S K Nema, Y K Agarwal. *Thermochimica Acta* 317, 1998, p175-182.
63. Transparent conducting films of $\text{In}_2\text{O}_3\text{-ZrO}_2$, $\text{SnO}_2\text{-ZrO}_2$ and ZnO-ZrO_2 . SB Qadri, H Kim, HR Khan, EF Skelton *et al.* *Thin Solid Films* 377-378, 2000, p750-754.
64. XRD and electrical characterization of photo-CVD zirconium oxide layers. JJ Yu, I W Boyd. *Applied Surface Science* 208-209, 2003, p374-377.
65. Oxygen reduction at Pr and $\text{Pt}_{70}\text{Ni}_{30}$ in $\text{H}_2\text{SO}_4/\text{CH}_3\text{OH}$ solution. JF Drillet, A Ee, J Friedemann *et al.* *Electrochimica Acta* 46 (2002) 1983-1988.

66. Nanostructured platinum as an electrocatalyst for the electrooxidation of formic acid. J Jiang, A Kucernak. *Journal of electroanalytical Chemistry* 520 (2002) 64-70.
67. Bimetallic catalysts for continuous catalytic wet air oxidation of phenol. A Fortuny, C Bengoa, J Font, A Fabregat. *Journal of Hazardous Materials* (1999) 181-193.
68. AC conductivity based microstructural characterization of Ytria stabilized zirconia. G Sauti, DS McLachlan. *Mat. Res.Soc.Symp. Proc.* 699 (2002) 69-74.
69. AC and DC conductivity based microstructural characterization. DS McLachlan, K Cai, G Sauti. *International Journal of Refractory Metals and Hard Materials* 19 (2001) 437-445.
70. Application notes from Gamry Instruments (<http://www.gamry.com>)
71. (<http://www.cp.umist.ac.uk/lecturenotes/echem>)
72. Interfacial properties of oxides with technological impact in electrochemistry. S Ardizzone, S Trasatti. *Advances in colloidal and interface science* 64 (1996) 173-251.
73. <http://www.webelements.com/webelements/compounds/text/Zr>
74. <http://www.webelements.com/webelements/compounds/text/Sb>
75. <http://www.webelements.com/webelements/compounds/text/Cu>
76. <http://www.webelements.com/webelements/compounds/text/Mn>
77. <http://www.webelements.com/webelements/compounds/text/Pd>
78. <http://www.webelements.com/webelements/compounds/text/Sn>
79. Impedance Spectroscopy. J Ross Mc Donald. John Wiley and Sons. p12-20.
80. Electrode behaviour at (La,Sr)MnO₃/Y₂O₃-ZrO₂ interface by EIS. SP Jiang, JG Love, Y Ramprakash. *Journal of Power Sources* 100 (2002) 201-208.

81. ZVIEW online software manual; Distributed circuit elements.
82. Study of the formation of Co_3O_4 thin films using sol-gel method.
H Tototzintle-Huitile, E Prokhorov, J Gonzalez-Hernandez *et al.* *Journal of Physics and Chemistry of Solids* 64, 2003, p975-980.
83. Impedance spectroscopy studies on chemically deposited CdS and PbS polycrystalline films. MB Ortuno-Lopez, JJ Valenzuela-Jauregui, J Gonzalez-Hernandez *et al.* *Journal of Physics and Chemistry of Solids* 63, 2002, p665-668.
84. <http://www.consultrsr.com/resources/eis/warburg1.htm>
85. Jyh-Myng, Annamalai Senthil Kumar, Jyh-Cheng Chen. *Journal of Molecular Catalysis A: Chemical* 165, 2001, p177-188.
86. VA Alves, LA da Silva, JFC Boodts. *Electrochimica Acta* 44, 1998, p1525-1534.
87. Capacitance of the double layer at polycrystalline Pt electrodes bearing a surface oxide film. WG Pell, A Zolfaghari, BE Conway. *Journal of Electroanalytical Chemistry* 532, 2002, p13-23.
88. M Metikos-Hukovic, S Omanovic. *Journal of Electroanalytical Chemistry* 455, 1998, p181-189.
89. Electrochemical oxidation of phenol for wastewater treatment using SnO_2 anodes. C Comninellis, C Pulgarin. *Jnl of Appl. Electrochem.* 23, 1993, p108-112.
90. R Kotz, S Stucki, B Carcer. *Journal of Applied Electrochemistry* 21 (1991) 14.
91. S Stucki, R Kotz, B Carcer, W Suter. *Journal of Applied Electrochemistry* 21(1991) 99.

92. Electrochemistry for a cleaner environment. Chapter 15: Electrochemical oxidation of organic waste. AC Almon, BR Buchanan, 301-321, The Electrosynthesis Co.Inc., Buffalo, 1992.
93. Electrocatalysis in the electrochemical conversion of organic pollutants for waste water treatment. C Comninellis. *Electrochimica Acta* 39(11/12) 1994, p1857-1862.
94. F Ortega, E Dominguez, E Burestedt. *J. Chromatogr. A* 675, 1994, p65.
95. KR Rogers, JY Becker, J Wang, F Lu. *Anal. Chem. Technol.* 3, 1999, p161.
96. Improved selective electrocatalytic oxidation of phenols by tyrosine based carbon paste electrode biosensors. KR Rogers, JY Becker, J Cembrano. *Electrochimica Acta* 45, 2000, p4373-4379.
97. Degradation of phenol and phenolic compounds by a defined denitrifying bacterial culture. S Thomas, S Sarfaraz, LC Mishra, L Iyengar. *World Journal of Microbiology and Biotechnology* 18 (1) 2002, 57-63.
98. Electrochemical oxidation of aqueous phenol at a carbon black slurry electrode. JL Boudenne, O Cerclier, J Galea, E van der Vlist. *Applied Catalysis A*, 143, 1996, p185-202.
99. Photodiode array detection for elucidation of the structure of phenolic compounds. *Journal of Chromatography A* 665, 1993, p119-125.
100. Electrochemical oxidation of phenol at boron-doped diamond electrode. J Iniesta, PA Michaud, M Panizza, G Cerisola, A Aldaz, Ch Comninellis. *Electrochimica Acta*, 46, 2001, p3573-3578.
101. Reactor design and catalyst development for the degradation of organic waste in water; Department of Chemical Engineering, M Cronje, RD Sanderson, JH Knoetze.

102. PH₃ detection by SnO₂-ZrO₂ thin films. T Ratcheva, I Stambolova and K Konstantinov. *Sensors and Actuators B* 21, 1994, p199-204.
103. Temperature programmed reduction and desorption studies of CuO/ZrO₂ catalysts. R Zhou, T Yu, X Jiang, F Chen, X Zheng. *Applied Surface Science* 148 (1999) 263-270.
104. Perspectives on physical electrochemistry. W R Fawcett. The Electrochemical Society *Interface*, Winter 2000.
105. http://w3.rz-berlin.mpg.de/pc/shg/shg_sers/SNIFTIRSpaper.html